AVERTISSEMENT

Ce document est le fruit d'un long travail approuvé par le jury de soutenance et mis à disposition de l'ensemble de la communauté universitaire élargie.

Il est soumis à la propriété intellectuelle de l'auteur. Ceci implique une obligation de citation et de référencement lors de l'utilisation de ce document.

D'autre part, toute contrefaçon, plagiat, reproduction illicite encourt une poursuite pénale.

Contact : ddoc-theses-contact@univ-lorraine.fr

LIENS

Code de la Propriété Intellectuelle. articles L 122. 4
Code de la Propriété Intellectuelle. articles L 335.2- L 335.10
http://www.cfcopies.com/V2/leg/leg_droi.php
http://www.culture.gouv.fr/culture/infos-pratiques/droits/protection.htm

THESE

de

DOCTORAT DE L'UNIVERSITE DE LORRAINE

Ecole Doctorale C2MP
Chimie-Mécanique-Matériaux-Physique

Spécialité de doctorat : Sciences des Matériaux
Discipline : Mécanique des Matériaux

Soutenue publiquement le 06/12/2019 par :

Manoj Subramani

DYNAMIC RESPONSE OF POROUS DUCTILE MATERIALS CONTAINING CYLINDRICAL VOIDS

Devant le jury composé de :

Nicolas Jacques	Maître de Conférences-HDR, ENSTA Bretagne, France	**Rapporteur**
Patrice Longère	Professeur, ISAE-SUPAERO, France	**Rapporteur**
Laurent Berthe	Directeur de Recherche, Arts et Métiers ParisTech, France	**Examinateur**
Guadalupe Vadillo Martín	Associate Professor, Université Carlos III de Madrid, Espagne	**Examinateur**
Jean-François Molinari	Professeur, Ecole Polytechnique Fédérale de Lausanne, Suisse	**Examinateur**
Alain Molinari	Professeur Emérite, Université de Lorraine, France	**Examinateur**
Christophe Czarnota	Maître de Conférences-HDR, Université de Lorraine, France	**Co-directeur de thèse**
Sébastien Mercier	Professeur, Université de Lorraine, France	**Co-directeur de thèse**

LABORATOIRE D'ETUDE DES MICROSTRUCTURES ET DE MECANIQUE DES MATERIAUX
LEM3-UMR CNRS 7239

Acknowledgement

Firstly, I would like to express my sincere gratitude to my advisors Sébastien Mercier and Christophe Czarnota for the continuous support of my Ph.D study and related research, for their patience, motivation, and immense knowledge. Their guidance helped me in all the time of research and writing of this thesis. I could not have imagined having a better advisors and mentors for my Ph.D study.

Besides my advisors, I gratefully acknowledge Dr. José Antonio Rodríguez for including me as a Early Stage Researcher for the project OUTCOME: A European Marie Sklodowska-Curie Innovative Training Network (ITN-ETN). My thanks to European Union Horizon 2020 research and innovation programme for funding my PhD under the Marie Sklodowska-Curie grant agreement N^{0}675602. I also extend my thanks to Université de Lorraine, France, two international universities (UC3M, Spain and Technion, Israël) and four industries to be part of this project. I thank the Professors and Engineers from the respective universities and industries who provided me an opportunity to join their team as a part of my secondments as well as industrial visits, to learn and share scientific knowledge between the researchers.

I would like to thank also my thesis committee: Prof N. Jacques, Prof P. Longère, Prof J.F. Molinari, Prof G. Vadillo and Prof L. Berthe for their insightful comments and encouragement, but also for questions which incented me to widen my research from various perspectives.
I thank my fellow labmates from LEM3 and OUTCOME project members for the stimulating discussions and for all the work, fun and travel we have had in the last three years. In particular, I am grateful to Prof. Alain Molinari for supporting and giving valuable guidance in our research.

Last but not the least, I would like to thank my family: specially my mother, my father and my loved ones for supporting me spiritually throughout writing this thesis and my life in general.







Contents

1 Résumé des travaux de thèse en Français **3**

1.1 Contexte et objectifs de la thèse 3

1.2 Modèle analytique 6

1.2.1 Volume Elémentaire Représentatif 8

1.2.2 Contributions statique et dynamique du tenseur des contraintes 9

1.3 Résultats 11

1.4 Conclusion et perspectives 15

2 Literature review **23**

2.1 Introduction 23

2.2 Experimental works 23

2.3 Modeling 30

2.3.1 Quasi-static analysis on void growth 30

2.3.1.1 Introduction 30

2.3.1.2 McClintock Model 31

2.3.1.3 Gurson model 33

2.3.1.4 Gurson Tvergaard and Needleman model (GTN model) . . 37
2.3.2 Dynamic analysis for porous materials 38
2.3.2.1 Introduction 38
2.3.2.2 Carroll and Holt Model 43
2.3.2.3 Molinari and Mercier Model-2001 45
2.3.2.4 Leblond and Roy Model 50
2.3.2.5 Molinari et. al Model 52
2.3.3 Conclusion 54

3 Modeling **57**

3.1 Geometry of the RVE and formulation of the velocity field 57
3.1.1 Formulation of the admissible velocity field 62
3.2 Formulation of the micro-inertia dependent term Σ^{dyn} 65
3.2.1 Plane strain case 68
3.2.2 Uniaxial deformation 69
3.3 Quasistatic stress tensor Σ^{static} 69

4 Results **71**

4.1 Introduction 71
4.2 Axisymmetric loading 71
4.3 Plane strain 73
4.4 Hydrostatic loading 78

4.5 Additional loading cases 87

4.6 Conclusion 97

5 Finite element modeling **101**

5.1 Introduction 101

5.2 Plane strain configuration 102

5.3 Hydrostatic loading 105

5.3.1 Boundary conditions inherited from the analytical model 105

5.3.2 Closed unit-cell 107

5.3.3 Validation on the reference case 111

5.3.4 Thin cylinder, l_0=10μm 112

5.4 Additional loading cases 113

5.4.1 Imposed axial strain rate (D_{33}=constant) with combined stress imposed on the lateral surface 113

5.4.2 Uniaxial loading: Case 1, χ=1/3 114

5.4.3 Biaxial loading: Case 2, χ=2/3 115

5.5 Influence of the elastic properties 116

6 Conclusion and perspectives **121**

A Formulation of the macroscopic dynamic stress tensor, $\Sigma^{\mathbf{dyn}}$. **125**

A.1 General formulation 125

A.2 Case where $\mathbf{\Omega} = \mathbf{0}$ 130

A.3 Axisymmetric case 131

B Analytical relationships for the quasi-static macroscopic stress, $\Sigma^{\mathbf{static}}$. 135

C Formulation of the macroscopic dynamic stress tensor ($\Sigma^{\mathbf{dyn}}$) for 2D approach. 137

Bibliography 146

Chapter 1

Résumé des travaux de thèse en Français

1.1 Contexte et objectifs de la thèse

La thèse est réalisé dans le cadre d'un projet ITN–H2020 "OUTCOME", numéro de convention 675602. Le consortium est formé de l'Université Carlos III Madrid, Espagne (coordinateur du projet), de Technion, Israël, de l'Université de Lorraine, France et de partenaires industriels CIMULEC, France et AEROSERTEC, Espagne. L'objectif de ce projet est de former huit doctorants sur la thématique de la tenue des matériaux en conditions extrêmes notamment sous chargement dynamique.

La rupture des matériaux ductiles résulte de l'interaction de trois mécanismes, à savoir la nucléation, la croissance et la coalescence des vides. Dans ce doctorat, nous nous intéressons à l'endommagement des matériaux poreux contenant des vides cylindriques, sous chargement dynamique. Cette étude intéresse de nombreux domaines d'application civile et militaire (dans le cadre du développement de structures absorbantes de choc) ou spatiale (par exemple dans l'étude de l'effet d'impacts de débris sur des satellites). Enfin, du fait du développement de la fabrication additive, la conception de matériaux contenant des vides cylindriques est une voie

possible pour créer des matériaux légers à haut pouvoir dissipatif. Ce travail s'attèle à décrire le comportement dynamique de matériaux architecturés tels que des nids d'abeille faiblement poreux.

Sous chargement dynamique, les particules matérielles situées à proximité des cavités subissent de grandes accélérations. Les effets de micro-inertie, induits par ces accélérations développées à l'échelle locale, jouent un rôle prépondérant dans la réponse macroscopique et le développement de l'endommagement dans les matériaux poreux. La prise en compte de ces effets a permis de décrire en particulier l'effet retard plus marqué lorsque les vides sont initialement plus gros. Les approches classiques (e.g. de type GTN) développées pour des cas de chargements quasi-statiques, et utilisées encore souvent pour la modélisation d'une réponse dynamique, ne révèlent pour la plupart que l'effet de porosité.

Les travaux précurseurs de Carroll and Holt [5], portant sur la réponse d'une sphère creuse soumise à un chargement en pression appliqué à l'extérieur du motif, ont conduit à l'expression analytique de la contrainte hydrostatique en chargement dynamique. Celle-ci est la somme d'une contribution statique, liée à la résistance de la matrice (considérée parfaitement plastique), et d'une partie reflétant les effets micro-inertiels. Cette partie dynamique se trouve proportionnelle à la masse volumique de la matrice et au carré du rayon du vide. A partir d'une approche d'homogénéisation en dynamique, Molinari and Mercier [26] ont développé un modèle analytique pour une matrice viscoplastique contenant des cavités sphériques. Ces travaux permettent d'ouvrir plus largement les champs d'application, ne se limitant pas à des chargements purement hydrostatiques [voir également 46, 48]. Tout comme le modèle de Carroll and Holt [5], l'approche analytique de Molinari and Mercier [26] met en évidence que la contrainte macroscopique est la somme d'une contribution quasi-statique et d'une partie dynamique proportionelle à la masse volumique et au carré du rayon du vide. Ce modèle a vu de nombreuses

évolutions au sein du LEM3 et de la communauté scientifique en général pour la description du phénomène d'écaillage [e.g. 9, 8, 16, 45], la propagation dynamique de fissures [e.g. 17] ou encore la propagation d'ondes de choc dans les matériaux poreux et mousses métalliques [e.g. 1, 10].

Le modéle de Molinari and Mercier [26] a été récemment adapté à la prise en compte de la forme plus complexe des cavités par Sartori et al. [36, 34]. Les auteurs ont alors adopté le champ de vitesse proposé par Gologanu et al. [14] pour des vides ellispoïdaux afin d'évaluer la contribution inertielle. Ils ont mis ainsi en évidence que les effets de micro-inertie sont modulés par la masse volumique de la matrice et deux paramètres de longueur (demi-axes du vide). En effet, ce type de géométrie est caractérisé par deux paramètres de longueur (ou de façon équivalente par la dimension d'un des demi-axes et le facteur de forme du vide), alors que le vide sphérique n'est défini géométriquement que par son rayon.

Dans ce travail de thèse, nous considérons des matériaux contenant des cavités cylindriques parallèles, représentatifs de structures perforées ou décrivant des matériaux architecturés de type nid d'abeille. Ce type de géométrie est également caractérisée par deux paramètres de longueur, (le rayon et la longueur du vide) qui vont influencer la réponse du matériau poreux en sollicitation dynamique. Peu d'études ont été menées sur les effets micro-inertiels pour des cavités cylindriques. Citons les travaux de Molinari et al. [25], portant sur la phase de coalescence en présence des effets de micro-inertie, pour lesquels le trajet de chargement étudié correspond à une déformation uniaxiale. Citons également Leblond and Roy [20] qui ont proposé un modèle analytique pour une matrice viscoplastique en tenant compte des effets micro-inertiels pour des vides de forme cylindrique. Les auteurs ont adopté le champ de vitesse de Gurson [15] pour décrire la réponse du matériau sous un chargement dynamique en déformation plane généralisée. Le terme d'accélération axiale (dans la direction de l'axe du vide cylindrique) a

été négligé dans l'approche et la contrainte dynamique se trouve influencée par la masse volumique et une unique longueur interne, le rayon du vide. Par conséquent, le modèle ne permet pas de restituer l'influence d'un second paramètre qui est la longueur du vide.

L'objectif de ce travail de thèse est de proposer un modèle théorique prenant en compte les effets de micro-inertie pour la croissance des cavités cylindriques afin de mettre en évidence l'influence du rayon et de la longueur des vides pour des sollicitations dynamiques. Le stade ultime du processus de rupture ductile n'est pas abordé dans ce doctorat et les instabilités de type bandes de cisaillement, ou de localisation, ne sont pas prises en compte dans l'analyse que l'on développera, voir par exemple Longère [21], Dorothy and Longère [11]. La coalescence est supposée se produire par empiètement géométrique (les cavités croissent jusqu'à ce que leur paroi se rencontre). Le critère ainsi retenu pour définir l'apparition de la rupture est une valeur critique de porosité. L'approche théorique, qui sera résumée dans la section suivante, est validée par une comparaison à des résultats obtenus par simulations numériques sur des cellules unitaires développées dans le cadre de la thèse. Des cas de chargements axisymmétriques variés ont été considérés dans notre travail. Dans cette partie résumant nos travaux, nous avons sélectionné un cas de déformation plane, pour illustrer la diminution de la contrainte axiale lors de l'évolution de l'endommagement ainsi qu'un cas de chargement hydrostatique afin de mettre en lumière l'influence de la longueur du vide sur le comportement macroscopique.

1.2 Modèle analytique

Notre approche théorique s'appuie sur le modèle d'homogénéisation en dynamique proposé par Molinari and Mercier [26] que nous adaptons au cas de vides cylindriques. Selon les auteurs, en considérant des conditions de contraintes ou de déformations homogènes au bord du Volume

Elémentaire Représentatif (VER), la contrainte macroscopique $\boldsymbol{\Sigma}$ est définie par :

$$\boldsymbol{\Sigma} = \langle \boldsymbol{\sigma} \rangle + \left\langle \rho \boldsymbol{\gamma} \otimes \boldsymbol{x} \right\rangle \tag{1.1}$$

où $\langle \bullet \rangle = \frac{1}{|V|} \int_V \bullet \, \mathrm{d}V$, ρ représente la masse volumique de la matrice, $\boldsymbol{\gamma}$ l'accélération. $|V|$ désigne le volume du VER, '$\otimes$' est le produit tensoriel et $\boldsymbol{x}$ la position d'une particule matérielle. La définition classique quasi-statique où la contrainte est obtenue par moyenne volumique dans le VER, i.e. $\boldsymbol{\Sigma}$=$\langle \boldsymbol{\sigma} \rangle$ n'est alors plus valide en dynamique (lorsque $\boldsymbol{\gamma} \neq \mathbf{0}$).

Nous considérons le motif de cylindres concentriques comme VER de notre matériau poreux au bord duquel un champ de vitesse de déformation homogène est appliqué :

$$\boldsymbol{v} = \mathbf{D} \cdot \boldsymbol{x} \, , \tag{1.2}$$

où $\mathbf{D}$ est le tenseur macroscopique des vitesses de déformation (supposé homogène) et " $\cdot$ " représente le produit simplement contracté. En adoptant un champ cinématiquement admissible et en utilisant le principe des puissances virtuelles, il est possible de montrer que la contrainte macroscopique $\boldsymbol{\Sigma}$ s'exprime comme la somme de deux contributions :

$$\boldsymbol{\Sigma} = \boldsymbol{\Sigma}^{static} + \boldsymbol{\Sigma}^{dyn} \, . \tag{1.3}$$

$\boldsymbol{\Sigma}^{dyn}$ représente la partie tenant compte des effets de micro-inertie et $\boldsymbol{\Sigma}^{static}$ tient compte de la réponse rhéologique de la matrice (incluant par exemple les effets visqueux), mais est indépendante des effets micro-inertiels. $\boldsymbol{\Sigma}^{static}$ peut s'obtenir à partir de tout potentiel ou surface de charge statique de la littérature. Lorsque les effets de micro-inertie sont négligeables, $\boldsymbol{\Sigma}^{dyn} = \mathbf{0}$ et $\boldsymbol{\Sigma} = \boldsymbol{\Sigma}^{static}$. Précisons également que dans le cadre général la contrainte micro-inertielle

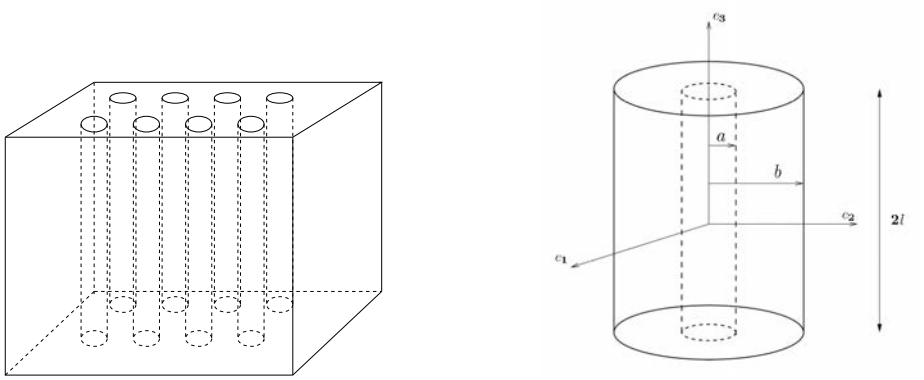

Figure 1.1: Représentation schématique d'un matériau poreux contenant des cavités cylindriques parallèles. Le VER adopté est décrit par un cylindre creux à section circulaire (longueur $2l$, rayon interne a, rayon externe b).

peut être non symmétrique.

Dans la suite, nous considérons des cavités cylindriques entourées d'une matrice parfaitement plastique incompressible. Nous adoptons la surface de charge et le champ de vitesse de Gurson [15] pour décrire d'une part la réponse statique du matériau poreux $\mathbf{\Sigma}^{static}$ et établir d'autre part une relation explicite pour la contribution dynamique $\mathbf{\Sigma}^{dyn}$.

1.2.1 Volume Elémentaire Représentatif

Le Volume Elementaire Représentatif (VER) du matériau poreux considéré correspond à un cylindre creux (à section circulaire) de rayon interne a, rayon externe b, de longueur $2l$, voir Fig. 1.1. La géométrie initiale est caractérisée par a_0, b_0 et $2l_0$ respectivement. La porosité courante (resp. initiale) est définie par $f = a^2/b^2$ (resp. $f_0 = a_0^2/b_0^2$).

Puisque la matrice est incompressible et l'élasticité est négligée dans notre approche, l'évolution de la porosité se trouve donnée par la relation :

$$\dot{f} = 3(1-f)D_m \tag{1.4}$$

où $D_m = \text{tr}(\mathbf{D})/3$ désigne le taux de déformation volumique macroscopique, tr$(\cdot)$ correspondant à la trace de $(\cdot)$.

La théorie est développée dans le manuscrit pour des cas de chargement quelconque. Nous proposons, dans cette partie, de nous focaliser sur des cas de chargement axisymmétrique pour lesquels les tenseurs des contraintes et de vitesses de déformation macroscopiques s'écrivent dans la base orthonormée $(\mathbf{e}_1, \mathbf{e}_2, \mathbf{e}_3)$, voir Fig. 1.1:

$$\mathbf{\Sigma} = \begin{bmatrix} \Sigma_{11} & 0 & 0 \\ 0 & \Sigma_{11} & 0 \\ 0 & 0 & \Sigma_{33} \end{bmatrix} \quad \mathbf{D} = \begin{bmatrix} D_{11} & 0 & 0 \\ 0 & D_{11} & 0 \\ 0 & 0 & D_{33} \end{bmatrix}. \tag{1.5}$$

1.2.2 Contributions statique et dynamique du tenseur des contraintes

La partie quasi-statique du tenseur des contraintes $\mathbf{\Sigma}^{\text{static}}$ est obtenue à partir de la surface de charge proposée par Gurson [15] pour des cavités cylindriques :

$$\Phi(\mathbf{\Sigma}^{\text{static}}, \sigma_0, f) = \left(\frac{\Sigma_{\text{eq}}^{\text{static}}}{\sigma_0}\right)^2 + 2f\cosh\left(\sqrt{3}\frac{\Sigma_{11}}{\sigma_0}\right) - (1+f^2) = 0 \tag{1.6}$$

avec σ_0 la limite élastique de la matrice (supposée ici parfaitement plastique) et où $\Sigma_{\text{eq}}^{\text{static}} = \sqrt{\frac{3}{2}\mathbf{\Sigma}^{\text{static}\prime} : \mathbf{\Sigma}^{\text{static}\prime}}$ est la contrainte (quasi-statique) macroscopique équivalente, $(\cdot)'$ désignant la partie déviatorique du tenseur de second ordre $(\cdot)$ et l'opérateur ':' représentant le produit doublement contracté.

Pour des chargements axisymmétriques, les tenseurs des contraintes quasi-statiques et des vitesses de déformation sont liés de façon explicite par les relations proposées dans Sartori et al.

[35], voir Annexe B.

En configuration de déformation plane où $D_{33} = 0$ (i.e. la longueur du cylindre est constante au cours de la déformation $l = l_0$), le tenseur des contraintes quasi-statiques est sphérique :

$$\Sigma_{11}^{static} = \Sigma_{22}^{static} = \Sigma_{33}^{static} = \frac{\sigma_0}{\sqrt{3}} \ln\left(\frac{1}{f}\right) \mathrm{sgn}(D_{11}) \,, \tag{1.7}$$

l'opérateur 'sgn$(\cdot)$' désignant le signe de $(\cdot)$. A partir de l'Eq (1.3), lorsque les effets de micro-inertie sont négligés, le tenseur des contraintes macroscopiques $\boldsymbol{\Sigma}$ coïncide avec $\boldsymbol{\Sigma}^{\text{static}}$ et par conséquent est sphérique en déformation plane. Cela n'est en revanche plus le cas lorsque les effets d'inertie sont importants.

Le tenseur des contraintes dynamiques $\boldsymbol{\Sigma}^{\text{dyn}}$ a été évalué de façon explicite à partir du champ de vitesse proposé par Gurson [15], voir Annexe A pour les détails. Dans le cas de chargements axisymmétriques définis en Eq (1.5) les composantes non nulles de $\boldsymbol{\Sigma}^{\text{dyn}}$ peuvent se mettre sous la forme :

$$\Sigma_{11}^{\text{dyn}} = \Sigma_{22}^{\text{dyn}} = \rho a^2 F \,, \Sigma_{33}^{\text{dyn}} = \rho a^2 G + \frac{\rho l^2}{3} (1 - f) \left(\dot{D}_{33} + D_{33}^2\right) \tag{1.8}$$

où les fonctions F et G, voir Eqs (A.31-A.32), dépendent de la porosité f, de termes quadratiques en D_{11} et D_{33}, et de termes linéaires contenant les dérivées en temps $\dot{D}_{11}$ et $\dot{D}_{33}$. La relation (1.8) confirme la dépendance particulière à la vitesse de déformation héritée des effets de micro-inertie, et relevée aussi pour les vides sphériques et sphéroïdaux [26, 36]. L'equation (1.8) révèle également que la réponse dynamique du matériau est intimement liée à la taille du VER. Ici, pour les vides cylindriques, il apparaît que la contrainte dynamique est proportionnelle à la masse volumique de la matrice ρ et dépend du carré de deux longueurs caractéristiques : le rayon du vide a et la demi-longueur l. Plus particulièrement, un résultat

important du modèle théorique concerne les effets d'échelle différenciés entre les composantes du tenseur des contraintes dans le plan et celle dans l'axe du cylindre. En effet, $\Sigma_{11}^{\text{dyn}} = \Sigma_{22}^{\text{dyn}}$ sont proportionnelles au carré du rayon du vide, tandis que la contrainte axiale Σ_{33}^{dyn} est de plus liée au carré de la longueur du vide. Cet aspect s'explique par l'anisotropie géométrique du vide cylindrique.

En déformation plane axisymmétrique, $D_{33} = 0$, on obtient :

$$\Sigma_{11}^{\text{dyn}} = \Sigma_{22}^{\text{dyn}} = \frac{\rho a^2}{2}\left\{ f^{-1}\ln\left(\frac{1}{f}\right)\dot{D}_{11} - f^{-1}\left[f^{-1} - 2\ln\left(\frac{1}{f}\right) - 1\right] D_{11}^2 \right\} \tag{1.9}$$

$$\Sigma_{33}^{\text{dyn}} = \frac{\rho a^2}{2}\left\{ \left[f^{-1}\ln\left(\frac{1}{f}\right) - f^{-1} + 1\right]\dot{D}_{11} - \left[(1+f)\,f^{-2} - 3f^{-1}\ln\left(\frac{1}{f}\right) - 2\right] D_{11}^2 \right\} \tag{1.10}$$

Il est intéressant de noter, à partir des Eqs (1.9-1.10), que les effets d'inertie sont toujours présents dans la contribution axiale Σ_{33}^{dyn}. Ce résultat a pu être révélé par l'approche développée dans notre travail, et ne peut pas être obtenu par une analyse 2D, voir Annexe C.

1.3 Résultats

Cette section présente quelques configurations de chargement sélectionnées parmi celles abordées dans le chapitre 4 de la thèse. En outre, précisons que le modèle analytique que nous avons développé est confronté de façon très satisfaisante à des simulations numériques sous Abaqus/Explicit. Celles-ci ont été menées sur des modèles éléments finis développés dans le doctorat, voir chapitre 5 pour les détails.

Nous considérons ici la réponse dynamique d'un milieu poreux contenant des vides cylin-

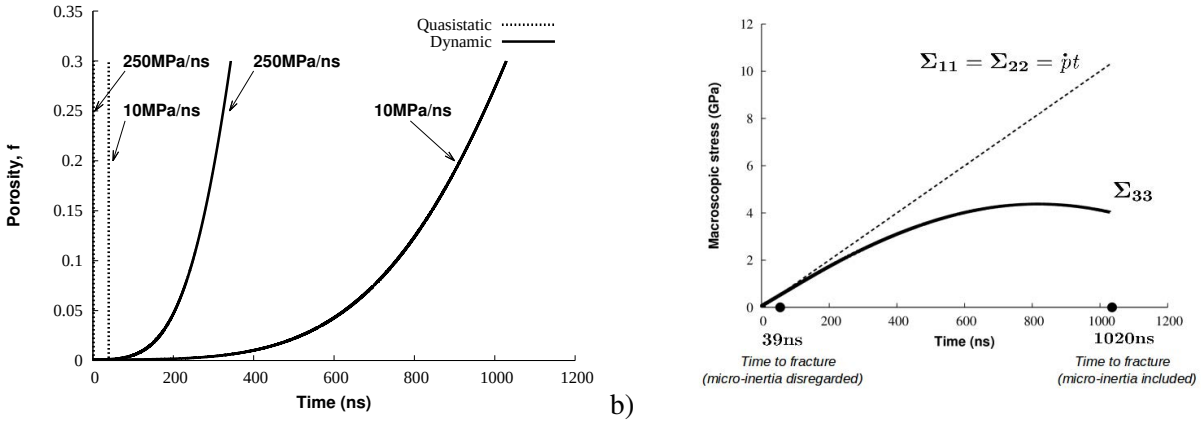

a) b)

Figure 1.2: Evolutions de a) la porosité f et b) des contraintes $\Sigma_{11} = \Sigma_{22}$, Σ_{33} en fonction du temps. Le chargement est axisymmétrique en déformation plane (D_{33}=0 est imposé) et $\Sigma_{11} = \Sigma_{22} = \dot{p}t$ avec $\dot{p}$ =10 et 250MPa/ns en a) et $\dot{p}$ =10MPa/ns en b). La matrice entourant les vides est rigide parfaitement plastique, de limite d'élasticité σ_0=100MPa, de masse volumique ρ=2700kg/m^3. La géométrie de la cellule élémentaire est telle que a_0=50μm, b_0=1500μm, conduisant à une porosité initiale f_0=1.1 10^{-3}.

driques de rayon initial a_0=50μm. Le rayon extérieur de la cellule élémentaire est b_0=1500μm conduisant à une porosité initiale f_0=1.1 10^{-3}. Les paramètres matériau de la matrice sont σ_0=100MPa, ρ=2700kg/m^3. Deux types de chargement axisymmétrique sont considérés dans cette partie:

- un chargement de déformation plane où l'on impose $D_{33} = 0$ et $\Sigma_{11} = \Sigma_{22} = \dot{p}t$ et pour lequel la réponse est indépendante de la longueur l_0,
- un chargement sphérique où $\Sigma_{11} = \Sigma_{22} = \Sigma_{33} = \dot{p}t$ et pour lequel nous étudions l'influence de la demi-longueur initiale l_0;

Le paramètre $\dot{p}$ est positif (vide en expansion) et représente le taux de chargement en contraintes

Déformation plane La Fig. 1.2a présente l'évolution de la porosité en fonction du temps pour deux valeurs de taux de chargement: $\dot{p}$ =10 et 250MPa/ns. La réponse quasi-statique est également reportée sur la figure. Les effets stabilisants de la micro-inertie sont clairement mis

en évidence, l'évolution en régime dynamique étant considérablement retardée comparativement à la réponse quasi-statique. Notons que cette dernière prédit une croissance instantanée du vide lorsque la contrainte appliquée $\Sigma_{11} = \dot{p}t$ atteint la valeur limite obtenue à partir de la surface de charge de Gurson (1.6), i.e. lorsque $\Sigma_{11} = \frac{\sigma_0}{\sqrt{3}} \ln\left(\frac{1}{f_0}\right)$. Compte tenu des paramètres considérés, le temps correspondant à l'expansion en régime quasi-statique est approximativement t =39ns (resp. 1.57ns) lorsque $\dot{p}$ =10MPa/ns (resp. $\dot{p}$ =250MPa/ns), voir Fig. 1.2a. Précisons enfin que, bien que la croissance de l'endommagement s'initie plus tôt lorsque $\dot{p}$ est plus grand, les effets de micro-inertie sont plus marqués pour les taux de chargement plus importants. En effet, la contrainte à appliquer pour observer un endommagement significatif au sein du matériau poreux est plus élevée lorsque $\dot{p}$ =250MPa/ns.

La Fig. 1.2b nous montre l'évolution des composantes du tenseur des contraintes totales pour le cas où $\dot{p}$ =10MPa/ns. Les contraintes dans le plan sont imposées, tandis que la contrainte axiale est obtenue à partir de la théorie, Eq (1.10). En raison des effets micro-inertiels, il apparaît que la contrainte axiale nécessaire pour maintenir le VER à sa longueur initiale, diminue aux grands temps, bien que le chargement dans le plan continue de croître. Cette tendance, vérifiée par calculs éléments finis, est un résultat marquant du travail de thèse, et a pu être révélé par l'approche théorique que nous avons développée. Un modèle construit à partir d'une approche 2D ne permet pas de restituer ces effets d'inertie dans la direction longitudinale, la contrainte dans cette direction ne pouvant être déterminée. Ce point est abordé en Annexe C.

Chargement sphérique La Fig. 1.3a présente l'évolution de la porosité en fonction du temps pour $\rho,\ a_0,\ f_0$ fixés, considérant plusieurs valeurs de longueur intiale l_0 dans l'intervalle [0-20 000]μm. Il apparaît que les effets d'inertie sont plus importants pour les vides longs, l'évolution de l'endommagement étant retardée lorsque l_0 augmente. La Fig. 1.3a révèle également

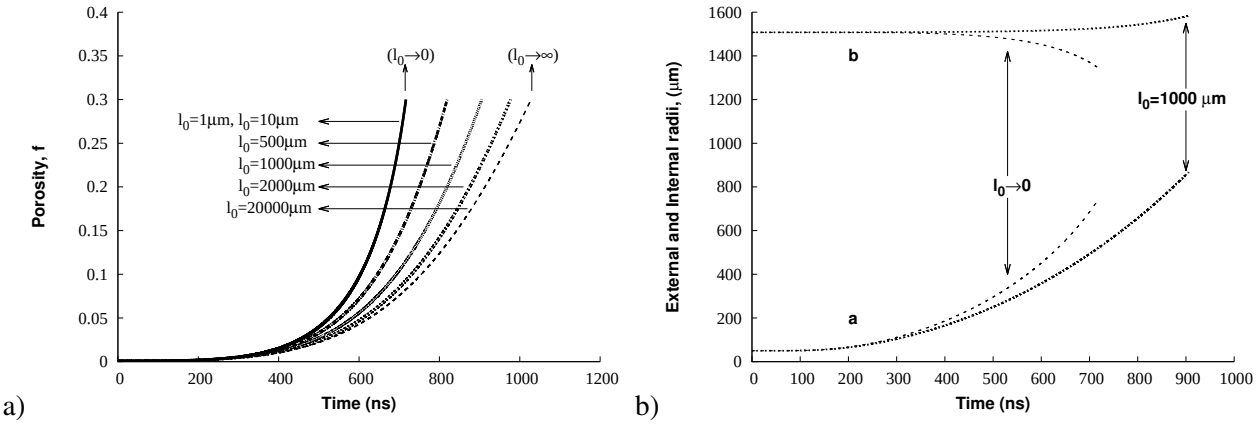

Figure 1.3: Effet de la longueur initiale de vide sur l'évolution a) de la porosité lorsque l_0 varie dans l'intervalle [1:20 000]μm et b) des rayons intérieur et extérieur du VER pour $l_0 \rightarrow 0$ et l_0 =1000μm. Le chargement est sphérique: $\Sigma_{11} = \Sigma_{22} = \Sigma_{33} = \dot{p}t$, avec $\dot{p}$=10MPa/ns. La matrice entourant les vides est rigide parfaitement plastique, de limite d'élasticité σ_0=100MPa, de masse volumique ρ=2700kg/m^3. La géométrie de la cellule élémentaire est telle que a_0=50μm, b_0=1500μm, conduisant à une porosité initiale f_0=1.1 10^{-3}.

que pour une cellule de longueur l_0 donnée, l'évolution de la porosité est encadrée par deux réponses asymptotiques. La première, obtenue pour $l_0 \geq$20 000μm correspond à la réponse de vides cylindriques très longs. Dans ce cas, l'évolution de la porosité coïncide avec le résultat illustré en Fig. 1.2a pour lequel $\Sigma_{11} = \Sigma_{22} = \dot{p}t$ et D_{33} =0 (déformation plane). Cependant, la contrainte axiale Σ_{33} est différente pour les deux cas de chargement. Il a en effet été montré qu'en raison des effets de micro-inertie, la contrainte axiale calculée en déformation plane est différente de $\dot{p}t$, cf. Fig. 1.2b.

La seconde réponse asymptotique illustrée en Fig. 1.3a est obtenue pour $l_0 \leq 1\mu$m. Dans ce cas, le modèle permet la description de vides cylindriques très minces pour lesquels la solution devient indépendante de la longueur initiale. Ce résultat peut être anticipé à partir de l'Eq (1.8) indiquant que les effets d'inertie liés à la longueur des vides disparaissent lorsque $l \rightarrow 0$. L'étude du cas de vides cylindriques très minces en expansion dynamique a révélé une situation tout à fait particulière illustrée en Fig. 1.3b montrant les évolutions des rayons intérieur a et extérieur b pour $l_0 \rightarrow 0$ et l_0 =1000μm. Dans le cas de matériaux poreux minces i.e $l \rightarrow 0$, l'augmentation de la porosité se réalise via une croissance du rayon de la cavité ac-

compagnée d'une réduction de la taille de l'enveloppe extérieure du VER. Cette tendance, tout à fait contrintuitive, n'est pas observée lorsque les effets d'inertie développés dans la direction longitudinale jouent un rôle important, comme c'est le cas par exemple pour $l_0 = 1000\mu$m sur la Fig. 1.3b.

1.4 Conclusion et perspectives

L'objectif de cette thèse est de proposer une modélisation de l'endommagement par croissance de cavités, pour des chargements dynamiques. Les matériaux poreux considérés contiennent des vides cylindriques parallèles représentatifs de structures perforées ou de matériaux architecturés de type nid d'abeille. Nous nous sommes particulièrement intéressés à l'influence de deux paramètres géométriques caractéristiques de la taille de la cellule (rayon et longueur), pour des cas de chargement axisymmétriques variés.

Les résultats obtenus par le modèle ont été vérifiés par comparaison à des simulations numériques menées sur des modèles éléments finis développés dans le doctorat. De nombreux cas de chargement ont été considérés et des résultats nouveaux ont été obtenus dans le cadre de la thèse. En particulier, lors d'un chargement de déformation plane, nous montrons que la contrainte axiale diminue alors que les contraintes dans le plan continuent d'augmenter. Ce résultat, traduisant que la contrainte nécessaire pour maintenir une structure poreuse à sa longueur initiale est réduite en raison des effets micro-inertiels, peut servir à préciser des éléments de dimensionnement de machines d'essais pour des essais dynamiques. Le cas du comportement sous chargement sphérique dynamique de structures minces a également révélé un comportement inattendu. L'endommagement croît par augmentation du rayon de vide, conjointement avec la réduction du rayon extérieur. Cette tendance est à attribuer uniquement aux effets de micro-inertie.

Au delà des cas de chargement abordés dans cette partie, le modèle a été testé pour des configurations supplémentaires pour révéler des tendances particulières. A titre d'exemples, le vide s'effondre lors d'une expansion biaxiale rapide alors qu'en traction dynamique, après une augmentation initiale, la porosité semble saturer lorsque les cavités sont suffisamment longues et les effets d'inertie importants.

Les travaux de doctorat appellent naturellement à poursuivre de nombreuses investigations. Nous n'en citerons que quelques unes. Tout d'abord, la matrice est considérée ici parfaitement plastique. Les effets stabilisants liés au chargement dynamique résulte donc, dans notre approche, uniquement des effets d'inertie liés à la taille des vides. La littérature a révélé que les effets visqueux peuvent jouer un rôle important dans l'évolution de l'endommagement en régime dynamique qui dépend, de ce fait, de l'influence combinée des effets visqueux et micro-inertiels. L'objectif premier, en poursuite de ce travail, consiste alors à inclure la sensibilité à la vitesse de déformation dans la réponse rhéologique de la matrice. Précisons d'ores et déjà que cela conduira à un ajustement de la contribution quasi-statique (i.e. indépendant des effets de micro-inertie) et n'affectera pas les expressions analytiques de la contribution inertielle obtenues dans ce travail. Après avoir étendu l'approche à la prise en compte des effets visqueux, il nous semble pertinent de mettre en œuvre le modèle à des fins de comparaison à des essais expérimentaux menés sur des matériaux ductiles dont le comportement dynamique de la matrice serait à identifier.

Dans notre approche, le VER adopté et champ de vitesse associés sont définis pour un cylindre creux. Cette configuration élémentaire nous permet notamment de mettre en évidence les effets de micro-inertie différenciés entre la contribution macroscopique dans le plan, et dans la direction longitudinale du cylindre. Une voie intéressante à l'extension de notre modélisation consiste à considérer des vides cylindriques noyés dans la matrice. Nous appuyant sur

des approches de la littérature, nous visons à adopter comme cellule élémentaire un domaine contenant le vide entouré d'une matrice déformable, à l'image du VER considéré par Morin et al. [27].

Enfin, les résultats obtenus au LEM3 pour le cas de vides sphériques ont révélé l'importance significative des paramètres de distribution de tailles de vides sur la réponse dynamique de matériaux poreux. Il serait alors également intéressant de considérer les effets de distribution en tailles (a) et en rapports de forme (l/a) sur la réponse dynamique d'une structure poreuse contenant une population hétérogène de vides cylindriques.

Context and Motivation of the thesis

This PhD is a part of the project "OUTCOME: A European Marie Curie Innovative Training Network (ITN-ETN)". The project has received funding from the European Union Horizon 2020 research and innovation programme under the Marie Sklodowska-Curie grant agreement n^0 675602. The consortium is a collaboration between University Carlos III Madrid, Spain (project coordinator), Technion, Israel, University of Lorraine, France and industrial partners CIMULEC, France and AEROSERTEC, Spain. The aim of this project is to train and develop eight Early Stage Researchers (PhD students) in developing novel solutions for the analysis and design of aerospace, defense and civilian structures subjected to extreme dynamic loading conditions.

Fracture in materials is due to action of thermo-mechanical loadings. Depending on the ability of materials to deform plastically before fracture determines whether the damage is ductile or brittle. The ductile damage in materials results from the interaction of three mechanisms: nucleation, growth and coalescence of voids. In this thesis, we are interested in damage of porous ductile materials under dynamic loading. This study concerns a wide range of fields such as civilian and military application (in the framework of the development of shock absorbing structures) or space application (for the study of the impact effect on satellites). For example, the aircraft sructures are vulnerable against loadings from impact, crash or explosion. These problems result in understanding the energy absorption in the structure and its

implementation in aircraft design. Safety is the major factor for the aircraft manufacturers. The aircraft industries are under deep investigation to employ different lightweight energy absorbers for suitable loading. When it comes to low weight and energy dissipation ability, honey comb structures are the state of the art structures for such applications. In biomechanics, the cylindrical like honey comb structures are widely used due to identical shape like bones. One of the example is illustrated in Fig. 1.4. The hollow cylindrical bones are known as Harvesian bones, which are stronger than reinforced concrete and exhibit an excellent resistance towards the compressive loading. Dynamic damage from impact of projectile on a target or explosion

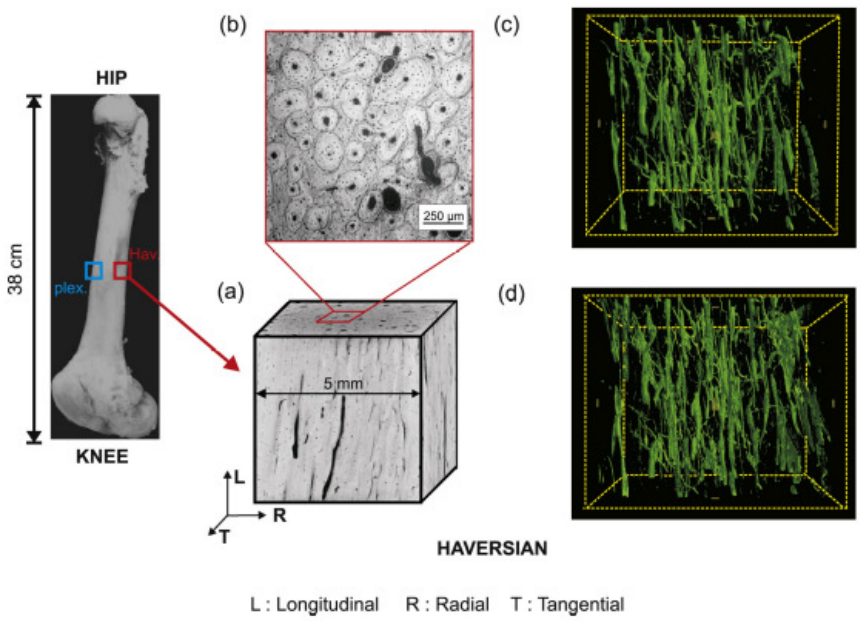

Figure 1.4: Compact bone made up of groups of concentric cylinders of bones, called Haversian units. a) Cubic sample from posterior cortex at mid-diaphysis with faces perpendicular to the longitudinal, radial and transverse directions. b) Optical micrograph of the sample surface showing Haversian bone. CT scan images of the Haversian bone specimen c) before fracture and d) after fracture (Mayya et al. [22]).

results in development of high strain rate and large stress. But classical approaches developed for quasi-static loads revealed only the effect of porosity to quantify damage. Under dynamic

loading, material particles situated near the cavities undergo strong acceleration. The micro-inertia effects induced by these strong acceleration developed at the local level play a major role in the macroscopic response and the development of damage in porous materials. Up to now, these effects at the local scale were mainly evaluated for porous materials containing spherical or spheroidal voids. Voids in metallic materials may reveal complex shapes which are not spherical or spheroidals. Within this context, we aim to consider cylindrical voided cells as representative of thick wall honeycomb structures or porous materials containing drilled holes. Finally, due to the development of additive manufacturing, the design of materials containing cylindrical voids is a possible way to create lightweight materials with high energy dissipation.

The aim of this work is to develop an analytical model for porous materials containing cylindrical voids. The goal is to elucidate several key points which are still under discussion (acceleration effect in the axial direction, micro-inertia effects, lengthscale effects, loading conditions, ...). In addition, the results obtained from the modeling are validated through comparison with finite element calculations conducted on unit cells using the finite element software Abaqus/Explicit.

The manuscript is organized as follows. A literature review is proposed in chapter 2. Then, the main steps of the dynamic homogenization procedure for porous materials are recalled in chapter 3. The trial velocity for the adopted cylindrical unit cell is also presented, followed by the expression of the macroscopic stress tensor that includes micro-inertia effects. To be noted, the matrix material is taken as rigid perfectly plastic (no strain hardening and no rate dependence of the matrix material). In chapter 4, we restrict the attention to axisymmetric loadings and present the results. The micro-inertia effects are exemplified considering various loading configurations such as plane strain case, hydrostatic case and various other loading paths. All results obtained from the approach are validated against finite element calculations

as presented in chapter 5. Finally, some conclusion and perspectives are discussed at the end of the manuscript.

Chapter 2

Literature review

2.1 Introduction

From decades, the description of void growth in ductile materials has received much attention around the scientific community mainly in quasi-static condition. But nature is dynamic, so it is significantly evident that the ductile fracture under intense dynamic loading is controlled to some extent by micro-inertia effects i.e, the kinetic energy stored in the matrix material in the vicinity of the void. The proposed literature review presents different aspects starting from ductile fracture in experimental works, theoretical studies about quasi-static and dynamic analysis of the void growth and importance of void shape. From the review, some conclusions will be drawn which will motivate my research.

2.2 Experimental works

Various researchers showed that the physical mechanisms of the ductile fracture are nucleation, growth and coalescence of voids, a scenario confirmed by experimental studies. Depending upon material and void configurations, different failure models are observed. The dynamic

fracture is visible in different situations associated with the impact of projectile on a target, detonation of an explosive or a sudden deposition of intense pulses of energy on the target. The ductile material undergoes very intensive loading which may exhibit high strain rates (in the order of $10^7\ s^{-1}$) and large stress levels (>$10GPa$) resulting in micro-voiding inside the material. Contrary to most quasi-static situations, in dynamic condition under large stress triaxiality voids are considerably growing, inducing large plastic deformation. In addition, the coalescence stage is mostly due to direct impingment (neigbhouring voids meet) while in quasi-static analyses, shear bands may connect small voids. The phenomenon of direct impingement is a consequence of micro-inertia effect, which stabilizes the flow in the neighbourhood of voids and prevent from early localization [17].

In the context of quasi-static loading, Weck and Wilkinson [49] developed a model material with cylindrical holes of micron dimensions, using laser drilling process through a single metallic sheet of Al-Mg alloy (AA5052), see Fig 2.1. The authors studied the influence of the initial hole geometry on the void growth and coalescence stages via consideration of various arrangements of voids in the middle of aluminium sheets under quasi-static condition. Fig. 2.1

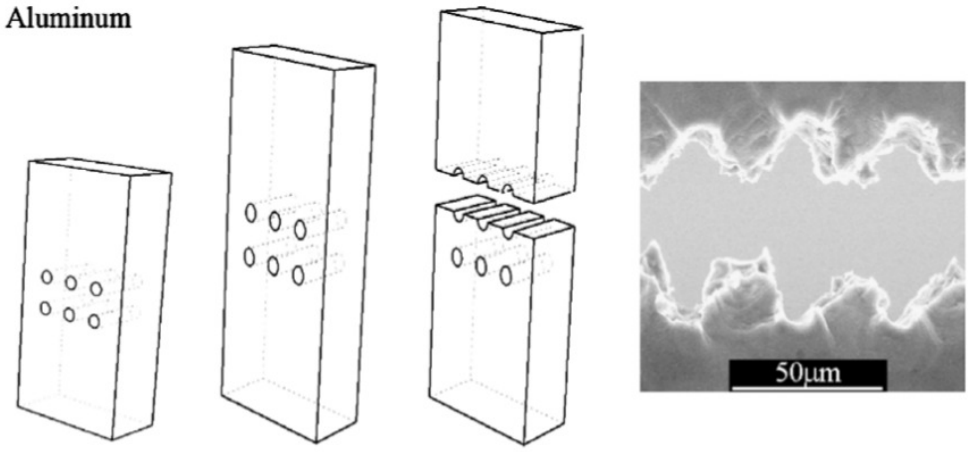

Figure 2.1: Failure mechanisms of Aluminium alloy (AA5052) with initial cylindrical voids generated using laser drilling process. The aluminium model fails by ductile fracture between the voids through internal necking. Weck and Wilkinson [49], Quasi-static condition.

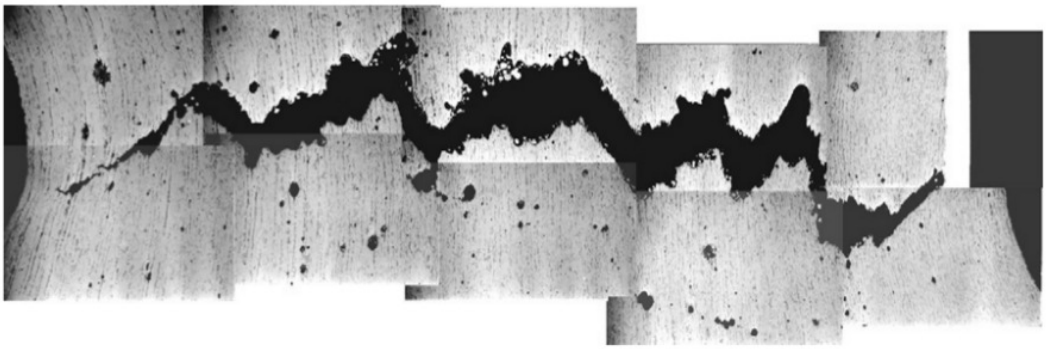

Figure 2.2: Ductile fracture in an initially dense steel due to void growth and coalescence of voids, Benzerga and Leblond [3], Quasi-static condition.

shows an array of 6 voids in 2 lines, the lines are oriented at 90^0 with respect to the tensile loading direction. In Fig. 2.1, it is visible that voids grow and coalescence occurs by internal necking of the ligament between voids.

Fig. 2.2 picturizes the ductile fracture observed for a round notched bar of low alloy steel, the material is initially considered as a dense steel with no crack. The zigzag crack goes "slant" as it approaches the free surfaces forming the shear lips that shows cup-cone fracture. The experiment was carried out by Benzerga et al. [2] and the authors observed that the damage occurs due to the evolution of voids (larger than $1\mu m$ in size). In this case, the void nucleates and grows. Coalescence is due to strain localization. The above two experimental works reveal that void growth and failure of ductile porous materials in quasi-static condition are interlinked.

Meyers and Aimone [24] studied the fracture behavior of nickel (Ni-200) during impact tests. In Fig. 2.3(a), the study revealed that the material undergoes ductile fracture due to spalling (spalling is a material failure due to the interaction of tensile stresses that develop inside a body when two rarefaction waves interact). In this study, Meyers and Aimone [24] observed that spherical voids grow, coalesce each other (mostly by direct impingement) and leads to fracture. Numerous spherical voids have been found during experiments, containing approximately 0.5 percent impurities in the material. Fig. 2.3(b) shows the formation of voids along the rolling direction like a string of particles. Later in the deformation process, voids are growing until

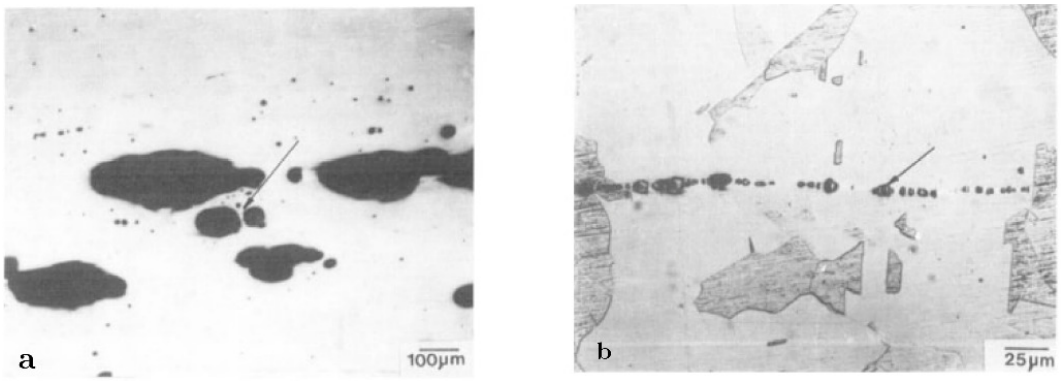

Figure 2.3: Dynamic fracture in nickel by spalling. (a) Spherical voids are induced during impact. They grow and coalesce by direct impingement mechanism. (b) Formation of a string of voids in nickel. Meyers and Aimone [24],

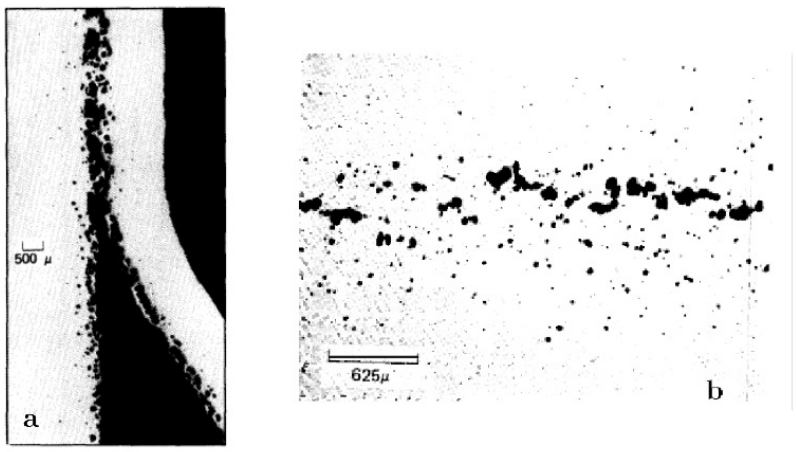

Figure 2.4: Dynamic damage in ductile material under impact test. (a) Ductile fracture by void coalescence. (b) Impingement of voids in impact-loaded specimens of 1145 aluminium. Curran et al. [7]

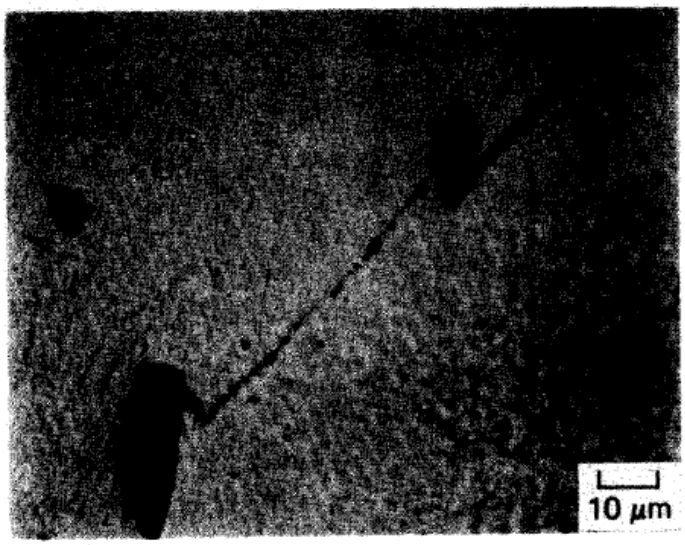

Figure 2.5: Voids coalescence by void sheet formation in AISI 4340 steel strained plastically. Curran et al. [7]

coalescence stage takes place leading to final failure by the creation of a scab.

The microscopic observations of Curran et al. [7] revealed that the coalescence process can be classified into two groups: direct impingement and localization between voids (strain localization). In Fig. 2.4(a), the coalescence process is simply direct impingement of the voids. In pure ductile metals (such as copper) after nucleation, void grows in a spherical manner to near direct impingement before localized ligament stretching completes the coalescence process. The above process occurs under dynamic loading, when the sample is submitted to planar impact (high stress triaxiality). Fig. 2.4(b) represents the void distribution in the spall plane in a 1145 aluminium. In some cases, the coalescence observed may occur through strain localization between voids, see Fig. 2.5.

Roy [33] investigated dynamic damage of high purity grade tantalum. Plate impact tests at various speeds and considering various target thicknesses were performed to generate damage and fracture in tantalum. The three main stages of damage and fracture (nucleation, void growth and coalescence) have been explained. Nevertheless, Roy studied particularly the problem of nucleation and growth of microvoids. Plate impact tests were carried out using a 80mm

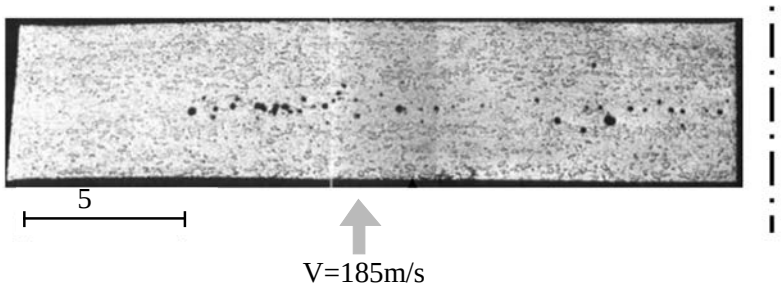

a)

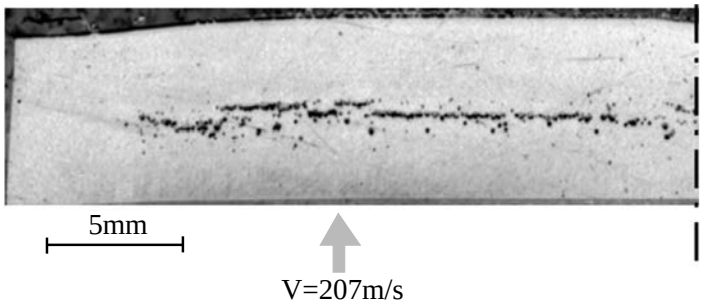

b)

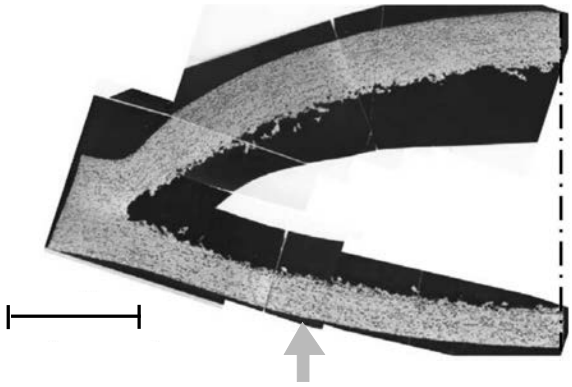

c)

Figure 2.6: Dynamic damage observed in tantalum under planar impact test at various impact velocites. Development of micro-voiding along the spall plane parallel to the impacted surface. The level of porosity is growing with increase in impacted velocity V. Complete fracture is observed at V=306m/s. Roy [33]

single stage gas gun providing a tensile stress as $5GPa < \sigma_{shock} < 30GPa$ and a shock rise time as $0.5\ \mu s < \Delta t_{shock} < 1.5\ \mu s$. The damage was observed from optical metallographic analyses. Fig. 2.6 illustrates the effect of impact velocity on the damage and fracture for the initially dense high purity grade tantalum. In Fig. 2.6(a), (v=$185m/s$) nucleation is observed to be randomly distributed in the vicinity of the spall plane parallel to the impacted surface. The investigation revealed that the voids remain spherical with diameter in the range $15\mu m$ to $400\ \mu m$. Fig. 2.6(b) shows as impact velocity increases (v=$207m/s$), the coalescence process is due to direct impingement mechanism. The interaction between voids during the growth stage seems to be delayed due to the micro-inertia effect. Fig. 2.6(c) shows that the complete fracture happens when the impact velocity is v=$306m/s$. In that case, the target is splitted in two parts. Under dynamic conditions, micro-inertia promotes rapid and large expansion which generates strong local acceleration of particles in the vicinity of cavities. As a consequence, the micro-inertia influences the overall behavior of the material. When micro-inertia is under consideration, the behavior of the porous material completely changes from quasi-static to dynamic (i.e, micro-inertia independent to micro-inertia dependent). Before presenting models in dynamic conditions, it is still interesting to focus on pioneering works dedicated to quasi-static conditions. Section 2.3.1 will focus on quasi-static theoretical studies. In section 2.3.2, a deeper analysis of works dedicated to dynamic conditions will be proposed.

2.3 Modeling

2.3.1 Quasi-static analysis on void growth

2.3.1.1 Introduction

The behavior of porous materials under quasi-static loading has been analyzed by several authors, since early works of McClintock [23], Rice and Tracey [32], Gurson [15], Budiansky et al. [4], Tvergaard [43] and Needleman and Tvergaard [28].

McClintock [23] investigated the growth of cylindrical and elliptical pores in an infinite viscous material. The author developed an approximate closed-form analytical expression for the void radius evolution and fracture criterion. Rice and Tracey [32] investigated the stage of void growth for mostly spherical void in an infinite matrix under general stress conditions. A variational principle has been proposed where the matrix is rigid-plastic (perfectly plastic or strain hardening). Results of McClintock [23] were retrieved for cylindrical voids when adopting the variational principle. Both analyses of McClintock [23] and Rice and Tracey [32] have revealed the exponential amplification of void growth by stress triaxiality. Budiansky et al. [4] have considered a viscous power law constitutive relationship for the matrix behavior, to identify the influence of the stress-triaxiality on the void radius growth. McClintock [23], Rice and Tracey [32], Budiansky et al. [4] were all considering dilute voids. In an engineering material, as observed in Fig. 2.1 to Fig. 2.6, voids are not isolated in the matrix phase, so the volume fraction of voids has to be integrated in the modelling. For that purpose, using a micro-mechanical approach, Gurson [15] derived an approximate yield criterion based on a trial velocity for porous materials with spherical and cylindrical voids under static conditions. The GTN (Tvergaard [43] and Needleman and Tvergaard [28]) model is extending the

Gurson model, which has been widely used for quasi-static investigation of fracture process in finite element calculations. Gologanu et al. [14] proposed a yield surface for porous material containing prolate voids, known as GLD model. The GLD yield surface can be viewed as an extension of the Gurson [15] model. A brief explanation of the quasi-static investigation from some of the previous works are pointed out in next pages.

2.3.1.2 McClintock Model

McClintock [23] developed a criterion for the fracture of cylindrical pores under prescribed stress at infinity. The criterion was developed for perfectly plastic, linear viscous materials and also extended to strain hardening material by extrapolation of the analysis. McClintock [23] observed that fracture takes place for very small porosity for both plastic and viscous flow with very strong inverse dependence of fracture strain on hydrostatic tension. McClintock [23] considered a porous medium subjected to stress loading at infinity. Calculations are done

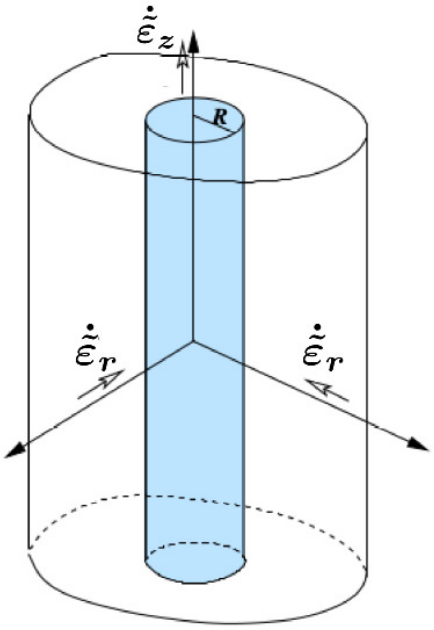

Figure 2.7: Cylindrical unit cell with inner radius R subjected to axial strain rate $\dot{\bar{\varepsilon}}_z$ and radial strain rate $\dot{\bar{\varepsilon}}_r$. The resulting strain rates are due to imposed stress at infinity, McClintock [23].

in the principal direction frames. McClintock [23] investigated the case of generalized plane strain with a hole in an infinite medium. The coalescence stage (and the associated fracture) is triggered when the radius of the hole reaches the mean spacing between voids. The problem is solved adopting cylindrical coordinates r, θ, z (Fig. 2.7). From the conservation of linear momentum in quasi-static conditions one obtains:

$$\frac{\partial \sigma_r}{\partial r} + \frac{\sigma_r - \sigma_\theta}{r} = 0 \tag{2.1}$$

For a von Mises material, Eq 2.1 becomes:

$$\frac{\partial \sigma_r}{\partial r} = -\frac{2\bar{\sigma}}{3r}\left(\frac{\dot{\varepsilon}_r}{\dot{\bar{\varepsilon}}} - \frac{\dot{\varepsilon}_\theta}{\dot{\bar{\varepsilon}}}\right) \tag{2.2}$$

where $\bar{\sigma}$ and $\dot{\bar{\varepsilon}}$ are the equivalent stress and strain rate.

From compatibility condition and incompressibility of the matrix, the velocity components are expressed as:

$$v_r = \frac{A}{r} - \frac{\dot{\bar{\varepsilon}}_z}{2} r \tag{2.3}$$

$$v_z = \dot{\bar{\varepsilon}}_z z \tag{2.4}$$

where $A = -R^2(\dot{\bar{\varepsilon}}_r + \dot{\bar{\varepsilon}}_z/2)$. $\dot{\bar{\varepsilon}}_r$ and $\dot{\bar{\varepsilon}}_z$ are the local strain rate at the void surface. The strain rate components in the matrix material are defined as:

$$\dot{\varepsilon}_r = -\left(\frac{R^2}{r^2}\right)\left(\dot{\bar{\varepsilon}}_\theta + \frac{\dot{\bar{\varepsilon}}_z}{2}\right) - \frac{\dot{\bar{\varepsilon}}_z}{2} \tag{2.5}$$

$$\dot{\varepsilon}_\theta = \left(\frac{R^2}{r^2}\right)\left(\dot{\bar{\varepsilon}}_\theta + \frac{\dot{\bar{\varepsilon}}_z}{2}\right) - \frac{\dot{\bar{\varepsilon}}_z}{2} \tag{2.6}$$

where the condition $(\dot{\bar{\varepsilon}}_\theta + \dot{\bar{\varepsilon}}_z + \dot{\bar{\varepsilon}}_r = 0)$ has been used. R is the radius of the cylindrical void. Using Eqs (2.2), (2.5), (2.6) and substituting in the equilibrium equation, Eq (2.1), the void growth is expressed as:

$$\frac{\dot{R}}{R_0} = \sqrt{3}\dot{\varepsilon}_r^\infty \sinh\left[\frac{\sqrt{3}\sigma_r^\infty}{\sigma_r^\infty - \sigma_z^\infty}\right] + \dot{\varepsilon}_r^\infty \tag{2.7}$$

The ductile fracture model of McClintock has been recently used as the basis for the formulation of a damage plasticity model by Reboul and Vadillo [31]. Adopting a hollow cylinder as the unit cell and based on Taylor series expansion, the authors provided a closed form macroscopic expression for the response of strain rate power-law materials.

2.3.1.3 Gurson model

Gurson [15] developed an approximate plastic constitutive theory for porous materials. An approximate velocity field is adopted, similar to Rice and Tracey [32] in such a way that the velocity field satisfies the kinematic boundary conditions on the external surface of the unit cell. Homogenous kinematic boundary conditions are considered:

$$\boldsymbol{v} = \mathbf{D} \cdot \boldsymbol{x} \tag{2.8}$$

where $\mathbf{D}$ is the macroscopic strain rate tensor. The material is assumed incompressible and the volume change of the RVE is only due to void growth. The approximate yield criterion is initially proposed for rigid perfectly plastic materials. Gurson studied the case of a matrix material containing both long circular cylindrical voids (Fig. 2.8) and spherical voids (Fig. 2.9).

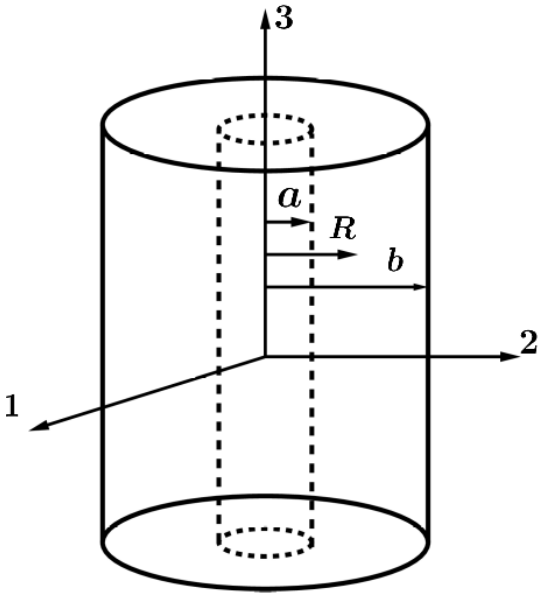

Figure 2.8: Long circular cylindrical unit cell (inner radius 'a' and outer radius 'b') with cylindrical void embedded inside. The porosity of the unit cell is $f = (a/b)^2$. The matrix is rigid perfectly plastic, Gurson [15].

The approximate velocity is developed in such a manner that the shear and dilatation components are independent. The velocity field for cylindrical void is expressed as:

$$\boldsymbol{v} = \hat{\mathbf{D}} \cdot \boldsymbol{x} + B\tilde{\boldsymbol{x}} \tag{2.9}$$

where $B = \frac{\mathrm{tr}(\mathbf{D})}{2}\left(\frac{b}{r}\right)^2 - \frac{\mathbf{D}_{33}}{2}$, $\tilde{\boldsymbol{x}} = x_1\mathbf{e}_1 + x_2\mathbf{e}_2$ and $\boldsymbol{x} = x_1\mathbf{e}_1 + x_2\mathbf{e}_2 + x_3\mathbf{e}_3$

$\hat{\mathbf{D}}$ is a strain rate tensor expressed as:

$$\hat{\mathbf{D}} = \begin{bmatrix} \frac{D_{11}-D_{22}}{2} & D_{12} & D_{13} \\ D_{12} & \frac{D_{22}-D_{11}}{2} & D_{23} \\ D_{13} & D_{23} & D_{33} \end{bmatrix}, \tag{2.10}$$

Based on the plastic dissipation evaluated from the velocity field, Gurson develops a yield

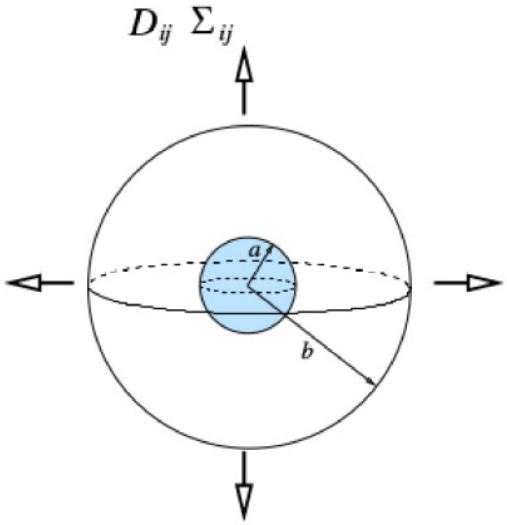

Figure 2.9: Hollow sphere model with a spherical void embedded inside a spherical shell having inner radius 'a' and outer radius 'b'. The porosity of the unit cell is $f = (a/b)^3$, Gurson [15].

function for the circular cylindrical void which takes the analytic form:

$$\Phi = C_{eqv}\left(\frac{\boldsymbol{\Sigma}_{eqv}}{\sigma_0}\right)^2 + 2f\cosh\left(\frac{\sqrt{3}}{2}\frac{\boldsymbol{\Sigma}_{\gamma\gamma}}{\sigma_0}\right) - 1 - f^2 \tag{2.11}$$

where $\boldsymbol{\Sigma}$ represents the stress tensor and σ_0 is the matrix yield stress (constant for perfectly plastic material). $\boldsymbol{\Sigma}_{\gamma\gamma} = \Sigma_{11} + \Sigma_{22}$, $\boldsymbol{\Sigma}_{eqv} = \sqrt{\frac{3}{2}\Sigma'_{ij}\Sigma'_{ij}}$, where $\boldsymbol{\Sigma}'$ is the deviatoric part of the cauchy stress tensor. C_{eqv} is function of f (volume fraction of pores). When f tends to zero, the yield function reduces to the von Mises yield function. The Gurson yield function for cylindrical voids in plane strain flow for rigid perfectly plastic material is presented in Fig. 2.10, see more details in Gurson [15]. One can observe that as the porosity increases, the elastic domain shrinks.

Even though the Ph.D focuses only on cylinder, one has to mention that in the literature, most of the works are dealing with spherical void shape. For spherical void, the microscopic velocity

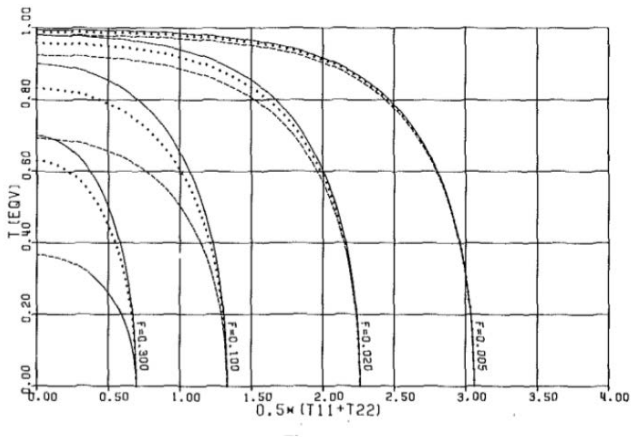

Figure 2.10: Gurson yield function for cylindrical voids in plane strain loading conditions. The yield loci are presented for three different loading cases. Axi-symmetric, plane strain and generalized plane strain conditions are represented by solid lines, dashed lines and dotted lines respectively for various porosities (f in the range 0.005 to 0.3). In the present figure $T = \Sigma/\sigma_0$ is the normalized macroscopic stress tensor, Gurson [15]

field usually adopted in the literature can be split into two parts:

$$v = v^s + v^v \tag{2.12}$$

where the first part represents shape change at constant volume (v^s) and the second part represents the volume change at constant shape (v^v), similar like cylindrical void. In that case, the yield function for spherical voids takes the form:

$$\Phi = \left(\frac{\boldsymbol{\Sigma}_{eqv}}{\sigma_0}\right)^2 + 2f\cosh\left(\frac{1}{2}\frac{\boldsymbol{\Sigma}_{nn}}{\sigma_0}\right) - 1 - f^2 \tag{2.13}$$

where $\Sigma_{nn} = tr(\boldsymbol{\Sigma}) = 0$, '$tr$' represents the trace operator. Again, when f=0, the von Mises yield function is retrieved.

Under spherical loading, the yield stress of porous material with spherical voids is:

$$\mathbf{\Sigma}_{nn} = 2\sigma_0 \ln\left(\frac{1}{f}\right) \tag{2.14}$$

The approximate yield functions proposed by Gurson for spherical and cylindrical voids have been adopted widely in the literature.

2.3.1.4 Gurson Tvergaard and Needleman model (GTN model)

Needleman and Tvergaard [28] have modified the Gurson model by comparing the prediction of the model with FE cylindrical unit cell containing a spherical void. Needleman and Tvergaard [28] introduce three parameters so that the approximate yield function takes the form:

$$\Phi = \left(\frac{\Sigma_{eqv}}{\sigma_0}\right)^2 + 2fq_1 \cosh\left(\frac{q_2}{2}\frac{\Sigma_{nn}}{\sigma_0}\right) - 1 - q_3 f^2 \tag{2.15}$$

where q_1, q_2 and q_3 are parameters that adopt various forms in the literature. Needleman and Tvergaard [28] proposed the following constant values q_1=1.5, q_2=1, q_3=q_1^2 while other authors showed that the q-parameters are depending on triaxiality (Vadillo and Fernández-Sáez [44]). When q_1=q_2=q_3=1, then Eq (2.15) takes the form of Gurson model Eq (2.13). From the associated flow rule, the macroscopic strain rate is perpendicular to the yield surface:

$$\mathbf{D} = \dot{\kappa}\frac{\partial \Phi}{\partial \mathbf{\Sigma}} \tag{2.16}$$

The parameter $\dot{\kappa}$ represents the plastic multiplier satisfying the Kuhn-Tuker conditions (Simo and Hughes [37]): $\Phi \leq 0$, $\dot{\kappa} \geq 0$, $\Phi\dot{\kappa} = 0$. To analyse the porosity evolution during loading,

an evolution law for f is defined based on the incompressibility of the matrix material:

$$\dot{f} = (1 - f)tr\mathbf{D} \tag{2.17}$$

In the above works, micro-inertia effects are not considered. In case of very high strain rates applications such as ballistic impacts, high speed forming processes, design of shock wave mitigation devices, crash tests, etc. the above quasi-static approaches have some limitations, the overall response being not related to the size of voids. The next section focuses on the dynamic behavior of porous materials investigated by several researchers aiming at overcome these limitations.

2.3.2 Dynamic analysis for porous materials

2.3.2.1 Introduction

Under dynamic conditions, intense local acceleration fields are developed in the vicinity of the void surface which will influence the overall behavior of the material. Several authors proved that micro-inertia tends to delay the porosity growth. I will briefly discuss some of the works and later in this section, I will propose a more extensive description of a limited number of contributions.

Carroll and Holt [5] investigated the inertia effect on the behavior of porous aluminium media (with spherical voids) under spherical compressive loading. The work is restricted to elastic perfectly plastic matrix. Carroll and Holt [5] constructed a rate-dependent pore-collapse relationship which involves the matrix material properties, the pore geometry and the loading. The above study revealed an analytical void collapse law including micro-inertia effects under pure hydrostatic compression. The macroscopic pressure was found to be sum of a quasistatic

part (micro-inertia independent) and a dynamic part (micro-inertia dependent) scaled by the square of the void radius and the matrix mass density. The comparison of the model prediction with finite-difference calculations was carried out. Klöcker and Montheillet [18] analyzed the void growth in a viscoplastic material. Cylindrical and spherical geometries under axisymmetric and spherical loadings were considered respectively. The authors investigated both static and dynamic responses. The matrix was linear viscous. Cortes [6] performed the analytical modeling of the dynamic growth of microvoids, which is an extension of the static and dynamic pore-collapse relationship obtained for ductile porous materials by Carroll and Holt [5]. The study was carried out under hydrostatic loading, including the effect of material viscosity, strain hardening and thermal dependency. Cortes [6] concluded that the porosity evolution is governed by viscous effect at the beginning stage and controlled by micro-inertia at the late stage of the deformation process. The investigation also revealed that the thermal softening has only very small influence on the dynamic behavior at high strain rate due to the localization of heat near the surface of the voids. The authors considered aluminium and copper-like materials. Ortiz and Molinari [30] considered a spherical void in an unbounded solid under spherical tensile loading to investigate the effect of micro-inertia. In this case, the study included both viscous and micro-inertia effects, adding the strain hardening sensitivity. The study revealed that both effects play an important role in the porosity growth i.e, the early stage is governed by viscous effects and the late stage is dominated by micro-inertia, confirming the conclusion of Cortes [6]. The main objective of the authors was to define a dimensionless parameter able to capture the interaction between the viscous and inertia effects and at the same time to clarify the role of both effects in the dynamic growth. Tong and Ravichandran [38, 39] investigated the dynamic behavior of spherical pores in porous materials under spherical loading for elastic-viscoplastic materials. The quasistatic and dynamic responses were examined. The quasistatic

analysis was developed for both rate-independent and rate-dependent matrix. The dynamic part or micro-inertia inherited part was evaluated by an approximate method. The effect of the dynamic loading rate, strain rate sensivity, strain hardening and thermal softening was also investigated by the authors.

From the previous mentioned contributions, the dynamic behavior of porous material was mostly investigated under spherical loading. To consider more general loading conditions, dynamic homogenization schemes have been proposed. Wang [46] studied the dynamic behavior of porous materials, considering a hollow sphere as the representative volume element of the medium. This model is not restricted to spherical loading. Surface energy effect and temperature softening are accounted for. When temperature and surface energy are disregarded, the relation proposed by Carroll and Holt [5] is retrieved. The numerical analyses were carried out for various initial distentions, initial temperature and material rate sensitivities, to illustrate the temperature dependency, the role of the matrix viscoplastic behavior and inertial effects on void growth. Note that the distention α is linked to the porosity f via the relationship:

$$\alpha = \frac{1}{1-f} \tag{2.18}$$

Wang [47] and Wang and Jiang [48] revisited the work of Wang [46], by adopting the general trial velocity field of Rice and Tracey [32]. From the energy conservation, part of the external work is dissipated by plastic deformation while the stored kinetic energy ensures the balance. In Wang and Jiang [48] axisymmetric loading conditions were treated and for the first time, the dynamic stress was not only spherical. So an extension of the Gurson model to dynamic condition was obtained. In Wang [47], a definition for the macroscopic stress and strain rate was proposed, both quantities being work conjugated. The proposition was still exemplified by

considering axisymmetric loadings (spherical and shear loadings).

Following the series of work proposed by Wang [46, 47] and Wang and Jiang [48], Molinari and Mercier [26] proposed a dynamic homogenization for the behavior of porous materials with spherical void. An explicit relationship was proposed between the macroscopic stress and strain rate tensors. The micro-mechanical modeling accounting for micro-inertia and viscoplasticity was obtained for general states of stress. The macroscopic stress was found to be the sum of two contributions: a static contribution and a dynamic part. The static part can be evaluated using any yield potential or flow surface. The micro-inertia part was derived from the trial velocity field of Gurson [15] and Rice and Tracey [32] for spherical voids. Like the work of Cortes [6] or Ortiz and Molinari [30], here also the results prove that the early stage of the void growth is governed by viscous effect and late stage by the micro-inertia effect. This modeling is further extended by Czarnota et al. [9, 8], Jacques et al. [16, 17], Czarnota et al. [10].

More specifically, Czarnota et al. [9] adopted the model of Molinari and Mercier [26] to investigate spall fracture due to microvoiding in tantalum. They extended the theoretical model to account also for nucleation of voids. Czarnota et al. [8] implemented the model in FE software (ABAQUS) so the configuration of Roy [33] was analyzed in details. The experimental velocity profiles of the free surface for various impact velocities were retrieved. Jacques et al. [16] adopted the micro inertia model for the same grade of tantalum. In this work, the mean void size evaluated from the theory was found to correlate with experiments of planar impact. Jacques et al. [17] proposed to illustrate the effect of micro-inertia on dynamic crack propagation. It was known from the literature that when adopting Gurson model, the strain localization process develops in a single row of elements. It is shown that when revisiting the dynamic crack propagation in a notch specimen or in a plate, the porosity development is spread in the vicinity of the crack surface. Therefore, finite element calculations in dynamic conditions are shown to

be mesh insensitive when mesh is dense enough. This aspect clearly illustrates the regularization feature of micro-inertia. Indeed with micro-inertia, the delay in porosity growth enables such regularization process. As main outcome of the work of Jacques et al. [16], the size of the damage zone in a notched specimen was found to be scaled by the size of the pre-existing voids. For pre-cracked plate, the fracture toughness was shown to be related to the initial void size. The crack speed is also limited due to micro-inertia and can be compared to experiments. Czarnota et al. [10] investigated the shock wave propagation in a porous material. From the dynamic analysis, the shock width is also controlled to some extent by the characteristic size of the voids. An interesting finding is the amount of plastic dissipation which increases in porous material under dynamic conditions when compared to dense materials. It is also shown that the shock width in porous material can be larger than in dense materials. A scaling law was finally proposed for the shock width with a clear link to the initial size and initial porosity. With porous materials containing sufficiently large voids, one can have plastic dissipation combined with lower acceleration. These are beneficial aspects for shock mitigation.

After a rapid presentation of a limited selection of papers of the literature, I propose in the following section to develop in more details four contributions which are of fundamental interest for my PhD. First, I will summarize the contribution of Carroll and Holt [5] to highlight the structure of micro-inertia term. Secondly, I will detail the homogenization procedure of Molinari and Mercier [26]. Next, I will present the Leblond and Roy [20] approach, which considers a porous materials with cylindrical voids subjected to dynamic loading. Finally, the investigation proposed by Molinari et al. [25] for the coalescence stage with a cylindrical RVE will be shortly discussed.

2.3.2.2 Carroll and Holt Model

As mentioned in the introduction part of section 2.3.2, Carroll and Holt [5] investigated the dynamic compaction of porous aluminium. For that purpose, the RVE is a hollow sphere model (see Fig. 2.9), with inner radius 'a' and outer radius 'b'. Under dynamic compression P, the mechanical analysis of the pore-collapse can be splitted in three phases: the first part where the RVE remains elastic, a second stage where the inner part of the RVE ($r < c$) is under plastic regime while the outer part ($r > c$) remains elastic. The surface $r = c$ denotes the interface between elastic and plastic regions. Finally when the loading is large, the RVE is entirely under plastic regime. The authors defined the governing equation of the three stages from the conservation of linear momentum (with the acceleration term) assuming also that the matrix phase is perfectly plastic (Y being the yield stress):

(i) Elastic phase:

$$\tau^2 Y Q(\ddot{\alpha}, \dot{\alpha}, \alpha) = P - \frac{4G(\alpha_0 - \alpha)}{3\alpha(\alpha - 1)} \tag{2.19}$$

where,

$$\tau^2 = \rho {a_0}^2 / [3Y(\alpha_0 - 1)^{2/3}] \tag{2.20}$$

$$Q(\ddot{\alpha}, \dot{\alpha}, \alpha) = -\ddot{\alpha}[(\alpha - 1)^{-1/3} - \alpha^{-1/3}] + \frac{1}{6}\dot{\alpha}^2[(\alpha - 1)^{-4/3} - \alpha^{-4/3}] \tag{2.21}$$

ρ represents the matrix mass density, τ has the physical dimension of time and α the distention as defined in Eq 2.18.

(ii) Elastic-plastic phase:

$$\tau^2 Y Q(\ddot{\alpha}, \dot{\alpha}, \alpha) = P - \frac{2}{3}Y(1 - [2G(\alpha_0 - \alpha)]/(Y\alpha) + \ln\{[2G(\alpha_0 - \alpha)]/[Y(\alpha - 1)]\}) \tag{2.22}$$

where G represents the shear modulus.

(iii) Plastic phase:

$$\tau^2 Y Q(\ddot{\alpha}, \dot{\alpha}, \alpha) = P - \frac{2}{3} Y \ln[\alpha/(\alpha - 1)] \tag{2.23}$$

From the above expressions, the dynamic pore collapse model leads to an expression of the form:

$$P = P_{eq}(\alpha) + \tau^2 Y Q(\ddot{\alpha}, \dot{\alpha}, \alpha) \tag{2.24}$$

where $P_{eq}(\alpha)$ can be viewed as the static part and $\tau^2 Y Q(\ddot{\alpha}, \dot{\alpha}, \alpha)$ the dynamic contribution due to micro-inertia. The expression for $P_{eq}(\alpha)$ for all three phases are listed in Table 2.1. The dynamic pressure is scaled by the mass density ρ, the square of the void size a, related to the distension α and its first and second time derivatives $\dot{\alpha}$ and $\ddot{\alpha}$. Note that this kind of rate dependency is a signature of micro-inertia.

Carroll and Holt [5] validated the theoretical modeling with recourse to numerical simulations based on the finite difference calculations. Fig. 2.11 reveals the investigation of Carroll and Holt on porous aluminium subjected to spherical compression. Various pressure rates ($\dot{P}$= 2.5, 5, 10 and 20 MPa/ns) are considered, the initial distention being α=1.8 (i.e, f=0.44). It is shown that the prediction of the model gives good agreement when compared to numerical results.

Table 2.1: Expression of the static pressure $P_{eq}(\alpha)$ for the elastic, elastic-plastic and plastic phases during dynamic compaction, from Carroll and Holt [5]

Elastic	$P_{eq}(\alpha) = [4G(\alpha_0 - \alpha)]/[3\alpha(\alpha - 1)]$
Elastic-plastic	$P_{eq}(\alpha) = \frac{2}{3} Y(1 - [2G(\alpha_0 - \alpha)]/(Y\alpha) + \ln\{[2G(\alpha\alpha_0 - \alpha)]/[Y(\alpha - 1)]\})$
Plastic	$\frac{2}{3} Y \ln[\alpha/(\alpha - 1)]$

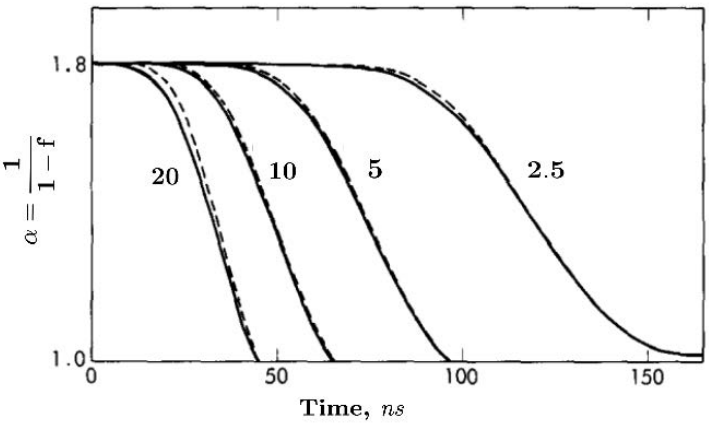

Figure 2.11: Evolution of distension with time during the pore collapse of an aluminium material of initial distention, α=1.8, with applied loading rates $\dot{P}$=2.5, 5, 10 and 20 MPa/ns. Solid line shows the predictions of the analytical model. Dashed lines show the results of the finite difference calculations, Carroll and Holt [5].

2.3.2.3 Molinari and Mercier Model-2001

Molinari and Mercier [26] investigated the dynamic behavior of porous material with spherical voids by means of a micro-mechanical approach. From the principle of virtual work, the macroscopic stress was defined which accounts for the acceleration contribution. The explicit relationship was derived starting from the conservation of linear momentum in dynamic condition:

$$\mathbf{div}\sigma = \rho\gamma \tag{2.25}$$

where ρ is the mass density, γ is the acceleration field and σ is the Cauchy stress tensor.

A homogenous kinematic boundary condition is applied on the external boundary of the RVE, so that

$$\boldsymbol{v} = \mathbf{D} \cdot \boldsymbol{x} \tag{2.26}$$

" $\cdot$ " denotes the simple contracted or dot product.

From the principle of virtual work including the acceleration term, Molinari and Mercier [26] found that the macroscopic stress $\mathbf{\Sigma}$ and macroscopic strain rate $\mathbf{D}$ are work conjugated:

$$\mathbf{\Sigma} : \mathbf{D} = \langle \boldsymbol{\sigma} : \mathbf{d} \rangle + \left\langle \frac{1}{2} \rho \frac{d|v|^2}{dt} \right\rangle \tag{2.27}$$

where (:) denotes the twice contracted product.

The macrostress was found to be defined by:

$$\mathbf{\Sigma} = \langle \boldsymbol{\sigma} \rangle + \left\langle \rho \gamma \otimes x \right\rangle \tag{2.28}$$

The macroscopic strain rate D is the volume average of microscopic strain rate, d:

$$\mathbf{D} = \langle \mathbf{d} \rangle \tag{2.29}$$

where $\langle \bullet \rangle = \frac{1}{|V|} \int_V \bullet \, \mathrm{d}V$, $|V|$ denotes the volume of the RVE, '$\otimes$' is the tensor product and 'x' the position of the particle. As the problem is dynamic (inertia dependent), so the static definition $\mathbf{\Sigma}$=$\langle \boldsymbol{\sigma} \rangle$ is no more valid. This statement is the main difference with a previous study developed by Wang [47]. In Eq (2.28), $\boldsymbol{\sigma}$ is the solution of the dynamic problem. As a consequence, under general loading condition of type Eq (2.26), it is impossible to find the exact solution. One can obtain such solution for instance by considering a hollow sphere RVE under spherical loading.

A second approach was proposed in Molinari and Mercier [26] using a trial velocity field. The local material behavior was assessed by the introduction of a potential $\Phi(x, \mathbf{d})$, so that the

microscopic stress and strain rate tensors are connected through the relation:

$$\boldsymbol{\sigma} = \frac{\partial \Phi(x, \mathbf{d})}{\partial \mathbf{d}} \tag{2.30}$$

Applying once again the principle of virtual work to the RVE subjected to an increment of macroscopic strain rate $\delta\mathbf{D}$, the symmetric part of macroscopic stress $\boldsymbol{\Sigma}$ is expressed as the sum of micro inertia independent term, $\boldsymbol{\Sigma}^{static}$ and micro inertia independent term, $\boldsymbol{\Sigma}^{dyn}$.

$$(\boldsymbol{\Sigma})^s = \boldsymbol{\Sigma}^{static} + (\boldsymbol{\Sigma}^{dyn})^s \tag{2.31}$$

where,

$$\boldsymbol{\Sigma}^{static} = \frac{\partial \langle \Phi \rangle}{\partial \mathbf{D}} \text{ and } (\boldsymbol{\Sigma}^{dyn})^s = \frac{1}{\Omega} \int_{\Omega} \rho\gamma . K(x, \mathbf{D}) d\Omega \tag{2.32}$$

where γ represents here the acceleration of a material particle evaluated from the trial velocity field and $(\cdot)^s$ represents the symmetric part of the tensor. $K(x, \mathbf{D})$ is a third order tensor which links the increment of the macro-strain rate $\delta\mathbf{D}$ to the increment of velocity $\delta\boldsymbol{v}$:

$$\delta\boldsymbol{v} = K(x, \mathbf{D}) : \delta\mathbf{D} \tag{2.33}$$

To evaluate the static term, Molinari and Mercier [26] adopted the macroscopic potential, $\langle \Phi \rangle$ proposed by Olevsky and Skorohod [29]:

$$\langle \Phi \rangle = \frac{A}{m+1}(1-f)\mathrm{W}^{m+1} \tag{2.34}$$

where $\mathrm{W} = \sqrt{\varphi\gamma^2 + \psi e^2}$, $\varphi = (1-f)$, $\psi = \frac{2}{3}(1-f)^2/f$, $\gamma = \sqrt{\mathbf{D}' : \mathbf{D}'}$, $e = tr(\mathbf{D})$ and $\mathbf{D}'$ represents the deviatoric part of the macroscopic strain rate $\mathbf{D}$.

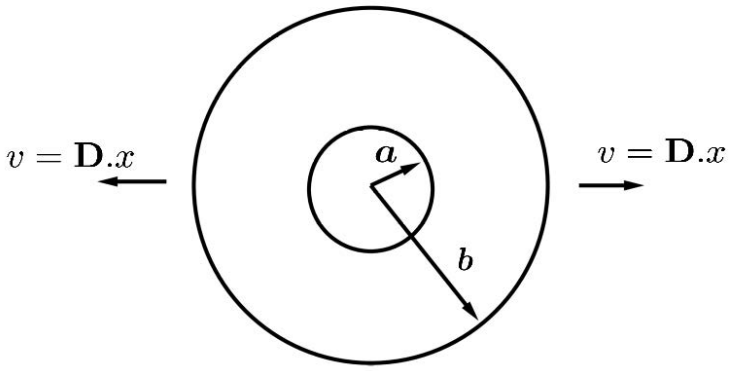

Figure 2.12: A hollow sphere as a representative volume element with internal radius a and external radius b. The matrix behavior is viscoplastic and the porosity $f = a^3/b^3$. Molinari and Mercier [26].

To obtain an analytical expression of $\mathbf{\Sigma}^{dyn}$, Molinari and Mercier [26] considered the approximate velocity field proposed by Gurson (1977) or Rice and Tracey [32]:

$$\boldsymbol{v} = \mathbf{D}^{'}.\boldsymbol{x} + B\boldsymbol{x} \tag{2.35}$$

where, $B = D_m\left(b/r\right)^3$ and $D_m = \frac{1}{3}tr(\mathbf{D})$. After some mathematical developments, Molinari and Mercier [26] obtain:

$$\begin{aligned}(\mathbf{\Sigma}^{dyn})^s = \rho a^2\Bigg[&\frac{1}{5}(f^{-2/3}-f)\left(\dot{\mathbf{D}}^{'}+\mathbf{C}-\frac{1}{3}tr(\mathbf{C})\mathbf{I}\right)+(f^{-2/3}-1)D_m\mathbf{D}^{'}\\&+\frac{1}{6}(f^{-2/3}-1)(\mathbf{D}^{'}:\mathbf{D}^{'})\mathbf{I}-(f^{-2/3}-f^{-1})\dot{D}_m\mathbf{I}\\&+\left(3f^{-1}-\frac{5}{2}f^{-2/3}-\frac{1}{2}f^{-2}\right)D_m^2\mathbf{I}\Bigg]\end{aligned} \tag{2.36}$$

with $\mathbf{C} = \mathbf{D}^{'}:\mathbf{D}^{'}$ and $\mathbf{I}$ is the second order tensor.

This term is scaled by the mass density ρ, the square of the void radius a. It contains quadratic terms in $\mathbf{D}$ and linear terms in $\dot{\mathbf{D}}$. Once again, this is the classical signature of micro-inertia

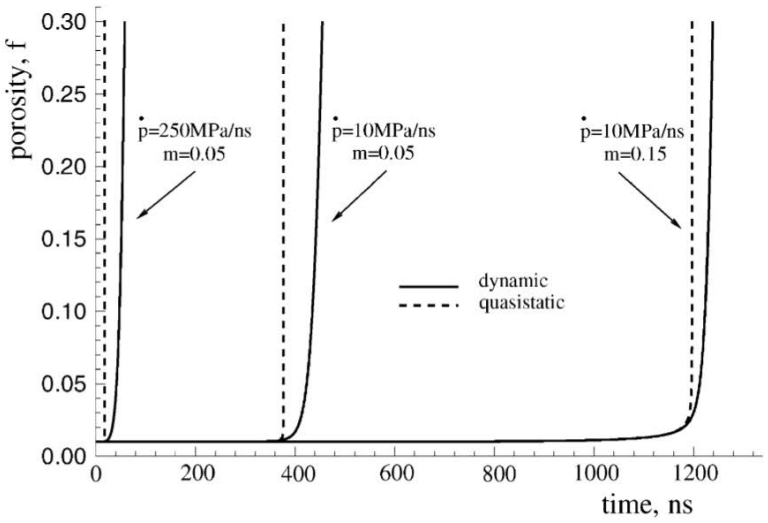

Figure 2.13: Porosity versus time evolution for both quasi-static and dynamic models. The initial porosity is f_0=0.01. Two loading rates ($\dot{p}$=10MPa/ns, 250MPa/ns) and two strain rate sensitivities (m=0.05, 0.15) are tested for spherical loading. Molinari and Mercier [26]

for porous material. The relation is designed in such a way that as inertia effect is reduced to zero, the total macroscopic stress is completely controlled by the static term (see Eq (2.31)). The evolution of the porosity is evaluated using the incompressibility of the matrix, Eq (2.17). Molinari and Mercier [26] considered a viscous plastic porous matrix under various loading conditions: hydrostatic expansion, compression and axisymmetric loadings. For hydrostatic condition, Fig. 2.13 presents the porosity evolution for a material representative of an aluminium for two loading rates, $\dot{p}$=10MPa/ns and 250MPa/ns and for two strain rate senstivities, m=0.05 and 0.15. Due to micro-inertia effect, the void growth is delayed in the dynamic analysis. For higher loading rate, the porosity evolves earlier. Nevertheless, the stress level necessary to trigger the expansion is larger. For larger strain rate senstivity, the void growth is delayed.

Most of the investigations are accounting for porous material containing spherical voids. But recently Sartori et al. [36, 34] considered spheroidal RVE with prolate and oblate voids (see Fig. 2.14). The authors used the Gologanu et al. [14] model to capture the static reponse of the porous material. The trial velocity field of Gologanu et al. [14] was used to derive the dynamic

stress tensor which appeared to be scaled by the matrix mass density and two internal lengths parameters related to the size of the void (semi axes of the spheroids). Indeed, for this type of geometry, the shape is charaterized by two length parameters, whereas for spherical voids, the shape is defined solely by the radius.

Few studies of the literature are dedicated to cylindrical voids under dynamic loading. One can cite Leblond and Roy [20] for the growth stage and Molinari et al. [25] for the coalescence stage.

2.3.2.4 Leblond and Roy Model

Leblond and Roy [20] proposed a simplified model for dynamic ductile behavior of porous materials containing cylindrical pores. For the investigation, Leblond and Roy [20] considered a cylindrical unit cell (RVE similar to Fig. 2.8) of internal radius a, external radius b. The

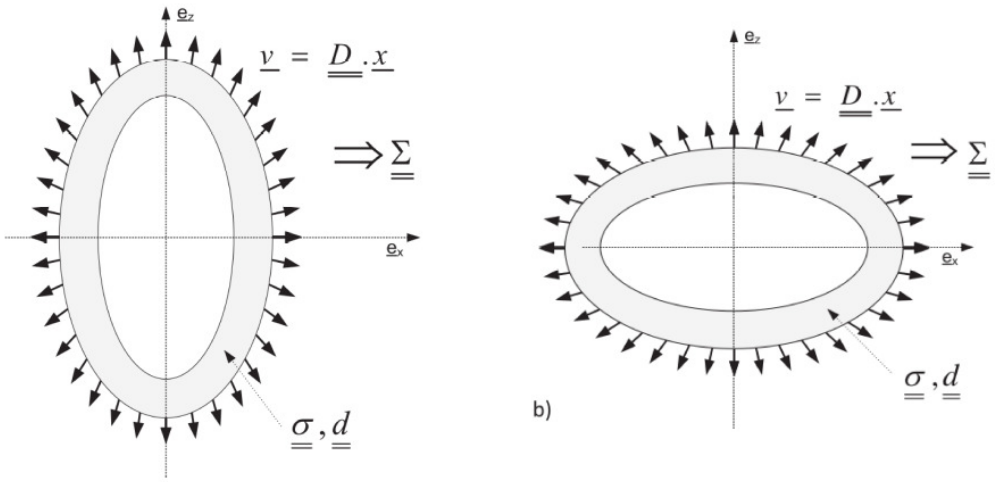

(a) prolate (b) oblate

Figure 2.14: Prolate (a) and oblate (b) spheroidal void embedded inside a confocal spheroid. Homogenous kinematic boundary conditions are applied on the external boundary of the unit cell, Sartori et al. [36, 34]. The RVE is similar to the Gologanu et al. [13] work.

length of the RVE is l. The porosity is defined as:

$$f = \frac{a^2}{b^2} \tag{2.37}$$

The unit cell is loaded under axisymmetric generalized plane strain and shearing is neglected. The matrix behavior is viscoplastic. The flow stress is linked to the effective strain rate via a powerlaw, $\sigma_{eq} = \sigma_0(d_{eq}/\dot{\varepsilon}_0)^n$. From the J2 flow rule:

$$\frac{\mathbf{d}}{\dot{\varepsilon}_0} = \frac{3}{2}\left(\frac{\sigma_{eq}}{\sigma_0}\right)^{n-1}\frac{\boldsymbol{\sigma}^{'}}{\sigma_0} \tag{2.38}$$

where, $\mathbf{d}$ represents the strain rate tensor, $\boldsymbol{\sigma}^{'}$ represents the deviatoric part of the stress tensor ($\boldsymbol{\sigma}$), σ_{eq} represents the equivalent stress (von Mises) and $\dot{\varepsilon}_0$, σ_0, n are material constants. The velocity field in the cylindrical coordinate system is:

$$v_r = \frac{A}{r} - \frac{Br}{2}, v_z = Bz \tag{2.39}$$

where, $A = \frac{3}{2}b^2 D_m$, $B = D_{33}$, $D_m = tr(\mathbf{D})/3$. Note that under axisymmetric loading $D_{11} = D_{22}$. The authors assume that the acceleration in the axial direction is negligible, $\gamma_z \approx 0$. Using the flow rule and equation of motion, the components of macroscopic stress in the plane direction are:

$$\frac{\Sigma_{11}}{\sigma_0} = \frac{\Sigma_{22}}{\sigma_0} = \frac{1}{2\sqrt{3}}\frac{n}{n+1}\left(\frac{|D_{33}|}{\dot{\varepsilon}_0}\right)^{1/n}[I(X) + XI^{'}(X)] + \tau^2 Q^c(\ddot{f}, \dot{f}, f) \tag{2.40}$$

The component of the macrostress in the axial direction is:

$$\frac{\Sigma_{33}-\Sigma_{11}}{\sigma_0}=\frac{1}{n+1}sgn(D_{33})\left(\frac{|D_{33}|}{\dot{\varepsilon}_0}\right)^{1/n}X[I(X)-nXI^{'}(X)] \tag{2.41}$$

$$\text{where, } X=\frac{\sqrt{3}}{2}\frac{D_m}{|D_{33}|},\ I(X)=\int_{2X}^{2X/f}2(1+x^2)^{(n+1)/2n}dx/x^2 \tag{2.42}$$

Note that the micro-inertia contribution is represented by the term $\tau^2 Q^c$:

$$\tau^2 Q^c(\ddot{f},\dot{f},f)=\frac{\rho a_0^2}{4\sigma_0 f_0}\left[\ln\left(\frac{1}{f}\right)\ddot{f}-\frac{\dot{f}^2}{2f}\right] \tag{2.43}$$

where a_0, f_0 denote the initial void radius and the initial porosity. From Eq (2.40), it is clear that once the term $\tau^2 Q^c(\ddot{f},\dot{f},f)$ is neglected, the quasi static approach of Leblond et al. [19] is retrieved. With the assumption of neglecting the axial acceleration, the dynamic stress is spherical. This contribution is scaled by the square of radius of the void cross-section but the effect of the void length is not accounted for in the model.

2.3.2.5 Molinari et. al Model

Molinari et. al [25] investigated the dynamic behavior of porous material with cylindrical void in the coalescence stage. The dynamic homogenization procedure for the porous viscoplastic material used here is similar to the one proposed by Molinari and Mercier [26] (see section 2.3.2.3). Here the representative volume element is considered as a cylindrical unit cell embedding a coaxial cylindrical void, see Fig. 2.15. The dimensions 2H and 2L represent the height and diameter of the cylindrical unit cell while 2h and 2R are the height and diameter

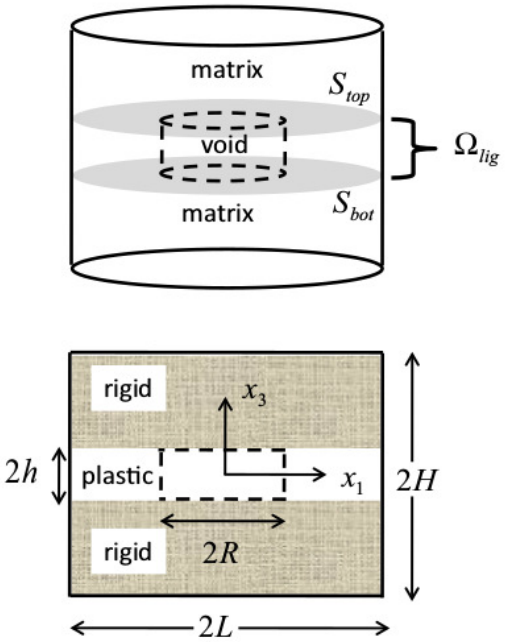

Figure 2.15: Representative volume element adopted for the coalescence analysis. The RVE has a cylindrical shape (height, $2H$ and diameter, $2L$) with a cylindrical void (height, $2h$ and diameter, $2R$) inside, Molinari et al. [25]

of the cylindrical void inside the unit cell. The cell is divided into a central part (Ω_{lig}), shown in Fig. 2.15 complemented by two plates on the top and bottom of Ω_{lig}. During coalescence, both top and bottom plates of the RVE remain rigid. In addition, it is assumed that the only non vanishing macroscopic strain rate is D_{33} so that $D_{11} = D_{22} = 0$. The authors proposed an explicit relation for the dynamic stress:

$$\Sigma_{33}^{dyn} = \rho\frac{\dot{D}_{33}}{2c}\left[L^2\ln\left(\frac{L}{R}\right) - \frac{3}{4}L^2 - \frac{R^4}{(4L)^2} + R^2\right] - \rho\frac{D_{33}^2}{c^2}\left[\left(\frac{1}{4} - \frac{c}{2}\right)L^2\ln\left(\frac{L}{R}\right) + \left(\frac{-9}{16} + \frac{3}{8}c\right)L^2 + \left(\frac{-3}{16} + \frac{c}{8}\right)\frac{R^4}{L^2} + \left(\frac{5}{8} - \frac{c}{2}\right)R^2 + \frac{1}{8}\frac{L^4}{R^2}\right] + \frac{\rho h^2}{3c}(\dot{D}_{33} + D_{33}^2)\left(1 - \frac{R^2}{L^2}\right) \quad (2.44)$$

where, $c = h/H$ is a dimensionless parameter. The macroscopic stress components in the plane direction, Σ_{11}^{dyn} and Σ_{22}^{dyn} are undefined because the condition $D_{11} = 0$ and $D_{22} = 0$ was adopted for the coalescence stage analysis. The authors pointed out that for high loading rates,

micro-inertia influences strongly the macroscopic stress in the axial direction Σ_{33}. Based on this approach, the effect of length of the void in the inertia contribution is present and is playing an important role in the dynamic problem.

2.3.3 Conclusion

To conclude from the literature review, it is evident that void shape/void geometry is an important parameter which influences the behavior of ductile porous solids for quasi-static conditions but also in dynamic conditions. At this stage, most of the works dedicated to micro-inertia effects have been done considering a spherical shape for the voids (Carroll and Holt [5], Rice and Tracey [32], Ortiz and Molinari [30], Wang [46, 47], Molinari and Mercier [26], Czarnota et al. [9],...). Recently Sartori et al. [34, 36] accounted for void shape effects on the dynamic response, the representative volume element being spheroidal. Indeed, for this type of geometry, the shape is characterized by two length parameters whereas for spherical voids, the shape is defined solely by the radius. Cylindrical voids are also defined by two length parameters, the radius and the length of the void which are expected to play a role in the dynamic response. Few authors investigated the dynamic behavior of porous material with cylindrical voids. The work of Molinari et al. [25], focused on the coalescence stage in presence of micro-inertia. The analysis by Molinari et al. [25] has shown that the length is influencing the axial dynamic stress and is modulating the coalescence stage. The cylindrical void in a finite matrix under dynamic loading has also been considered by Leblond and Roy [20]. Nevertheless, it is to be noted that in the work of Leblond and Roy [20], the component of the acceleration field in the axial direction was neglected, so that the dynamic stress remains unaffected by the length of the cylinder. Therefore, the modeling suffers from restituting the influence of the second internal length which is the length of the void. So our goal is to define a new model for the dynamic

growth of cylindrical voids in a porous material which accounts for both length scales: the size and the length of the voids, under general loading conditions.

To reveal the influence of micro-inertia, the theory is developed for general kinematic boundary conditions. However one has to keep in mind that the velocity field adopted here supposes that the section of the void keeps a circular shape. The dynamic homogenization theory proposed by Molinari and Mercier [26] is used here. So the macroscopic stress have two contributions: static part (micro-inertia independent) and dynamic part (micro-inertia dependent). The Gurson [15] model for cylindrical voids is adopted for the quasi-static part. For dynamic part, the explicit relationship proposed by Molinari and Mercier [26] is adopted with the approximate velocity inherited from Gurson [15] for cylindrical shells. The results are shown for rigid perfectly plastic matrix under axisymmetric loading. The analytical modeling is validated with finite element simulations for different boundary conditions. The next chapter presents the analytical modeling for the porous material containing cylindrical voids under dynamic loading.

Chapter 3

Modeling

In this chapter, the analytical modeling developed for the dynamic response of porous materials containing cylindrical voids is presented. Our approach is founded on the dynamic homogenization scheme proposed by Molinari and Mercier [26] which is recalled in chapter 1, section 2.3.2.3. Within this framework, the macroscopic stress tensor is found to be the sum of a quasi-static part and a dynamic part which contains micro-inertia effect, see Eqs (2.31), (2.32). The Representative Volume Element consisting of a cylindrical shell and the admissible velocity field adopted for our model are presented in the first section of this chapter. In the second and third sections, explicit relationship are given for the dynamic part and the quasi-static one, respectively.

3.1 Geometry of the RVE and formulation of the velocity field

The representative volume element (RVE) of the porous material corresponds to a hollow cylinder (circular cross section) of current internal radius a, external radius b, length $2l$, see Fig. 3.1. The current porosity is defined as:

$$f = \frac{a^2}{b^2} \tag{3.1}$$

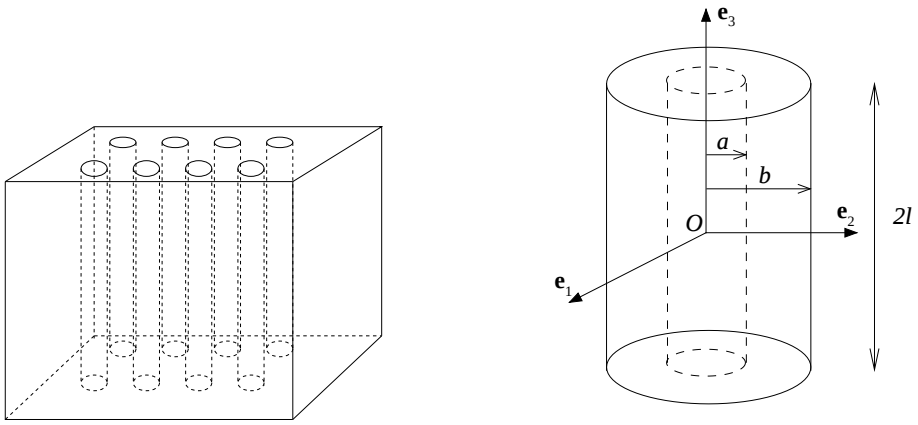

Figure 3.1: Schematic representation of the porous material. A cylindrical unit cell (length $2l$, void radius a, external radius b) is taken as the representative volume element. A cartesian coordinate system is adopted for the derivation of the model with $-l < x_3 < l$.

The rate of change of volume fraction is obtained from Eq (3.1) as:

$$\dot{f} = 2f\left(\frac{\dot{a}}{a} - \frac{\dot{b}}{b}\right) \tag{3.2}$$

The volume of the RVE is $V = 2\pi b^2 l$ see Fig. 3.1. The rate of volume change is obtained as:

$$\dot{V} = 4\pi l b\dot{b} + 2\pi b^2 \dot{l} \tag{3.3}$$

The volumetric part of the macroscopic strain rate tensor, D_m is defined as:

$$D_m = \frac{\dot{V}}{3V} = \frac{1}{3}\left(\frac{2\dot{b}}{b} + \frac{\dot{l}}{l}\right) \tag{3.4}$$

As $\dot{D}_{33} = \frac{\dot{l}}{l}$ and since $D_m = \frac{\mathrm{tr}\mathbf{D}}{3}$, one clearly sees from Eq. (3.4), that :

$$\frac{\dot{b}}{b} = \frac{D_{11} + D_{22}}{2}. \tag{3.5}$$

Obviously, this relation is valid when the RVE does not deviate too much from its initial cylindrical shape so that its volume can still be approximated by $V = 2\pi b^2 l$. This relation is in fact an approximate relation and is fully consistent when the circular shape of the cross-section is preserved. Indeed, when D_{11} and D_{22} differ, the circular shape will not pertain during the deformation process. This is satisfied at least for axi-symmetric loadings. The matrix is incompressible and the volume of matrix material $V_m = 2\pi l(b^2 - a^2)$ is not evolving. Therefore, from $\dot{V}_m$=0, one gets:

$$\frac{\dot{l}}{l} = -2\left(\frac{b\dot{b} - a\dot{a}}{b^2 - a^2}\right) \tag{3.6}$$

After some manipulations, Eq (3.6) can be written differently:

$$D_{33} + \frac{D_{11} + D_{22}}{(1-f)} = 2\frac{\dot{a}}{a}\left(\frac{1}{f^{-1} - 1}\right) \tag{3.7}$$

For the case of axi-symmetric loading, $D_{11} = D_{22}$ and Eq (3.7) becomes:

$$D_{33} + \frac{2D_{11}}{(1-f)} = 2\frac{\dot{a}}{a}\left(\frac{1}{f^{-1} - 1}\right) \tag{3.8}$$

As the matrix surrounding the cylindrical cavity is assumed incompressible and elasticity being neglected, from Eqs (3.2), (3.4) and (3.6) the evolution law for the porosity, $\dot{f} = (1-f)\mathrm{tr}\mathbf{D}$ (see Eq 2.17) is retrieved.

An approximate velocity, denoted by $\mathbf{v}$ has to be defined, satisfying the incompressibility condition and the kinematic condition at the boundary ∂V of the RVE:

$$\boldsymbol{v} = \mathbf{D} \cdot \boldsymbol{x} \quad \text{on } \partial V\,, \tag{3.9}$$

The cylinder is loaded under general strain rate condition with $\mathbf{D}$ written in the orthonormal frame basis $(\mathbf{e}_1, \mathbf{e}_2, \mathbf{e}_3)$ as:

$$\mathbf{D} = \begin{bmatrix} D_{11} & D_{12} & D_{13} \\ D_{12} & D_{22} & D_{23} \\ D_{13} & D_{23} & D_{33} \end{bmatrix} . \tag{3.10}$$

Based on the analysis of Gurson [15] and assuming uniform shear components of the strain rate tensor within the matrix material (see also Torki et al. [40, 41]), the admissible velocity field of the following form is adopted:

$$\boldsymbol{v} = \left(\mathbf{D}^{\mathrm{d}} + \mathbf{D}^{\mathrm{s}} + \mathbf{D}^{\mathrm{u}}\right) \cdot \boldsymbol{x} \tag{3.11}$$

where $\mathbf{D}^{\mathrm{s}}$ and $\mathbf{D}^{\mathrm{u}}$ are traceless tensors (inducing no dilatation); $\mathbf{D}^{\mathrm{s}}$ represents the change of shape of the void (including evolution of the cross section) whereas $\mathbf{D}^{\mathrm{u}}$ is describing the stretching or elongation of the void preserving the shape of the cross section (assumed circular) at constant porosity. Both are uniform and only depending on the macroscopic strain rate tensor components:

$$\mathbf{D}^{\mathrm{s}} = \begin{bmatrix} \frac{D_{11}-D_{22}}{2} & D_{12} & D_{13} \\ D_{12} & \frac{D_{22}-D_{11}}{2} & D_{23} \\ D_{13} & D_{23} & 0 \end{bmatrix} , \tag{3.12}$$

and

$$\mathbf{D}^{\mathrm{u}} = \begin{bmatrix} \frac{-D_{33}}{2} & 0 & 0 \\ 0 & \frac{-D_{33}}{2} & 0 \\ 0 & 0 & D_{33} \end{bmatrix} . \tag{3.13}$$

The last contribution to the approximate velocity field of Eq (3.11) expressed as:

$$\mathbf{D}^{\mathrm{d}} = \begin{bmatrix} \frac{\mathrm{tr}(\mathbf{D})}{2}\left(\frac{b}{r}\right)^2 & 0 & 0 \\ 0 & \frac{\mathrm{tr}(\mathbf{D})}{2}\left(\frac{b}{r}\right)^2 & 0 \\ 0 & 0 & 0 \end{bmatrix} \tag{3.14}$$

is inducing porosity evolution, since $tr\mathbf{D}^d \neq 0$. Note that the trial velocity field given by Eqs (3.11-3.14) supposes that the shape of voids remains cylindrical with a circular cross section. Therefore, the tensor $\mathbf{D}^{\mathrm{s}}$, related to the shape change, has to be overwhelmed by the other contributions in our applications. Let us remark that various trial velocity fields found in the literature for the dynamic response of porous materials fall within the formulation adopted here. For instance, the velocity field used in Leblond and Roy [20] is retrieved for $\mathbf{D}^{\mathrm{s}} = \mathbf{0}$. This is also the case for the velocity field adopted in Molinari et al. [25] for the description of the coalescence stage.

From Eqs (3.11-3.14), the trial velocity can also be put in the form of Eq (2.9):

$$\boldsymbol{v} = \hat{\mathbf{D}} \cdot \boldsymbol{x} + B\tilde{\boldsymbol{x}} \tag{3.15}$$

where $\hat{\mathbf{D}}$ is a strain rate tensor expressed in the frame basis $(\mathbf{e}_1, \mathbf{e}_2, \mathbf{e}_3)$, see Eq (2.10) and $B = \frac{tr\mathbf{D}}{2}(\frac{b}{r})^2 - \frac{D_{33}}{2}$. $\tilde{\boldsymbol{x}} = x_1\mathbf{e}_1 + x_2\mathbf{e}_2$ represents the projection in the plane $(\mathbf{e}_1, \mathbf{e}_2)$, along $\mathbf{e}_3$ of the position vector $\boldsymbol{x}$ defined in chapter 1, section 2.3.2.3. This expressions are recalled here to make the reading easier. The derivative of Eq (3.15) based on Gurson [15] is presented next in section 3.1.1.

3.1.1 Formulation of the admissible velocity field

In this section, we detail how the approximate velocity field was proposed by Gurson [15]. We will use it to evaluate the dynamic response of porous material containing cylindrical voids.

In the analysis of Gurson [15], the general form of the velocity fields in the cylindrical coordinates is defined as:

$$\boldsymbol{v} = v_r \mathbf{e_r} + v_\theta \mathbf{e}_\theta + v_z \mathbf{e_z} \tag{3.16}$$

Gurson [15] proposes the following expression for the three components:

$$v_r = \left(c_1 r^3 + c_2 r + \frac{c_3}{r} + \frac{c_4}{r^3}\right)\cos 2\theta + \frac{c_7}{r} + c_9 r \sin 2\theta - c_8 \frac{r}{2} + c_9 r \sin 2\theta + c_{10} z \sin\theta + c_{11} z \cos\theta \tag{3.17}$$

$$v_\theta = (-2c_1 r^3 - c_2 r + c_4 r^{-3})\sin 2\theta + c_9 r \cos 2\theta + c_{10} z \sin\theta - c_{11} z \cos\theta \tag{3.18}$$

$$v_z = c_{10} r \sin\theta + c_{11} r \cos\theta + c_8 z \tag{3.19}$$

where c_i are constants to be defined according to boundary conditions. Note that the velocity field defined by Eqs (3.17), (3.18), (3.19) fulfills the incompressibility condition ($div(\boldsymbol{v}) = 0$). At the boundary ∂V of the RVE, since the kinematic condition Eq (3.9) prevails with $\mathbf{D}$ given by Eq (3.10), the velocity components are written as:

$$v_1 = D_{11} x_1 + D_{12} x_2 + D_{13} x_3 \tag{3.20}$$

$$v_2 = D_{12} x_1 + D_{22} x_2 + D_{23} x_3 \tag{3.21}$$

$$v_3 = D_{13}x_1 + D_{23}x_2 + D_{33}x_3 \tag{3.22}$$

The prescribed boundary conditions Eq (3.9) can be expressed in cylindrical coordinate system (at $r = b$):

$$v_r(b) = \left(\frac{D_{11} - D_{22}}{2}\right) b\cos 2\theta + \left(\frac{D_{11} + D_{22}}{2}\right) b + D_{12}b\sin 2\theta + (D_{23}\sin\theta + D_{13}\cos\theta)z \tag{3.23}$$

$$v_\theta(b) = D_{12}b\cos 2\theta + \left(\frac{D_{22} - D_{11}}{2}\right) b\sin 2\theta + (D_{23}\sin\theta - D_{13}\cos\theta)z \tag{3.24}$$

$$v_z(b) = D_{13}b\cos\theta + D_{23}b\sin\theta + D_{33}z \tag{3.25}$$

By comparing Eqs (3.17-3.19, 3.23-3.25), conditions for the unknowns are obtained:

$$\begin{aligned}\left(\frac{D_{11} - D_{22}}{2}\right) b\cos 2\theta + \left(\frac{D_{11} + D_{22}}{2}\right) b + D_{12}b\sin 2\theta + (D_{23}\sin\theta + D_{13}\cos\theta)z \\ = \left(c_1 b^3 + c_2 b + \frac{c_3}{b} + \frac{c_4}{b^3}\right)\cos 2\theta + \frac{c_7}{b} \\ + c_9 b\sin 2\theta - c_8\frac{b}{2} + (c_{10}\sin\theta + c_{11}\cos\theta)z\end{aligned} \tag{3.26}$$

$$\begin{aligned}D_{12}b\cos 2\theta + \left(\frac{D_{22} - D_{11}}{2}\right) b\sin 2\theta + (D_{23}\sin\theta - D_{13}\cos\theta)z \\ = (-2c_1 b^3 - c_2 b + c_4 b^{-3})\sin 2\theta + c_9 b\cos 2\theta + (c_{10}\cos\theta - c_{11}\sin\theta)z\end{aligned} \tag{3.27}$$

$$D_{13}b\cos\theta + D_{23}b\sin\theta + D_{33}z = c_{10}b\sin\theta + c_{11}b\sin\theta + c_8 z \tag{3.28}$$

As the functions 1, $\sin(\theta)$, $\cos(\theta)$, $\sin(2\theta)$, $\cos(2\theta)$ are orthogonal, unknowns c_7, c_8, c_9, c_{10}, c_{11} are identified. Unknowns: $c_9 = D_{12}$, $c_7 = \left(\frac{tr\mathbf{D}}{2}\right) b^2$, $c_{10} = D_{23}$, $c_{11} = D_{13}$ and $c_8 = D_{33}$. From Gurson [15], $c_1 = 0$ since when the porosity is small, the velocity field should be linear in r for $r >> a$. In addition it is supposed, as in Gurson [15] that c_3 and c_4 are set to zero. Therefore, $c_2 = \frac{D_{11}-D_{22}}{2}$. As a consequence in general loading conditions, the velocity field is defined as in Gurson [15]:

$$\begin{aligned}\boldsymbol{v} = &\left\{\left(\frac{D_{11}-D_{22}}{2}\right) r\cos 2\theta + D_{12} r \sin 2\theta - D_{33}\frac{r}{2} + \left(\frac{tr\mathbf{D}}{2}\right)\frac{b^2}{r} + D_{23} z sin\theta + D_{13} z cos\theta\right\}\mathbf{e_r} \\ &+ \left\{D_{12} r\cos 2\theta + \left(\frac{D_{22}-D_{11}}{2}\right) r\sin 2\theta + D_{23} z cos\theta - D_{13} z sin\theta\right\}\mathbf{e}_\theta \\ &+ \left\{D_{13} r cos\theta + D_{23} r sin\theta + D_{33} z\right\}\mathbf{e_z}. \quad (3.29)\end{aligned}$$

which in the cartesian coordinate system becomes:

$$\begin{aligned}\boldsymbol{v} = &\left(\frac{D_{11}-D_{22}}{2}\right) x_1\mathbf{e_1} + D_{12} x_2\mathbf{e_1} + D_{13} x_3\mathbf{e_1} \\ &+ D_{12} x_1\mathbf{e_2} + \left(\frac{D_{22}-D_{11}}{2}\right) x_2\mathbf{e_2} + D_{23} x_3\mathbf{e_2} \\ &+ D_{13} x_1\mathbf{e_3} + D_{23} x_2\mathbf{e_3} + D_{33} x_3\mathbf{e_3} \\ &+ \left(\frac{tr\mathbf{D}}{2}\left(\frac{b}{r}\right)^2 - \frac{D_{33}}{2}\right)(x_1\mathbf{e_1} + x_2\mathbf{e_2}). \quad (3.30)\end{aligned}$$

or in a condensed form:

$$\boldsymbol{v} = \hat{\mathbf{D}}\cdot\boldsymbol{x} + \left(\frac{tr\mathbf{D}}{2}\left(\frac{b}{r}\right)^2 - \frac{\mathbf{D}_{33}}{2}\right)\tilde{\boldsymbol{x}} \quad (3.31)$$

So Eq (3.15) is retrieved. In our work, when the more general boundary condition $\boldsymbol{v} = \mathbf{L}.\boldsymbol{x}$ is

considered, the trial velocity field will be of the form:

$$\boldsymbol{v} = \hat{\mathbf{L}} \cdot \boldsymbol{x} + \left(\frac{tr\mathbf{L}}{2} \left(\frac{b}{r} \right)^2 - \frac{L_{33}}{2} \right) \tilde{\boldsymbol{x}} \tag{3.32}$$

Eq (3.31) or Eq (3.32) will be used to calculate the components of the dynamic stress tensor $\boldsymbol{\Sigma}^{\text{dyn}}$, see Appendix A for more details.

3.2 Formulation of the micro-inertia dependent term $\boldsymbol{\Sigma}^{\text{dyn}}$

To evaluate $\boldsymbol{\Sigma}^{\text{dyn}}$, we determine explicitly the integral term proposed by Molinari and Mercier [26], $1/|V| \int_V \rho \boldsymbol{\gamma} \cdot \delta \mathbf{v} dV$ (see chapter-1, section 2.3.2.3, Eqs (2.32), (2.33)) with use of the boundary condition $\boldsymbol{v} = \mathbf{L} \cdot \boldsymbol{x}$ (where $\mathbf{L}$ represents the macroscopic velocity gradient) instead of Eq (3.31). Indeed it can be easily shown that $1/|V| \int_V \rho \boldsymbol{\gamma} \cdot \delta \mathbf{v} dV = \Sigma^{dyn} : \delta^t L$. Within this context, the antisymmetric part of the dynamic stress tensor is also defined. From the general case of Appendix A, the restrition to the boundary condition defined by Eq (2.26) is straight forward by simply considering that $\mathbf{L}$ is symmetric or $\mathbf{L} = \mathbf{D}$. In that case, the components of the dynamic stress tensor are:

$$\begin{aligned} \Sigma_{11}^{\text{dyn}} = \frac{\rho a^2}{4} \Bigg[& \left(f^{-1} - f \right) \left(\dot{\hat{D}}_{11} + \hat{C}_{11} - D_{33} \hat{D}_{11} \right) - \frac{9}{2} \left(f^{-2} - f^{-1} \right) D_{\text{m}}^2 \\ & + 3 f^{-1} \ln \left(\frac{1}{f} \right) \left(\dot{D}_{\text{m}} + 3 D_{\text{m}}^2 - D_{\text{m}} D_{33} \right) \\ & + \left(f^{-1} - 1 \right) \left(\frac{D_{33}^2}{2} - \dot{D}_{33} + C_{11} + C_{22} + 6 D_{\text{m}} \hat{D}_{11} \right) \Bigg] \end{aligned} \tag{3.33}$$

$$\Sigma_{22}^{\text{dyn}} = \frac{\rho a^2}{4}\Bigg[\left(f^{-1}-f\right)\left(\dot{\hat{D}}_{22}+\hat{C}_{22}-D_{33}\hat{D}_{22}\right) - \frac{9}{2}\left(f^{-2}-f^{-1}\right)D_{\text{m}}^2 + 3f^{-1}\ln\left(\frac{1}{f}\right)\left(\dot{D}_{\text{m}}+3D_{\text{m}}^2-D_{\text{m}}D_{33}\right) + \left(f^{-1}-1\right)\left(\frac{D_{33}^2}{2}-\dot{D}_{33}+C_{11}+C_{22}+6D_{\text{m}}\hat{D}_{22}\right)\Bigg] \quad (3.34)$$

$$\Sigma_{33}^{\text{dyn}} = \frac{\rho a^2}{4}\Bigg[\left(f^{-1}-f\right)\left(\frac{\dot{D}_{33}}{2}-\frac{D_{33}^2}{4}-\frac{C_{11}+C_{22}}{2}\right) - \frac{9}{2}\left(f^{-2}-f^{-1}\right)D_{\text{m}}^2 + \left(f^{-1}-1\right)\left(C_{11}+C_{22}+3D_{\text{m}}D_{33}+\frac{D_{33}^2}{2}-9D_{\text{m}}^2-\dot{D}_{33}-3\dot{D}_{\text{m}}\right) + 3f^{-1}\ln\left(\frac{1}{f}\right)\left(\dot{D}_{\text{m}}+\frac{9}{2}D_{\text{m}}^2-D_{\text{m}}D_{33}\right)\Bigg] + \frac{\rho l^2}{3}\left(1-f\right)\left(\dot{D}_{33}+C_{33}\right) \quad (3.35)$$

$$\Sigma_{12}^{\text{dyn}} = \Sigma_{21}^{\text{dyn}} = \frac{\rho a^2}{4}\left[\left(f^{-1}-f\right)\left(\dot{D}_{12}+C_{12}-D_{33}D_{12}\right)+6\left(f^{-1}-1\right)D_{\text{m}}D_{12}\right] \quad (3.36)$$

$$\Sigma_{13}^{\text{dyn}} = \frac{\rho l^2}{3}\left[\left(1-f\right)\left(\dot{D}_{13}+C_{13}-\frac{D_{33}}{2}D_{13}\right)+\frac{3}{2}\ln\left(\frac{1}{f}\right)D_{\text{m}}D_{13}\right] \quad (3.37)$$

$$\Sigma_{23}^{\text{dyn}} = \frac{\rho l^2}{3}\left[\left(1-f\right)\left(\dot{D}_{23}+C_{23}-\frac{D_{33}}{2}D_{23}\right)+\frac{3}{2}\ln\left(\frac{1}{f}\right)D_{\text{m}}D_{23}\right] \quad (3.38)$$

$$\Sigma_{31}^{\text{dyn}} = \frac{\rho a^2}{4}\left[\left(f^{-1}-f\right)\left(\dot{D}_{13}+C_{13}-\frac{D_{33}}{2}D_{13}\right)+3\left(f^{-1}-1\right)D_{\text{m}}D_{13}\right] \quad (3.39)$$

$$\Sigma_{32}^{\text{dyn}} = \frac{\rho a^2}{4}\left[\left(f^{-1}-f\right)\left(\dot{D}_{23}+C_{23}-\frac{D_{33}}{2}D_{23}\right)+3\left(f^{-1}-1\right)D_{\text{m}}D_{23}\right] \quad (3.40)$$

where $\mathbf{C}=\hat{\mathbf{D}}\cdot\hat{\mathbf{D}}$.

The expression of the dynamic stress tensor reveals particular aspects that are further commented. The influence of quadratic and time derivative terms involving strain rate tensor components are also present for the RVE consisting of a hollow cylinder. This illustrates the specific rate dependencies brought by the micro-inertia to the overall response of porous materials. This has already been observed for spherical voids (Molinari and Mercier [26]) and spheroidal voids (Sartori et al. [36]).

As revealed for other geometries, the dynamic response is closely related to the cell size. Here, for cylindrical voids, it appears from Eqs (3.33-3.40) that the dynamic stress tensor is scaled, by the mass matrix density ρ and is involving the square of two characteristic lengths of the unit cell: the void radius a and half the void length l.

The macroscopic stress tensor $\boldsymbol{\Sigma}$ is the sum of the static and the dynamic contributions, with $\boldsymbol{\Sigma}^{\text{static}}$ being a symmetric tensor describing the static response of the porous material. As a consequence, from Eqs (3.37-3.40), the macroscopic stress tensor $\boldsymbol{\Sigma}$ is shown to be nonsymmetric. This reminds the results obtained by Molinari and Mercier [26] for porous materials containing spherical voids, where the loss of symmetry was only due to spin effects. Here, however, even when spin effects vanish (i.e. $\boldsymbol{\Omega}=\mathbf{0}$ is imposed), owing to the anisotropy of the cell geometry, the macroscopic stress tensor may remain non symmetric. In the following sections, we derive the macroscopic dynamic stress tensor for plane strain case and for uniaxial deformation case. Shear contributions are also disregarded.

3.2.1 Plane strain case

Under plane strain $D_{33} = 0$ without shear components ($D_{12} = D_{13} = D_{23} = 0$), the dynamic macroscopic stress tensor Eqs (3.33-3.35) reduces to:

$$\Sigma_{11}^{\text{dyn}} = \frac{\rho a^2}{4}\Bigg[\left(f^{-1} - f\right)\left(\dot{\hat{D}}_{11} + \dot{\hat{C}}_{11}\right) - \frac{9}{2}\left(f^{-2} - f^{-1}\right) {D_{\text{m}}}^2 + 3f^{-1}\ln\left(\frac{1}{f}\right)\left(\dot{D}_{\text{m}} + 3{D_{\text{m}}}^2\right) + \left(f^{-1} - 1\right)\left(C_{11} + C_{22} + 6D_{\text{m}}\hat{D}_{11}\right)\Bigg] \tag{3.41}$$

$$\Sigma_{22}^{\text{dyn}} = \frac{\rho a^2}{4}\Bigg[\left(f^{-1} - f\right)\left(\dot{\hat{D}}_{22} + \dot{\hat{C}}_{22}\right) - \frac{9}{2}\left(f^{-2} - f^{-1}\right) {D_{\text{m}}}^2 + 3f^{-1}\ln\left(\frac{1}{f}\right)\left(\dot{D}_{\text{m}} + 3{D_{\text{m}}}^2\right) + \left(f^{-1} - 1\right)\left(C_{11} + C_{22} + 6D_{\text{m}}\hat{D}_{22}\right)\Bigg] \tag{3.42}$$

$$\Sigma_{33}^{\text{dyn}} = \frac{\rho a^2}{4}\Bigg[\left(f^{-1} - f\right)\left(\frac{C_{11} + C_{22}}{2}\right) - \frac{9}{2}\left(f^{-2} - f^{-1}\right) D_{\text{m}}^2 + \left(f^{-1} - 1\right)\left(C_{11} + C_{22} - 9D_{\text{m}}^2 - 3\dot{D}_{\text{m}}\right) + 3f^{-1}\ln\left(\frac{1}{f}\right)\left(\dot{D}_{\text{m}} + \frac{9}{2}D_{\text{m}}^2\right)\Bigg] \tag{3.43}$$

3.2.2 Uniaxial deformation

When $D_{33} \neq 0$ and all other components being zero, Eqs.(3.33-3.35) reduce to:

$$\Sigma_{11}^{dyn} = \Sigma_{22}^{dyn} = \rho a^2 \left[\left(\frac{1}{4} f^{-1} ln\left(\frac{1}{f}\right) - \frac{1}{4}(f^{-1} - 1) \right) \dot{D}_{33} + \left(\frac{1}{8}(f^{-1} - 1) - \frac{1}{8}(f^{-2} - f^{-1}) \right) D_{33}^2 \right] \quad (3.44)$$

$$\Sigma_{33}^{dyn} = \rho l^2 \left[\frac{(1-f)}{3} (\dot{D}_{33} + D_{33}^2) \right] + \rho a^2 \left[\left(\frac{1}{4} f^{-1} ln\left(\frac{1}{f}\right) - \frac{3}{8}(f^{-1} + f) + \frac{1}{2} \right) \dot{D}_{33} + \left(\frac{1}{8} f^{-1} ln\left(\frac{1}{f}\right) + \frac{3}{16}(f^{-1} + f) - \frac{1}{8}(f^{-2} + 1) \right) D_{33}^2 \right] \quad (3.45)$$

It is observed that Eq (3.45) is coinciding with the one proposed by Molinari et al. [25] for the dynamic coalescence, when $h = H = l$, $R = a$ and $L = b$ in Eq (2.44), (compare Fig. 2.15 and Fig. 3.1).

3.3 Quasistatic stress tensor $\boldsymbol{\Sigma}^{\text{static}}$

The quasi-static stress depicts the response of porous materials under static loading, when micro-inertia effects are neglected. The matrix material is rigid perfectly plastic, with σ_0 being the yield stress. The quasi-static stress tensor $\boldsymbol{\Sigma}^{\text{static}}$ is derived here from the yield function Eq (2.11) proposed by Gurson [15] for cylindrical voids:

$$\Phi(\boldsymbol{\Sigma}^{\text{static}}, \sigma_0, f) = C_{\text{eqv}} \left(\frac{\Sigma_{\text{eq}}^{\text{static}}}{\sigma_0} \right)^2 + 2f \cosh\left(\frac{\sqrt{3}}{2} \frac{\Sigma_{\gamma\gamma}^{\text{static}}}{\sigma_0} \right) - (1 + f^2) = 0 \quad (3.46)$$

where C_{eqv} is a function of f whose expression is depending on the loading state and boundary conditions, see Gurson [15] for details. $\Sigma^{\text{static}}_{\gamma\gamma}$ is the macroscopic transverse stress defined by:

$$\Sigma^{\text{static}}_{\gamma\gamma} = \Sigma^{\text{static}}_{11} + \Sigma^{\text{static}}_{22} \tag{3.47}$$

and $\Sigma^{\text{static}}_{\text{eq}}$ is the macroscopic equivalent stress expressed as:

$$\Sigma^{\text{static}}_{\text{eq}} = \sqrt{\frac{3}{2}\boldsymbol{\Sigma}^{\text{static}\prime} : \boldsymbol{\Sigma}^{\text{static}\prime}}\,, \tag{3.48}$$

The quasistatic stress $\boldsymbol{\Sigma}^{\text{static}}$ and the macroscopic plastic strain rate $\mathbf{D}$ are related by the flow law:

$$\mathbf{D} = \dot{\kappa}\frac{\partial\Phi(\boldsymbol{\Sigma}^{\text{static}}, \sigma_0, f)}{\partial\boldsymbol{\Sigma}^{\text{static}}}\,, \tag{3.49}$$

where $\dot{\kappa}$ is the plastic multiplier subjected to the Kuhn-Tucker complementary conditions: $\Phi \leq 0$, $\dot{\kappa} \geq 0$, $\Phi\dot{\kappa} = 0$ (Simo and Hughes [37]).

In chapter 4, we restrict our attention to axisymmetric loading conditions that have been selected to reveal important effects brought by the micro-inertia contribution. In that case as reported in Gurson [15], $C_{\text{eqv}} = 1$ in Eq (3.46). Within this context, the static stress is related to the strain rate tensor by explicit relationships, Gurson [15] and Leblond et al. [19]. In the present work, we adopt the one proposed by Sartori et al. [35], see Appendix B.

Chapter 4

Results

4.1 Introduction

In this section, different axisymmetric remote loading conditions will be explored. All the analytical results shown and discussed in this manuscript have been verified against finite element calculations conducted with Abaqus/Explicit. Section 5.1 provides details on the various numerical models developed for the comparative study accompanied by some validation cases. The analytical modeling proposed in this manuscript was developed for general loading conditions. Recall that the velocity field used to derive the dynamic and static stresses assume that the cross section of voids remain circular, so that the contribution $\mathbf{D}^s$ has to be of negligible magnitude, see Eqs (3.11-3.14).

4.2 Axisymmetric loading

For application purpose, we restrict the attention to axisymmetric loading paths without shear contributions. Thus $\mathbf{D}^s$ vanishes. Consequently, $D_{22} = D_{11}$ and the macroscopic stress tensor

$\boldsymbol{\Sigma}$ satisfies $\Sigma_{22} = \Sigma_{11}$, $\Sigma_{ij} = 0$ for all $i \neq j$. The same applies for the static and dynamic contributions, $\boldsymbol{\Sigma}^{\text{static}}$ and $\boldsymbol{\Sigma}^{\text{dyn}}$ respectively.

The dynamic stress tensor for axisymmetric loading still reveals the influence of both a^2 and l^2. Its explicit form, given in Eqs (3.33-3.35) or in appendix A, can be written in the following condensed way:

$$\Sigma_{11}^{\text{dyn}} = \Sigma_{22}^{\text{dyn}} = \rho a^2 F \, , \Sigma_{33}^{\text{dyn}} = \rho a^2 G + \frac{\rho l^2}{3} (1 - f) \left(\dot{D}_{33} + D_{33}^2 \right) \tag{4.1}$$

where functions F and G, see Eqs (A.31-A.32), are depending on the porosity f, quadratic terms in D_{11} and D_{33}, and linear terms implying the time derivatives $\dot{D}_{11}$ and $\dot{D}_{33}$.

Of particular interest, it appears from Eq (4.1) that the influence of l vanishes when one of the following two conditions is fulfilled:

$$l = 0 \tag{4.2}$$

or

$$\dot{D}_{33} + D_{33}^2 = 0 \tag{4.3}$$

which, upon time integration, leads to:

$$D_{33} = \frac{D_{33}^0}{1 + D_{33}^0 t} \tag{4.4}$$

with $D_{33}^0 = D_{33}(t = 0)$. Note that since $v_3 = D_{33} x_3$ (see Eqs 3.15-2.10), Eq (4.3) also corresponds to a nil acceleration in the axial direction, $\gamma_3(x_3, t) = 0$. It is therefore interesting to notice that prescribing a constant axial velocity v_3^0 at $x_3 = l$ (a similar condition but of opposite sign is found for the bottom of the cylinder) induces the fact that Eq (4.3) is satisfied and the

length of the cylinder is no more present in the expressions (4.1). Note that the particular case when D_{33} =0 (plane strain) fulfills also the condition (4.3).

In the following, the RVE is initially at rest and axisymmetric loading is prescribed by imposing in the plane, the stress amplitude:

$$\Sigma_{22} = \Sigma_{11} = \dot{p}t \, , \dot{p} = \text{constant} \geq 0 \text{ (positive in tension)} \tag{4.5}$$

where $\dot{p}$ denotes the stress rate. Various types of conditions (in stress or in velocity) imposed in the axial direction ($x_3 = \pm l$) will also be considered.

4.3 Plane strain

We first focus on the dynamic expansion of porous materials under plane strain (D_{33}=0) configuration with $\Sigma_{11} = \Sigma_{22} = \dot{p}t$. So the length of the cylinder is fixed. Under axisymmetric plane strain loading conditions, as mentioned by Gurson [15], the static stress is spherical with the mean static stress under void expansion (i.e. when $D_{\text{m}} > 0$) expressed as:

$$\Sigma_{\text{m}} = \Sigma_{\text{m}}^{\text{static}} = \frac{\sigma_0}{\sqrt{3}} \ln\left(\frac{1}{f}\right) \tag{4.6}$$

As a consequence, when micro-inertia is neglected, plane strain with axisymmetric loading condition is akin to the hydrostatic loading path. This situation is no more valid when micro-inertia effects are included since Σ_{33}^{dyn} is different from $\Sigma_{22}^{\text{dyn}} = \Sigma_{11}^{\text{dyn}}$, see Eqs (3.41-3.43). Consequently, the macroscopic stress tensor is no more spherical and $\Sigma_{33} \neq \Sigma_{11}$.

A reference material is defined as being representative of porous aluminium. The yield stress of the matrix material σ_0 =100MPa and the matrix mass density ρ =2 700kg/m^3. For the reference material, the initial void radius a_0 =50μm and the initial porosity f_0 =0.0011.

Therefore the external radius of the RVE b_0 =1 500μm, see Table 4.1. Recall that under plane strain configuration, the length of the cylinder does not play a role so that no specific value of l_0 is needed in this section to define the material.

Fig. 4.1a (resp. Fig. 4.1b) represents the evolution of the porosity f versus time (resp. macroscopic stress $\Sigma_{11} = \dot{p}\,t$) for two values of the loading rate $\dot{p}$ =10 and 250MPa/ns. The porosity is limited to values below 0.3 because it is assumed that fracture occurs by direct impingement when the porosity f reaches this value. The results of the dynamic analysis (micro-inertia included) and the quasistatic approach (micro-inertia disregarded) are provided on Fig. 4.1. The stabilizing effect of micro-inertia is clearly highlighted, the dynamic void evolution being significantly delayed. This trend is well known from the literature for porous materials with spherical voids, for e.g. Glennie [12], Ortiz and Molinari [30], Tong and Ravichandran [39], Molinari and Mercier [26], Wu et al. [50], Czarnota et al. [9]. Note that the static analysis, for perfectly plastic matrix material, predicts an instantaneous void expansion once the yield limit is reached. Reminding that the plane strain and hydrostatic configurations coincide for the static approach, the stress at yield from Eq (4.6) is: $\Sigma_{11} = \frac{\sigma_0}{\sqrt{3}} \ln\left(\frac{1}{f_0}\right)$. With the set of parameters of Table 4.1, one obtains 0.39GPa leading to a time around t =39ns (resp. 1.57ns) when $\dot{p}$ =10MPa/ns (resp. $\dot{p}$ =250MPa/ns). Note that even if the void evolution is triggered earlier when $\dot{p}$ is larger, the micro-inertia effects are stronger. Indeed, Fig. 4.1b shows that the porous material sustains a much larger stress when $\dot{p}$ =250MPa/ns. This is attributed to the sole effect of micro-inertia, since the matrix response is perfectly plastic (no viscosity).

Fig. 4.2 shows the time evolution of the macroscopic stress components $\Sigma_{11} = \Sigma_{22} = \dot{p}t$

ρ [kg/m^3]	a_0 [μm]	b_0 [μm]	$f_0 = a_0^2/b_0^2$	σ_0 [MPa]
2 700	50	1 500	0.0011	100

Table 4.1: Reference material parameters, representative for porous aluminium.

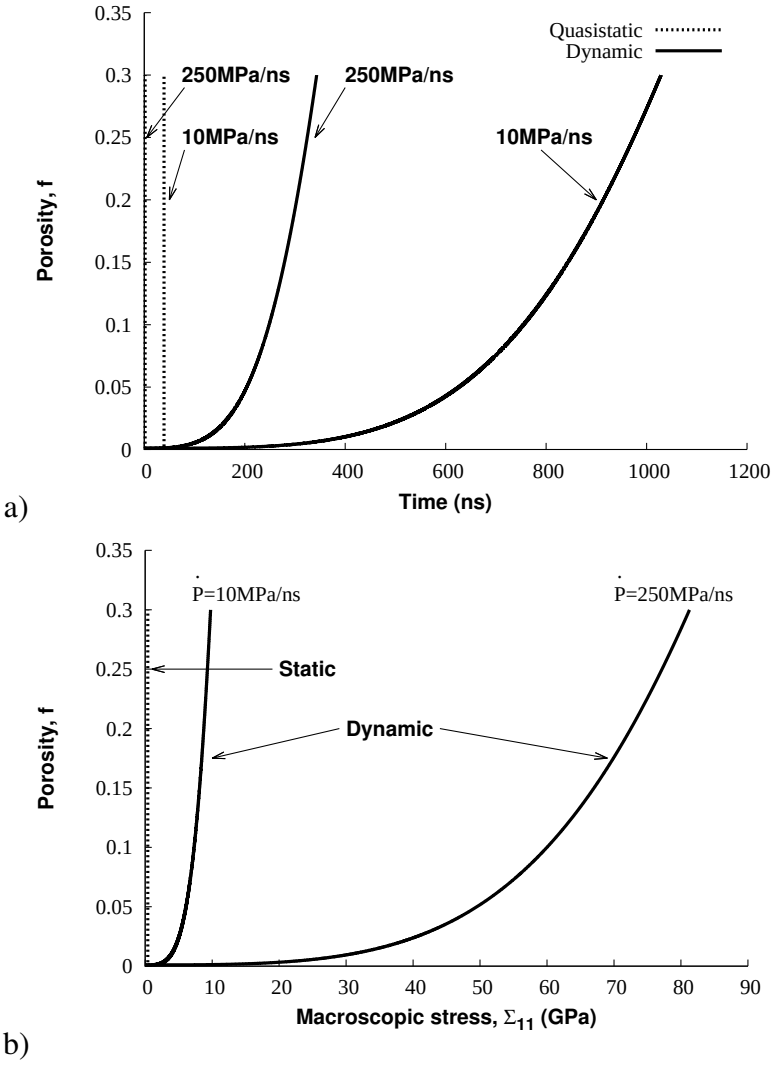

Figure 4.1: Evolution of the porosity f versus a) time and b) macroscopic stress $\Sigma_{11} = \Sigma_{22} = \dot{p}t$ under plane strain loading. A comparison between dynamic (micro-inertia dependent) and static (micro-inertia independent) analyses is carried out for two stress rates: $\dot{p}$ =10 MPa/ns and $\dot{p}$ =250 MPa/ns. Material parameters are provided in Table 4.1. For D_{33} =0, results are independent from the void length.

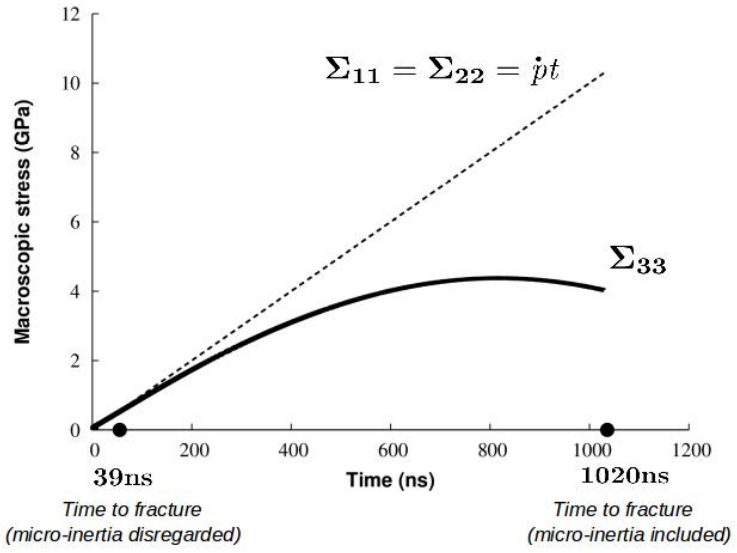

Figure 4.2: Time evolution of the macroscopic stress Σ_{33} under plane strain loading. The macroscopic stress $\Sigma_{11} = \Sigma_{22} = \dot{p}t$ is imposed with $\dot{p}$=10MPa/ns. Material parameters are listed in Table 4.1. The time to fracture (i.e. when f =0.3 is reached) is strongly influenced by micro-inertia (around 1020ns in the micro-inertia dependent calculation). Under quasistatic approach (micro-inertia being neglected), the porous material sustains very limited stress up to fracture which occurs at a time around 39ns.

(prescribed) and Σ_{33} calculated from the theory Eq (3.43) when plane strain case is adopted. From Fig. 4.2, it appears that the stress amplitude needed to maintain the cylinder at a constant length l_0 happens to decrease at large deformation stage even when the lateral stress is still increasing. This finding, which could have been hardly anticipated without the proposed analytical approach, clearly highlights the peculiar role of micro-inertia in the dynamic response of porous materials containing cylindrical voids.

Next the pore collapse is also discussed briefly. Here the RVE is subjected to axisymmetric compression loading with the stress rate, $\dot{p} < 0$ in Eq (4.5) (negative in compression). The reference configuration represented in Table 4.1, is also used. Two axisymmetric compressive loading are prescribed with $\dot{p}$=-10MPa/ns and $\dot{p}$=-250MPa/ns. Fig. 4.3 shows the significant effect of micro-inertia for both stress rates. For a stress rate, $\dot{p}$=-10MPa/ns, it is visible that the pore collapse time for quasi-static condition is 13.3ns while for the dynamic case due to

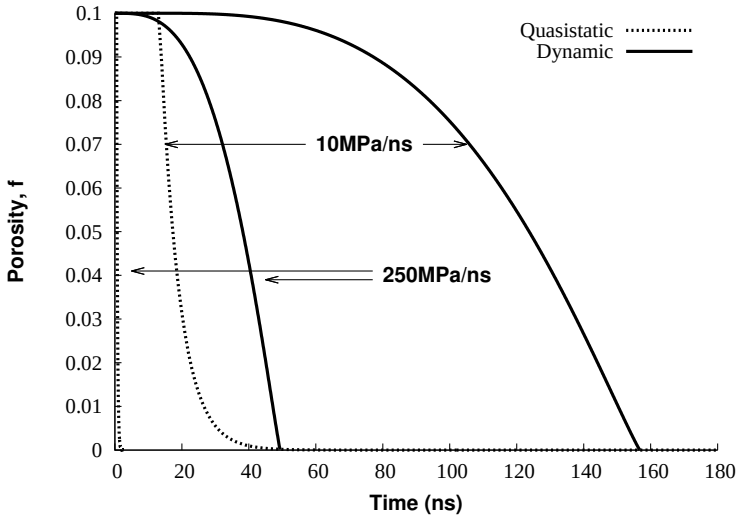

Figure 4.3: Collapse of the pore under plane strain loading, porosity f versus time. $\Sigma_{11} = \Sigma_{22} = \dot{p}t$. Comparison of dynamic (micro-inertia dependent) and quasi-static (micro-inertia independent) analyses is carried out for two stress rates: $\dot{p}$ =-10 MPa/ns and $\dot{p}$ =-250 MPa/ns. Material parameters are provided in Table 4.1. For D_{33} =0, results are independent of the void length (similar to Fig. 4.1).

micro-inertia effect, the pore collapse is delayed and pore closure occurs at 156.7ns. When the magnitude of stress rate is increased from $\dot{p}$=-10MPa/ns to $\dot{p}$=-250MPa/ns, the pore collapse is faster from 156.7ns to 49.3ns for the dynamic case and in quasi-static analysis the collapse happens at 0.53ns.

A parametric study is now conducted under plane strain configuration in order to figure out the effects of micro-inertia and of material properties on the time evolution of porosity. Fig. 4.4 portrays the influence of various material parameters on the dynamic void expansion. Results are obtained by varying the mass density, the flow stress level, the initial void radius and the initial porosity. Recall that the micro-inertia effects are scaled by the mass matrix density. As a consequence, when ρ is reduced, the stabilizing effect of micro-inertia is less pronounced and the rate of porosity is increased. The case with ρ =0.27kg/m^3 is hardly distinguishable from the static analysis conducted on the reference material. An increase of the flow stress delays the void expansion. This is due to the higher static stress carrying capacity of the porous material (see Eq (4.6)), and is not entirely attributed to micro-inertia effects. When the initial

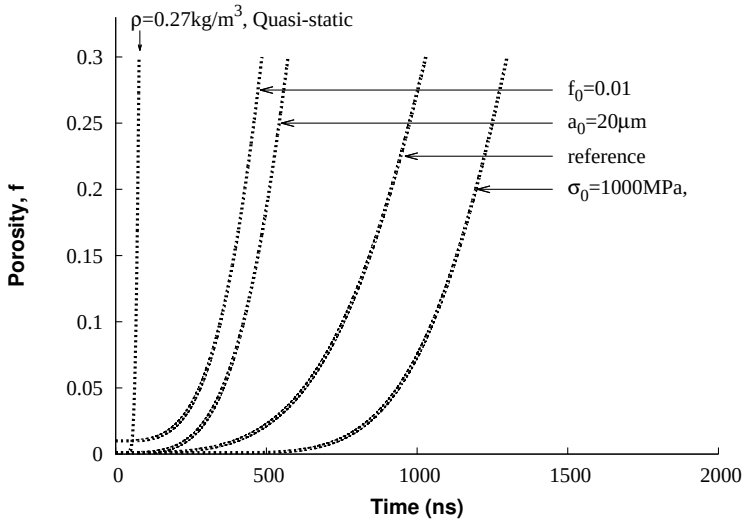

Figure 4.4: Effects of the mass density, of the initial radius, of the initial porosity and of the flow stress level, on the porosity evolution for dynamic expansion under plane strain configuration. The parameters of the reference material are listed in Table 4.1. The stress rate is $\dot{p}$ =10MPa/ns.

porosity is increased (from f_0 =0.0011 to 0.01) or the initial cavity radius is reduced (from a_0 =50 to 20μm), the void expansion is accelerated. The first configuration reflects a porous material containing more voids of initial size a_0. In that case, the static stress is lower and the micro-inertia is reduced, because the void is surrounded by less matrix. The second case is representative of a porous material containing smaller voids for which the micro-inertia effects are also reduced. The results provided in Fig. 4.4 again confirm previous trends found in the literature for spherical and spheroidal voids.

4.4 Hydrostatic loading

We now consider hydrostatic loading with:

$$\Sigma_{11} = \Sigma_{22} = \Sigma_{33} = \Sigma_{\rm m} = \dot{p}\, t \quad \dot{p} > 0 \tag{4.7}$$

where $\dot{p}$ coincides here with the mean stress rate $\Sigma_{\rm m}$. Note that since $\Sigma_{33}^{\rm dyn} \neq \Sigma_{11}^{\rm dyn}$, see Eq (4.1), the dynamic stress tensor is not spherical, and consequently the same applies for the static stress

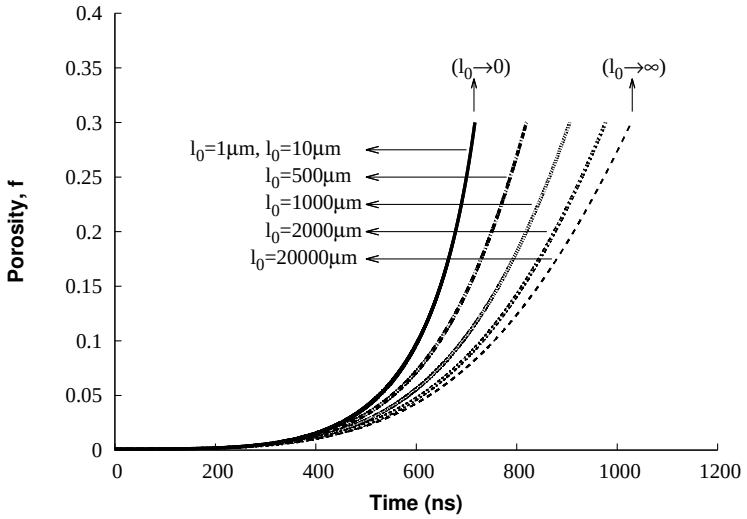

Figure 4.5: Effect of the initial length on the time evolution of the porosity under spherical loading. The material parameters are listed in Table 4.1 except for l_0 which is varying in the range [1:20 000]μm. The stress rate is $\dot{p}$ =10MPa/ns. The case where $l_0 \to \infty$ (resp. $l_0 \to$0) depicts the response of long (resp. short) cylinders under dynamic loading.

tensor. By contrast with the plane strain configuration, the length now plays a role in the overall response. Its influence will be explored first, then a specific attention will be put on the case of short cylinders where $l_0 \to 0$.

Fig. 4.5 illustrates the porosity evolution for the reference material with parameters listed in Table 4.1 considering various values of the initial length ranging from 1 to 20 000μm, initial f_0, ρa_0^2 and stress rate $\dot{p}$ being fixed. It is shown that an increase in initial axial length l_0 leads to the delay of the void evolution. This illustrates the stabilizing effect of micro-inertia modulated this time by the additional influence of the length of the cylindrical void. From Fig. 4.5, it is seen that the porosity evolves between two asymptotic responses. The first one is obtained when the initial length adopts a large value l_0 =20 000μm and depicts the response of elongated cylinders. Within that configuration it is observed that the porosity evolution under spherical loading ($\Sigma_{11} = \Sigma_{22} = \Sigma_{33} = \dot{p}t$) coincides with the results of Fig. 4.1a obtained under plane strain condition ($\Sigma_{11} = \Sigma_{22} = \dot{p}t$ and D_{33} =0). However, it has been shown in Fig. 4.2 that, due to micro-inertia effects, the axial stress Σ_{33} resulting from plane strain loading is different

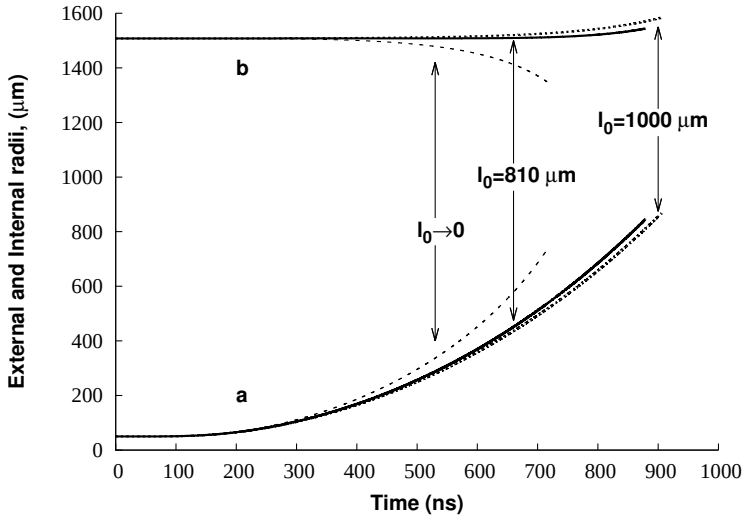

Figure 4.6: Time evolution, under spherical loading, of the external and internal radii for $l_0 \rightarrow$0, l_0 =810 and 1 000μm. Material parameters, displayed in Table 4.1, are those of Fig. 4.5 with stress rate, $\dot{p}$ =10MPa/ns.

from $\dot{p}t$ (which is the case here under spherical loading).

The second asymptotic response, revealed with l_0 =1μm, describes the response of short cylinders ($l_0 \rightarrow 0$) under dynamic loading. This situation can be retrieved from Eq (4.2) which also implies that the dynamic stress expressed by Eq (4.1) is not depending on l_0. This case of short cylinders under dynamic loading is investigated now more deeply.

From Fig. 4.5, we isolate the cases $l_0 \rightarrow$0 and l_0 =1 000μm which are obtained for material parameters listed in Table 4.1 and $\dot{p}$ =10MPa/ns. Fig. 4.6 displays the time evolution of the external (b) and internal (a) radii for $l_0 \rightarrow 0$ and l_0 =1 000μm. For further insight, the case where l_0 =810μm is also presented. When the initial length is large enough, e.g. l_0 =1 000μm or larger, the porosity growth is characterized by the increase of the external (b) and internal (a) void radii. This result is classically expected under quasistatic conditions also. Interestingly, when $l_0 \rightarrow$0, the evolution of damage results from the reduction of the external radius b, while the internal radius a is still increasing. As a consequence, $D_{11} = \dot{b}/b$ is negative (after some time) when $l_0 \rightarrow$0 and positive when l_0 is large, as reflected by Fig. 4.7 where the time evolution of D_{11} is displayed. This observation in configuration evolution, revealed for short cylinders,

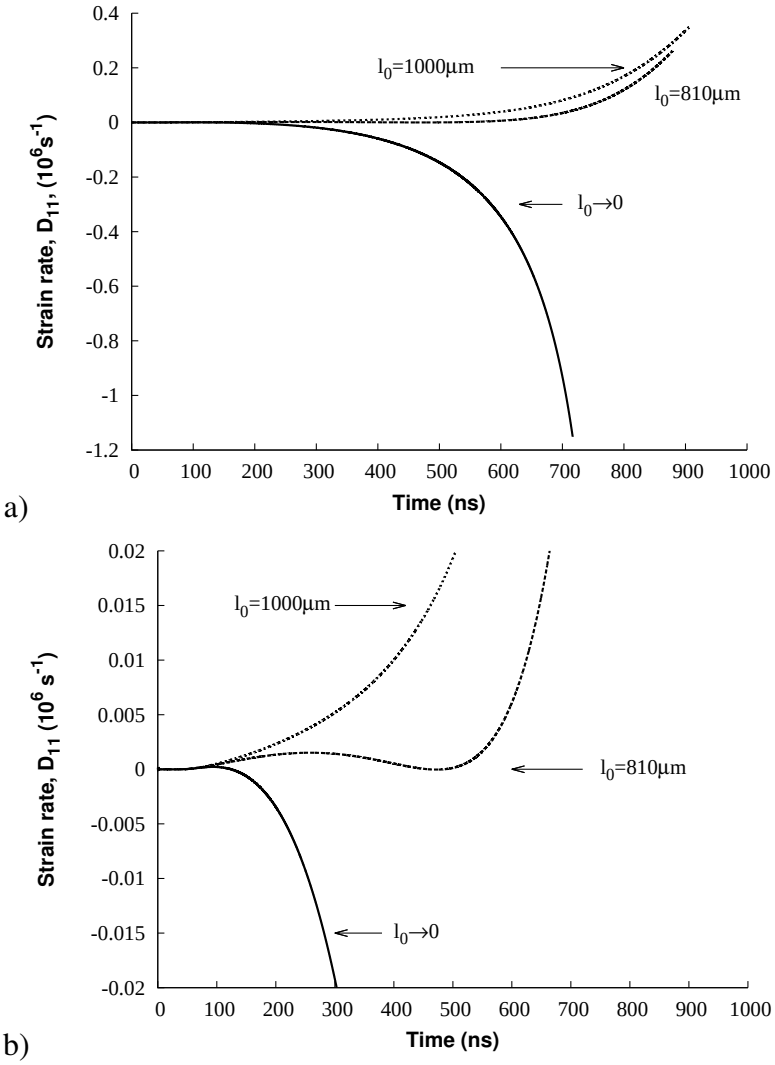

Figure 4.7: Time evolution, under spherical loading, of D_{11} for $l_0 \rightarrow 0$, l_0 =810 and 1 000μm. Material parameters are displayed in Table 4.1, and the stress rate, $\dot{p}$ =10MPa/ns. A magnified scale, where the y-axis is reduced, is proposed in b).

is counterintuitive and brings new insights in the behavior of porous materials under dynamic loading. This effect is due to micro-inertia and cannot be observed under quasistatic conditions. For intermediate values, it is expected that the strain rate oscillates due to the change of sign of $\dot{D}_{11}$. This is confirmed in Fig. 4.7b for l_0 =810μm. For this case, D_{11} is shown to first increase, then decrease, adopting negative values, and finally increase up to the final stage of the growth process. Note, from Fig. 4.6, that the late stage of the porosity growth for l_0 =810μm is quite similar to the case where l_0 =1 000μm.

In an attempt to identify by analytical means the critical length, denoted by $l_0^{\text{cr, approx.}}$, at which the porosity evolution switches from one mechanism (increase of the external radius) to another one (decrease of the external radius), an approximate analysis is proposed. Regarding the large stress amplitude developed during the process, we first assume that the static stress components are negligible when compared to the dynamic ones. Under spherical loading, this implies that $\Sigma_{33}^{\text{dyn}} = \Sigma_{11}^{\text{dyn}} = \dot{p}t$. For the approximate analysis, we also assume that the quadratic terms in D_{11} and D_{33} are negligible and that only linear terms in $\dot{D}_{11}$ and $\dot{D}_{33}$ are held in Eqs (A.31,A.32) of Appendix A. These assumptions lead to the following relationships:

$$\dot{p}t \;=\; \Sigma_{11}^{\text{dyn}} \;=\; \Sigma_{22}^{\text{dyn}} \;=\; \frac{\rho a^2}{4}\left\{2f^{-1}\ln\left(\frac{1}{f}\right)\dot{D}_{11} + \left[1 - f^{-1} + f^{-1}\ln\left(\frac{1}{f}\right)\right]\dot{D}_{33}\right\} \tag{4.8}$$

$$\begin{aligned}\dot{p}t = \Sigma_{33}^{\text{dyn}} = \frac{\rho a^2}{4}\Bigg\{&2\left[1 + f^{-1}\ln\left(\frac{1}{f}\right) - f^{-1}\right]\dot{D}_{11} \\ &+ \left[f^{-1}\ln\left(\frac{1}{f}\right) - \frac{1}{2}\left(f^{-1} - 1\right)(3 - f)\right]\dot{D}_{33}\Bigg\} + \frac{\rho l^2}{3}(1 - f)\,\dot{D}_{33}\end{aligned} \tag{4.9}$$

which give after some manipulations:

$$\left(\frac{2l^2}{3b^2} - \frac{1-f}{4}\right)\dot{D}_{33} = \dot{D}_{11} \tag{4.10}$$

where relationship $b = f^{-1/2}a$ has been used. One can substitute $\dot{D}_{11}$ expressed by Eq (4.10) into Eq (4.8) to get:

$$\dot{D}_{33} = \frac{4\dot{p}t}{\rho b^2}\left[\left(\frac{l^2}{3b^2} + \frac{1+f}{2}\right)\ln\left(\frac{1}{f}\right) + f - 1\right]^{-1} \tag{4.11}$$

It can be seen that $\dot{D}_{33}$ is strictly positive when $\dot{p}$ >0 (see Fig. 4.8a). Therefore Eq. (4.10) reveals that $\dot{D}_{11} < 0$ when $l \to 0$. The critical length $l_0^{\text{cr, approx.}}$ is evaluated from Eq (4.10) with the conditon $\dot{D}_{11}$ =0. Assuming in addition that the porosity and length have slightly evolved, one obtains:

$$l_0^{\text{cr, approx.}} = \sqrt{\frac{3\,(1-f_0)}{8}}b_0 \tag{4.12}$$

Using this last equation with f_0 =0.0011, b_0 =1 500μm, one has $l_0^{\text{cr, approx.}}$ =916μm which is well compared to 810μm shown in Fig. 4.7.

Eq (4.12) indicates that the critical length solely involves b_0 and f_0, while being independent from the stress rate $\dot{p}$ and other material parameters. Various configurations have been considered serving at testing the validity of the analytical approximation. From Table 4.2, compiling all tested cases, one notes that the critical length $l_0^{\text{cr, approx.}}$ obtained from the analytical approximation (4.12), is relatively well predicting the value l_0^{cr} obtained from the complete theory. The analytical approximation supposes that the micro-inertia effects are strong enough so that the static stress can be neglected. As a matter of fact, when $\dot{p}$ is increased, the micro-inertia effects are enhanced and the value of $l_0^{\text{cr, approx.}}$ becomes closer to the value l_0^{cr} captured by the model.

	$\dot{p}$ [MPa/ns]	ρ [kg/m^3]	a_0 [μm]	b_0 [μm]	$f_0 = a_0^2/b_0^2$ /	σ_0 [MPa]	l_0^{cr} [μm]	$l_0^{\text{cr, approx.}}$ [μm]
ref	10	2 700	50	1 500	0.0011	100	810	916
#1	**100**	2 700	50	1 500	0.0011	100	880	916
#2	10	2 700	50	1 500	0.0011	**200**	760	916
#3	10	2 700	**150**	1 500	**0.01**	100	800	914
#4	10	2 700	**25**	**750**	0.0011	100	390	457
#5	10	2 700	50	**750**	**0.0044**	100	390	458

Table 4.2: Various configurations used to compute the critical length for $l_0 < l_0^{\text{cr}}$, $\dot{D}_{11} < 0$. The critical value l_0^{cr}, obtained from the complete modeling, is well compared to the analytical approximation $l_0^{\text{cr, approx.}}$ given by Eq (4.12)

By contrast, when σ_0 is increased, one notices from Table 4.2 that the gap between l_0^{cr} and $l_0^{\text{cr, approx.}}$ is getting larger. When b_0 is half the reference value, l_0^{cr} obtained from the complete theory is reduced by a factor of two, thus validating the mathematical dependence on b_0 in the analytical approximation. Finally, l_0^{cr} is also shown to be little sensitive to a variation in f_0, as reflected also from the analytical approximation of Eq (4.12).

The void growth to some extent is controlled by micro-inertia effect, i.e. kinetic energy stored in the matrix material in the vicinity of the void. For axisymmetric loadings without shear, the kinetic energy K stored in the unit cell is:

$$K = K_{axial} + K_{plane} = \frac{1}{2}\int_V \rho v_z^2 dV + \frac{1}{2}\int_V \rho v_r^2 dV \tag{4.13}$$

where $V = 2\pi b^2 l$ is the volume of the unit cell, $v_z = D_{33} z$ and $v_r = \left(\frac{2D_{11}+D_{33}}{2}\right)\left(\frac{b^2}{r}\right) - \frac{D_{33}}{2} r$. Therefore, the two contributions K_{axial} and K_{plane} can be evaluated in closed form:

$$K_{axial} = \rho\pi D_{33}^2 l^3 \frac{b^2-a^2}{3} \tag{4.14}$$

$$K_{plane} = \rho\pi l \left[\frac{(\text{tr}\mathbf{D})^2}{2} b^2 \ln\frac{b}{a} - \frac{\text{tr}(\mathbf{D})D_{33}}{2} b^2(b^2-a^2) + \frac{D_{33}^2}{8}(b^4-a^4)\right] \tag{4.15}$$

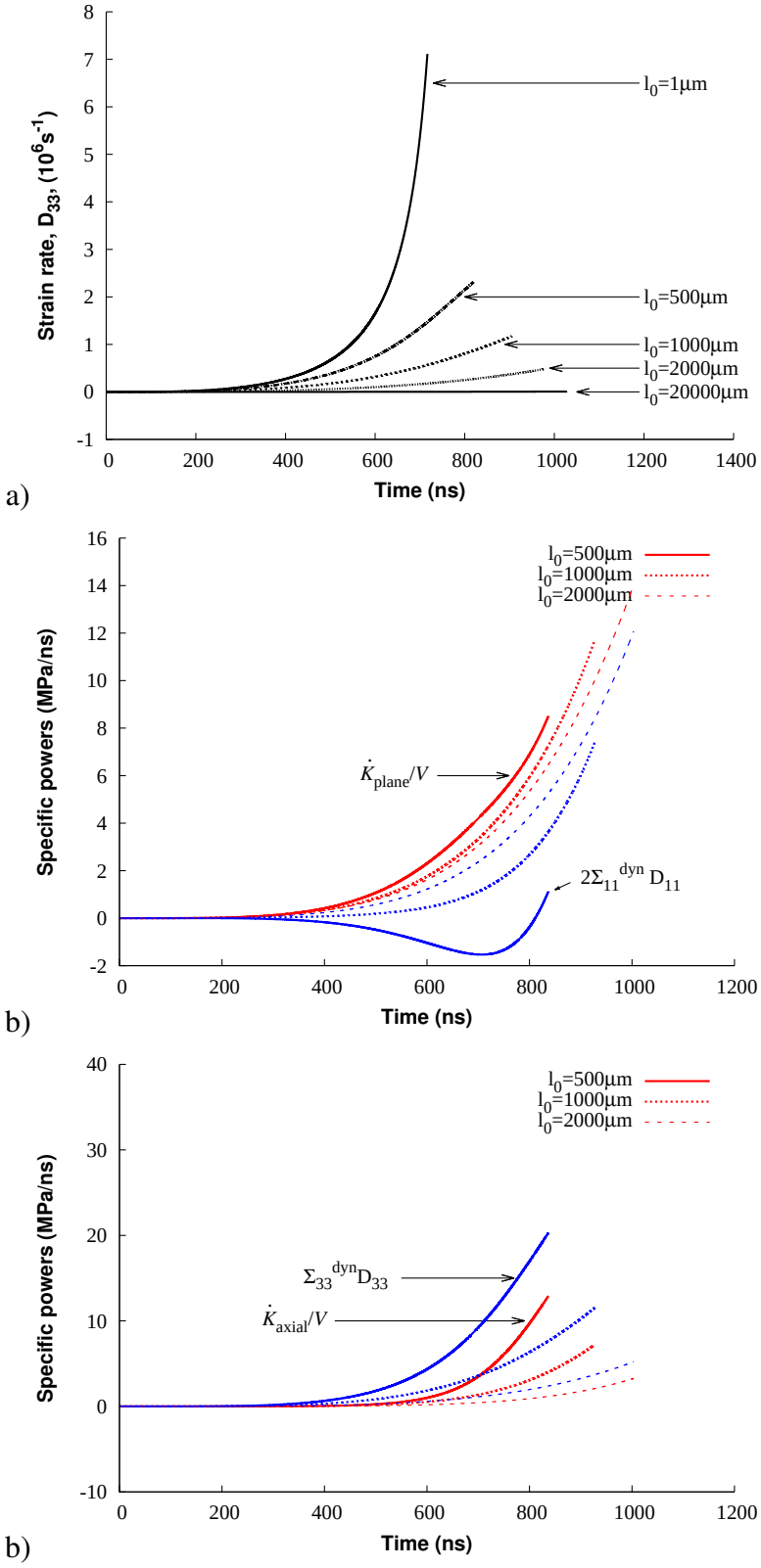

Figure 4.8: a) Time evolution of D_{33} under spherical loading, the initial length ranging from 1 to 20000μm - Specific powers in b) the plane, see Eq. (4.17), and c) the axial direction, see Eq. (4.18), for l_0=500, 1000, 2000μm. Other material parameters are displayed in Table 4.1 with stress rate, $\dot{p}$ =10MPa/ns.

Note that for plane strain loading, or when the initial length adopts very large values, $K_{axial} = 0$ and $K_{plane} = 2\rho\pi D_{11}^2 b^2 l \ln \frac{b}{a}$. The kinetic energy in the RVE is purely planar. From Eqs (4.14) and (4.15), expressions for $\dot{K}_{axial}$ and $\dot{K}_{plane}$ can be found. Since the matrix material is volume preserving, then one has: $l(b^2 - a^2) = c^{st}$. Therefore, the rate of kinetic energy in the axial direction is:

$$\dot{K}_{axial} = 2\rho\pi \frac{l^3(b^2 - a^2)}{3}(\dot{D}_{33}D_{33} + D_{33}^3) \tag{4.16}$$

Similarly, $\dot{K}_{plane}$ has been evaluated (results not presented here). For axisymmetric loadings without shear, the macroscopic dynamic stress is given in Eq (A.33) of Appendix A. The rate of kinetic energy in the plane direction is found to be related to the dynamic stress as:

$$\dot{K}_{plane} = V(2\Sigma_{11}^{dyn} D_{11} + \rho a^2 G D_{33}) \tag{4.17}$$

The rate of kinetic energy in the axial direction is given by:

$$\dot{K}_{axial} = V(\Sigma_{33}^{dyn} D_{33} - \rho a^2 G D_{33}) \tag{4.18}$$

So it has been checked that:

$$\dot{K}_{plane} + \dot{K}_{axial} = V\Sigma^{dyn} : D \tag{4.19}$$

The term $V\rho a^2 G D_{33}$, which is vanishing under plane strain loading, corresponds to a transfer term between the two contributions $\dot{K}_{plane}$ and $\dot{K}_{axial}$ of the total kinetic energy.

Fig. 4.8a shows the macroscopic strain rate D_{33} versus time, for the reference material under spherical loading with parameters listed in Table 4.1 considering various values of the initial length l_0 ranging from 1 to 20 000μm. An increase in initial length l_0 induces a decrease in

macroscopic strain rate D_{33} (see Fig. 4.8a). Next, we compare in Fig. 4.8b the rate of work per unit volume done by the dynamic stress in the plane, $2\Sigma_{11}^{dyn}D_{11}$, to the rate of kinetic energy in the plane per unit volume $\frac{\dot{K}_{plane}}{V}$ for three initial lengths $l_0 = 500,\ 1000,\ 2000\mu m$. Fig. 4.8c displays the corresponding quantities for the axial direction, *i.e.* $\Sigma_{33}^{dyn}D_{33}$ compared to the rate of external work in the axial direction $\frac{\dot{K}_{axial}}{V}$. Note that under such high level of imposed spherical loading ($\dot{p}$ =10MPa/ns), the static stress playing almost no role in the overall response, the dynamic stress is closed to $\dot{p}t$. As a consequence, the rates of work per unit volume done by the dynamic stress in the plane $2\Sigma_{11}^{dyn}D_{11}$, and in the axial direction $\Sigma_{33}^{dyn}D_{33}$ could have been deduced from the time evolution of the strain rate components D_{11} and D_{33}. The results of Figs 4.8b and 4.8c illustrate the importance of the transfer term for various lengths. As l_0 becomes large, the magnitude of D_{33} is reduced, so is the magnitude of the transfer term. In plane strain loading, the rate of external work per unit volume in the plane $2\Sigma_{11}D_{11}$ and the rate of kinetic energy in the plane per unit volume $\frac{\dot{K}_{plane}}{V}$ will almost coincide, as the contribution of the static term is small.

4.5 Additional loading cases

In this section we complement the analysis by first considering the following boundary conditions: (i) homogeneous stress different from hydrostatic loading and (ii) imposed axial strain rate and homogeneous pressure on the lateral surface.

Stress boundary conditions of two different types are first explored, see Table 4.3. Case 1 corresponds to $\Sigma_{11} = \Sigma_{22} = 0$ and $\Sigma_{33} = \dot{p}t$. Case 2 is obtained for $\Sigma_{11} = \Sigma_{22} = \dot{p}t$, $\Sigma_{33} = 0$. The stress triaxiality, defined by $\chi = \frac{\Sigma_{\mathrm{m}}}{\Sigma_{\mathrm{eq}}}$, is equal to 1/3 and 2/3 for Case 1 and Case 2, respectively. In Case 1, which corresponds to uniaxial stress loading, the void axis is aligned with the loading direction and D_{33} is naturally positive under remote extension. For Case 2, the

cylinder is stretched in the radial direction. The two cases serve as complementing the spherical loading addressed previously. Note that within the adopted study, the macroscopic equivalent stress is $\dot{p}t$ for both $\chi = 1/3$ (Case 1) and 2/3 (Case 2), while vanishing under spherical loading. A fixed value of the stress rate, $\dot{p}$ =10MPa/ns, is adopted in this section. The reference material parameters listed in Table 4.1 are first considered.

Fig. 4.9 shows the time evolution of the porosity for Case 1 and Case 2 when $l_0 = 2\,000\mu$m (Fig. 4.9a) and l_0 =10μm (Fig. 4.9b). The response under spherical loading is also reported for comparison purpose. The initial porosity is f_0 =0.0011 in all calculations. Since a static analysis provides for the porous material a time to fracture around 10ns for both Case 1 and Case 2, Fig. 4.9 clearly illustrates that micro-inertia effects are important for all stress triaxialities. Note the stabilizing effect of the length of the cylinder during uniaxial loading (Case 1), due to an enhancement of global inertia at large value l_0 =2 000μm, see Fig. 4.9a. It is seen by comparing Figs 4.9a and b, that the response under spherical loading is slightly sensitive to a reduction in l_0, see also Fig. 4.5. By contrast, for the two other cases, the porosity evolution is strongly depending on l_0.

Of particular situation, Fig. 4.9a and b show that the void may collapse under loading Case 2 ($\chi = 2/3$). To have a better explanation of the situation, Fig. 4.10a provides the time evolution of the internal a and external b radii and Fig. 4.10b shows the time evolution of D_{11} and D_{33}. In fact, when the top and bottom surfaces of the cylinder are traction-free with $\dot{p}$ >0

	$\chi = \frac{\Sigma_m}{\Sigma_{eq}}$	$\Sigma_{11} = \Sigma_{22}$	Σ_{33}
Spherical loading	∞	$\dot{p}\,t$	$\dot{p}\,t$
Case 1	1/3	0	$\dot{p}\,t$
Case 2	2/3	$\dot{p}\,t$	0

Table 4.3: Loading configurations and corresponding triaxialities.

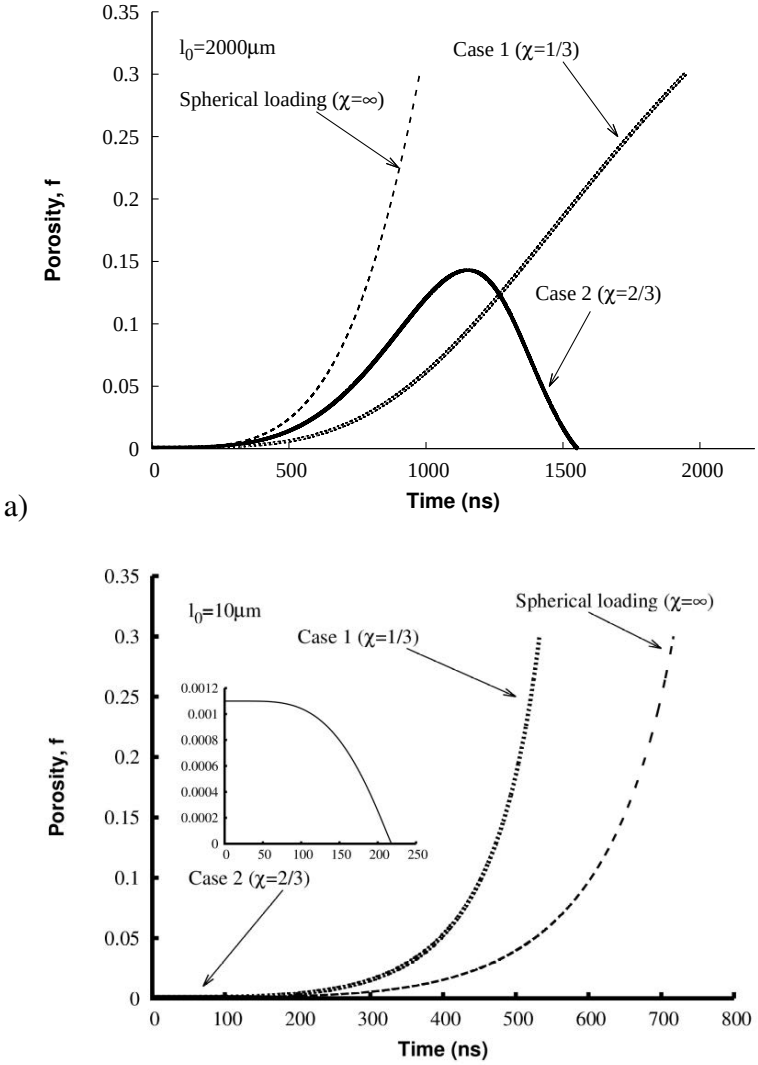

Figure 4.9: Time evolution of the porosity for spherical loading and for Case 1 and Case 2 under dynamic conditions, see Table 4.3. The stress amplitude is $\dot{p}t$ with $\dot{p}$ =10MPa/ns. The initial length is a) l_0 =2 000μm, b) l_0 =10μm. Other material parameters are listed in Table 4.1.

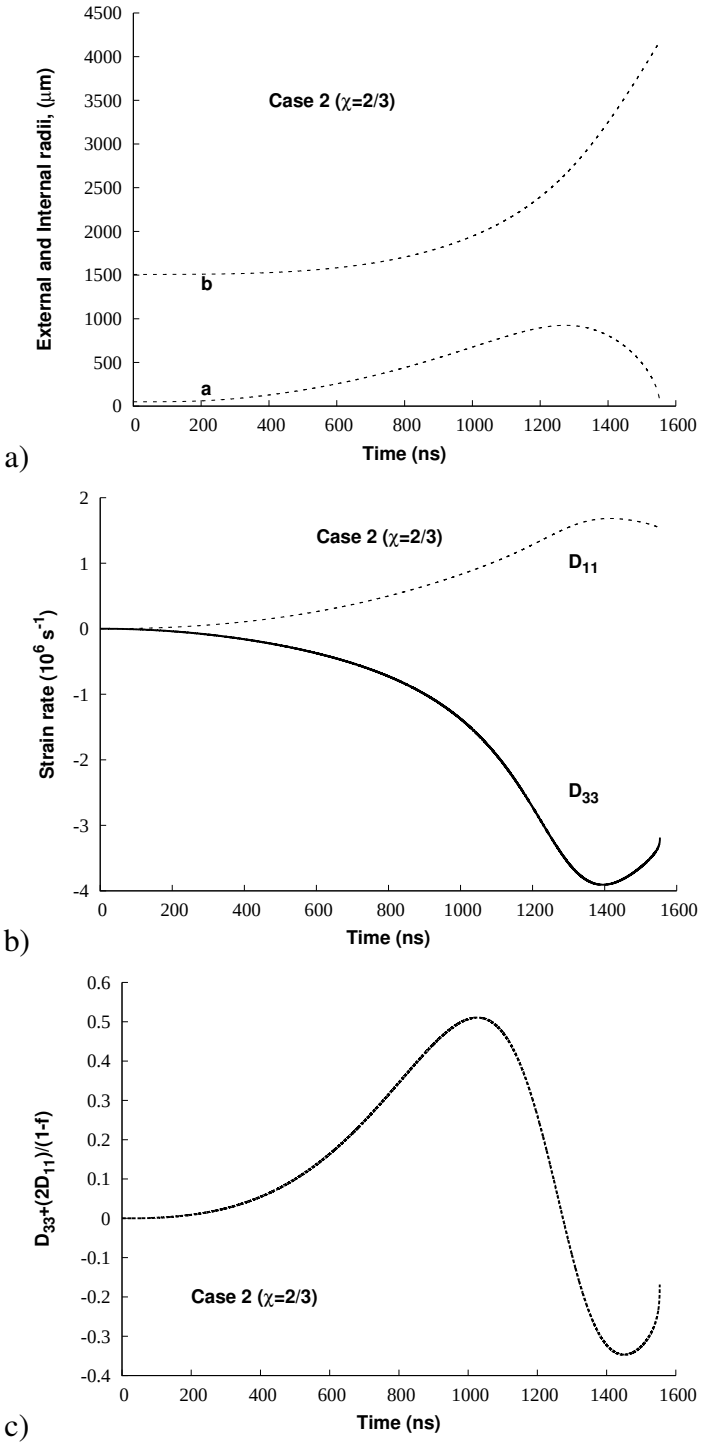

Figure 4.10: Time evolution of a) the void radius a and external radius b and b) the macroscopic strain rate components D_{11} and D_{33} c) $D_{33} + 2\frac{D_{11}}{(1-f)}$, for Case 2: $\Sigma_{11} = \Sigma_{22} = \dot{p}t$ with $\dot{p}$ =10MPa/ns, $\Sigma_{33} = 0$. The initial length is l_0 =2 000μm, other material parameters being listed in Table 4.1.

imposed in the radial direction (Case 2), the length of the cylinder is naturally reduced (i.e. D_{33} <0). At the same time, the external radius is always increased whereas the internal void radius is first increased before void collapse occurs at the final stage. From Fig. 4.10c, the term $D_{33} + 2D_{33}/(1-f)$ is negative after some time. From Eq (3.8), this means that $\dot{a}$ <0. This peculiar behavior results only from micro-inertia. Indeed, in a quasistatic analysis, it can be easily shown from the Gurson model, that when $\Sigma_{\gamma\gamma} = \Sigma_{11} + \Sigma_{22}$ is positive, then $D_{\mathrm{m}} > 0$. So the porosity is increasing and no void collapse can occur within a micro-inertia independent approach. In addition, in the quasistatic approach l is decreasing while a and b are both increasing.

Case 2 is investigated more deeply by varying ρ (l_0 =2 000μm being fixed, Fig. 4.11a) and l_0 (ρ =2 700kg/m^3 being fixed, Fig. 4.11b). When ρ is reduced (smaller effects of micro-inertia), the porosity growth is triggered for earlier time and develops faster. Note that micro-inertia effects are always included in the complete theory and that void collapse occurs even for low values of ρ. The static response would be obtained with a very low value of ρ for which, as previously stated, one would observe an instantaneous growth without collapse (at $t \simeq$10ns).

The effect of l_0 portrayed in Fig. 4.11b confirms the important role of the axial length of the cylinder on the dynamic response. As l_0 is reduced, the collapse process is triggered earlier. Indeed it can be shown that as l decreases, D_{33} is still negative but with larger absolute value ($D_{33} < 0$), so the quantity $D_{33} + 2D_{11}/(1-f)$ become negative earlier. Remind that the micro-inertia stress is the sum of two terms, the first being scaled by ρa^2, the second by ρl^2. Thus, when $l_0 \to 0$ micro-inertia is solely dependent upon the void radius. One finally notes from Fig. 4.11b that the response obtained with a large value of l_0, e.g. l_0 =10 000μm, coincide with the plane strain case of Fig. 4.1, in terms of porosity evolution only.

The uniaxial stress loading (Case 1) is next explored by varying the mass matrix density

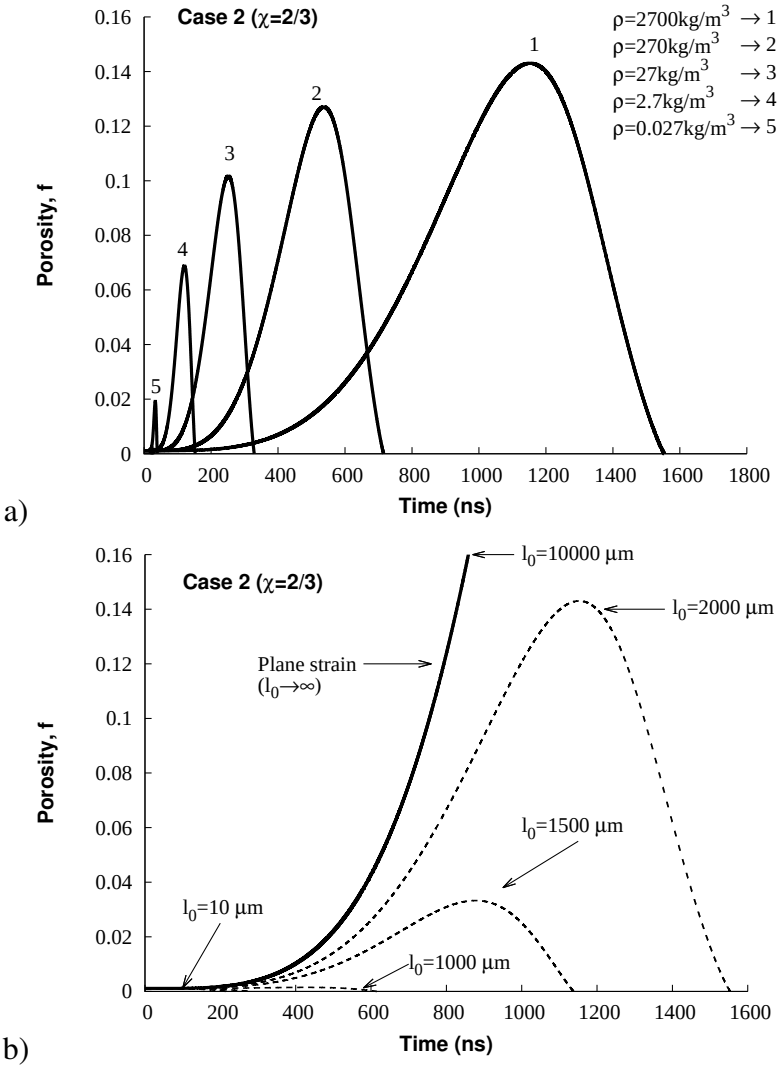

Figure 4.11: Influence of a) the mass matrix density with l_0=2000μm and b) the initial void length with ρ=2700kg/m^3 for Case 2: $\Sigma_{11} = \Sigma_{22} = \dot{p}t$ with $\dot{p}$ =10MPa/ns, $\Sigma_{33} = 0$. The other material parameters are displayed in Table 4.1. The response with l_0 =10 000μm provides the plane strain case of Fig. 4.1, in terms of porosity evolution only.

(with fixed l_0 =2 000μm in Fig. 4.12a) and the initial length of the cylinder (ρ =2 700kg/m^3 being fixed in Fig.4.12b). Again, when l_0 is fixed and ρ is reduced, the micro-inertia effects are lowered down, and the porosity growth occurs earlier. But, most interestingly, when ρ is lower than 270kg/m^3, the critical porosity f_c =0.3 (for which fracture is assumed to occur) is not reached during the dynamic process. Instead of continuously increasing up to the ultimate fracture at $f = f_c$, the porosity is reduced and tends to a stabilized value. This plateau is characterized by the collective decrease of a and b, f being constant. Fig. 4.13a illustrates the evolution of the internal and external cell radii while Fig. 4.13b presents the time evolution of D_{11} and D_{33}. Note from the last figure, that since $\dot{f} \simeq 0$ at late stage of the process, D_{11} is close to $-D_{33}/2$.

Increasing l_0 with fixed ρ also favors the occurrence of a plateau. Indeed, from Fig. 4.12b obtained with ρ =2700kg/m^3, it appears that when l_0 =5 000μm, the porosity is frozen after some time ($t > 8\,000$ns) while the cell internal and external radii are still decreasing. When l_0 is reduced, the porosity growth is faster and the critical porosity is reached prior to any decrease in f. Note that a plateau could have been observed by adopting a larger critical porosity f_c for lower values of l_0.

The length of the cylinder plays an important role in the dynamic response of cylindrical voids. In the last two examples, the dynamic behavior may be characterized by a saturation in porosity evolution or a collapse process. These effects are solely due to micro-inertia.

We now consider the loading path where homogeneous pressure is prescribed on the lateral surface, $\Sigma_{11} = \Sigma_{22} = \dot{p}t$, while a constant strain rate D_{33} is imposed in the longitudinal direction. In that case the displacement of the top surface is following the law: $l = l_0 \exp(D_{33}t)$. Fig. 4.14 shows the evolution of the porosity for various values of D_{33} up to 10^6s^{-1} with $\dot{p}$ =10MPa/ns (Fig. 4.14a) and $\dot{p}$ =100MPa/ns (Fig. 4.14b). The reference material of Ta-

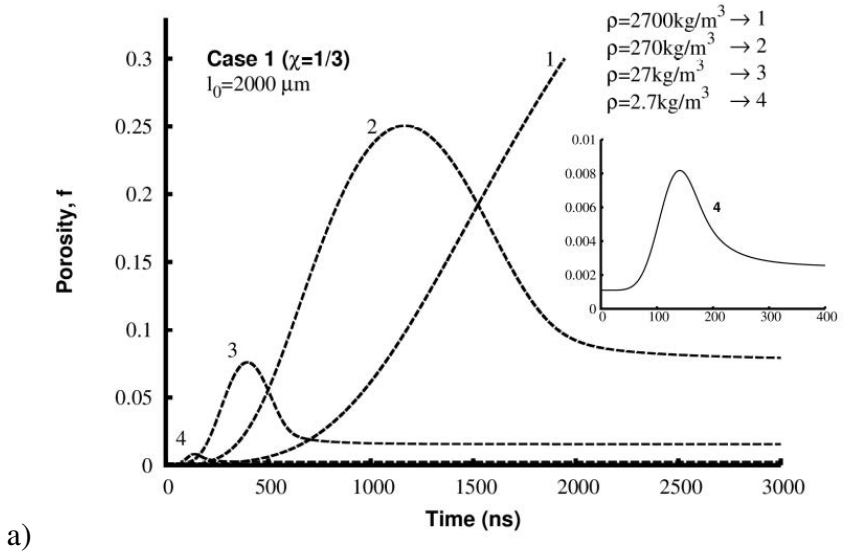

Figure 4.12: Influence of a) the mass matrix density with l_0=2 000μm and b) the initial void length with ρ=2700kg/m^3 on porosity evolution for loading Case 1 (uniaxial stress). The other material parameters are displayed in Table 4.1. The evolution of the axial stress is given by $\Sigma_{33} = \dot{p}t$ with $\dot{p}$ =10MPa/ns.

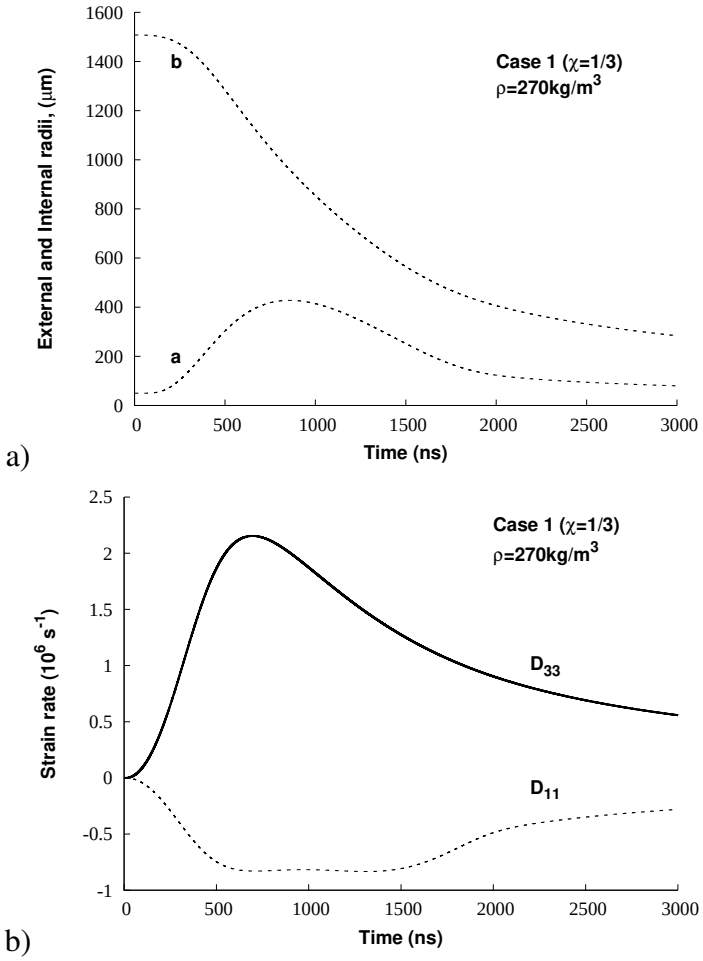

Figure 4.13: Time evolution of a) the void radius a and external radius b and b) the macroscopic strain rate components D_{11} and D_{33} for loading Case 1 (uniaxial stress with $\Sigma_{33} = \dot{p}t$, $\dot{p}$ =10MPa/ns). The initial length is l_0 =2 000μm, the mass matrix density is ρ =270kg/m^3, other material parameters being listed in Table 4.1.

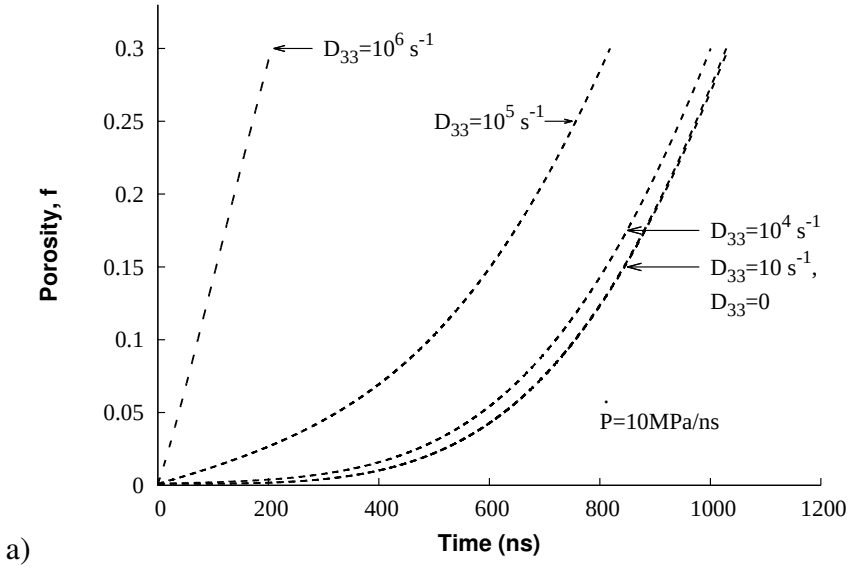

a)

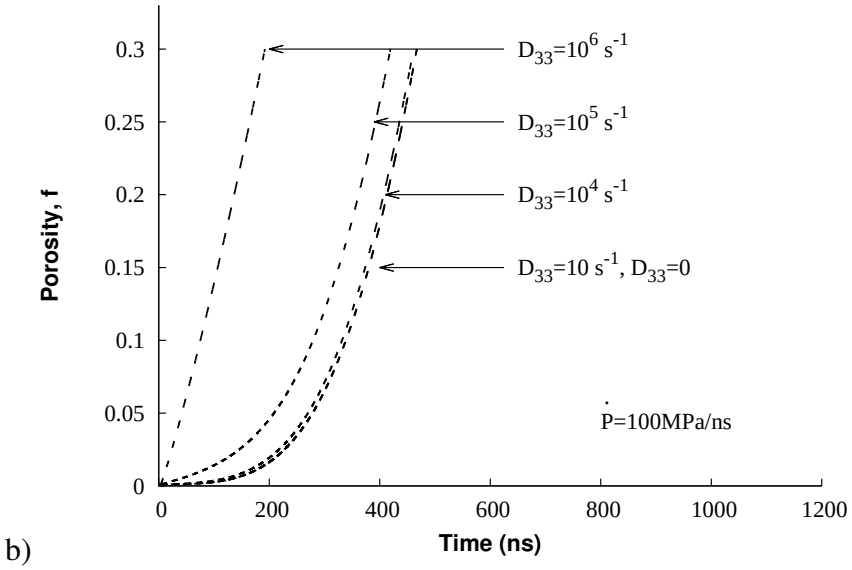

b)

Figure 4.14: Time evolution, under imposed constant strain rate D_{33} and prescribed $\Sigma_{11} = \Sigma_{22} = \dot{p}t$ with a) $\dot{p}$ =10MPa/ns b) $\dot{p}$ =100MPa/ns. The initial length is l_0 =100μm, other material parameters being listed in Table 4.1.

ble 4.1 is adopted with l_0 =100μm. As expected, when the strain rate D_{33} increases, the porosity growth is accelerated. Most interestingly, when comparing Fig. 4.14a and b, one notes that when D_{33} =10^{6}s^{-1} the evolution of the porosity is almost identical for the two applied pressure rates, $\dot{p}$=10MPa/ns (Fig. 4.14a) and $\dot{p}$=100MPa/ns (Fig. 4.14b). In such situation (i.e. under intense imposed constant strain rate), the void evolution appears to be mostly governed by D_{33} and quite irrespective of the value of $\dot{p}$. Naturally, when D_{33} =0, the growth process is solely driven by the stress rate $\dot{p}$. For intermediate values, the evolution of the porosity results from both the influences of $\dot{p}$ and D_{33}. One has to mention also that if the stress rate $\dot{p}$ is further increased, it is expected that for the effect of the lateral stress ($\dot{p}t$) to be negligible, larger values of the strain rate D_{33} have to be considered.

In the last example, the in-plane macroscopic stress tensor components are still $\Sigma_{11} = \Sigma_{22} = \dot{p}t$ while a constant velocity $v_3 = \pm v_3^0$ is prescribed at $x_3 = \pm l$. The corresponding nominal strain rate is $D_{33}^0 = v_3^0/l_0$ and the displacement at the top boundary is $l = l_0(1 + D_{33}^0 t)$. It was demonstrated from the analysis of Eqs (4.1) and (4.4) conducted at the beginning of section 4.1, that the term related to l^2 in Σ_{33}^{dyn} vanishes. This is exemplified in Fig. 4.15 for the reference material (parameters given in Table 4.1) considering two cylinder lengths l_0 =1 000, 2 000μm and D_{33}^0 =10^{5}s^{-1}, 10^{6}s^{-1}. Note that, as for the configuration of an imposed constant strain rate addressed previously, the growth process is less dependent on $\dot{p}$ and is largely influenced by the imposed axial strain rate when D_{33}^0 is large, e.g. D_{33}^0=10^{6}s^{-1} in Fig. 4.15.

4.6 Conclusion

It is interesting to highlight the influence of the two geometrical characteristics of the cylindrical voids (i.e. length and radius) on damage evolution. It is worth noting that the effects of void length and radius can be separated. Indeed, the macroscopic dynamic stress in the axial

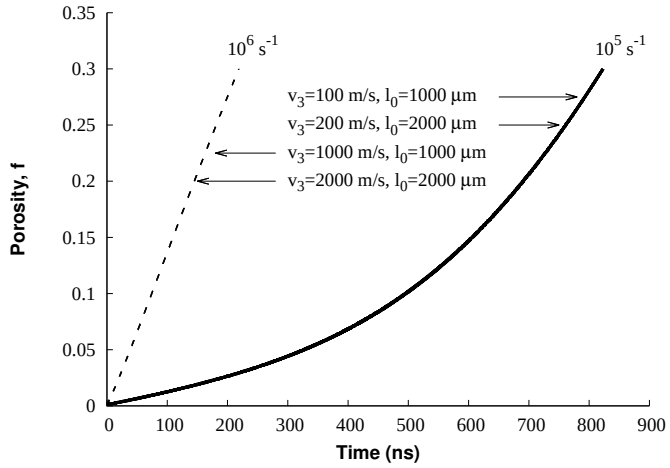

Figure 4.15: Time evolution of the porosity under imposed in-plane stress $\Sigma_{11} = \Sigma_{22} = \dot{p}t$ and constant velocity v_3^0. Calculations are performed for D_{33}^0 =$10^5 s^{-1}$ and $10^6 s^{-1}$ considering l_0 =1000 and 2000μm which infers various applied constant velocities. Other material parameters are given in Table 4.1.

direction appears as the summation of two terms: the first (resp. second) term is scaled by the matrix mass density and the square of the void radius (resp. void length).

A parametric study has been conducted under plane strain configuration, confirming the refraining effect of micro-inertia when modulated by the mass matrix density and the initial void size. In addition, under plane strain, the axial stress component is found to be decreasing with time at large deformation. This reflects that the stress needed to constrain the length of the cylinder is reduced because of micro-inertia.

The influence of the length of the cylindrical void has been revealed. In particular, for spherical stress loading, it has been shown that micro-inertia effects are more important for longer voids. At the same time, it was shown that two asymptotic responses in the time evolution of the porosity are emerging from the spherical loading path: the plane strain case is retrieved when $l_0 \to \infty$ and the case of short cylinders is obtained from $l_0 \to 0$.

The case of short cylinders reveals a peculiar damage evolution. In fact, the porosity is found to increase due to a reduction of the external radius and an increase of the void radius. This situation is solely due to micro-inertia effects.

The modeling has been applied to stress states with various triaxialities. Under radial expansion with traction free top and bottom surfaces, the void was found to collapse, at least for the reference set of material parameters. Under uniaxial stress loading, after an initial void growth, the porosity may decrease and reach a plateau. Under such case, the late stage of the deformation process is characterized by a continuous decrease of the internal and external radii.

Predictions of the present model have now to be verified against numerical simulations for various axisymmetric loading paths. This is the main goal of the next chapter.

Chapter 5

Finite element modeling

5.1 Introduction

To validate the proposed constitutive model, dynamic micromechanical computations based on cylindrical unit cells have been carried out with the finite element code ABAQUS/Explicit. Various axisymmetric models have been developed to depict the dynamic response under i) plane strain condition ii) hydrostatic loading conditions and iii) other loading cases considered in the thesis work. Since the matrix material is taken as rigid in the model, a large value of the Young's modulus has been adopted (6 300GPa). In addition, to approach the incompressibility condition for the matrix, a value of 0.499 for the Poisson's ratio has been used. Otherwise stated, these values, (E=6300GPa, ν=0.499) are adopted in finite element simulations. We propose at the end of this chapter, to investigate the influence of both elastic constants on FEM results.

For all configurations addressed in the thesis, the proposed analytical approach has been accurately compared to results obtained from numerical simulations. Here, only some important examples from each loading case have been selected to bring the comparison.

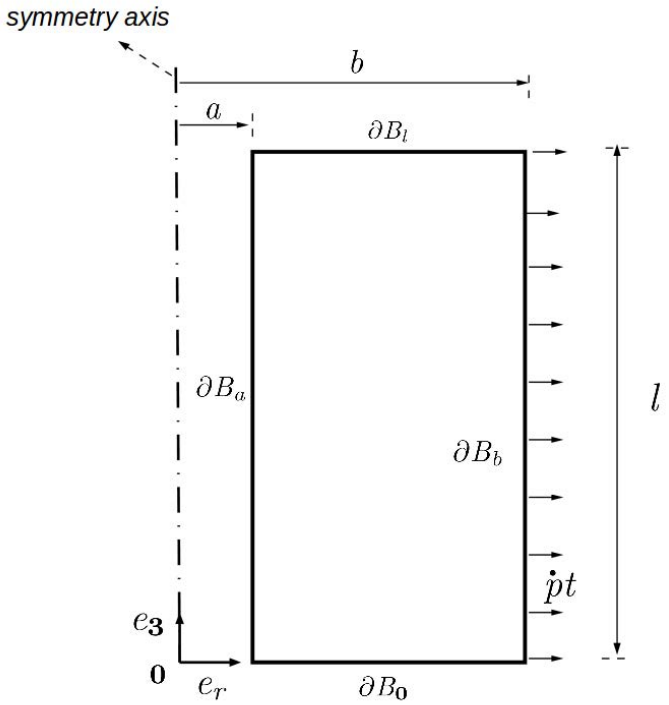

Figure 5.1: Finite element cylindrical unit cell of length l, inner radius a and external radius b used for various loading cases. The mesh is made with 4 node axisymmetric elements (CAX4R). The element size is 20μm$\times 40\mu$m.

5.2 Plane strain configuration

In this section, the goal is to validate results presented in section 4.3 (Fig. 4.1). For this case, the unit cell, illustrated on Fig. 5.1, is meshed with 4 node axisymmetric elements with reduced integration (CAX4R). The initial element size is about 20μm$\times 40\mu$m. Since the unit cell is expanded in the radial direction, elements are initially elongated in the axial direction, so as to prevent the element aspect ratio from excessive values during the deformation process. Kinematic conditions of the following form are considered on the boundary:

$$v_3(\boldsymbol{x},t) = 0 \text{ on } \partial B_0,\ v_3(\boldsymbol{x},t) = 0 \text{ on } \partial B_l \tag{5.1}$$

which account for the condition of symmetry at ∂B_0 and ensure the plane strain condition at ∂B_l. In addition, the following stress boundary conditions prevail (expressed in the cylindrical coordinate system):

$$\Sigma_{r3}(\boldsymbol{x},t) = \Sigma_{\theta 3}(\boldsymbol{x},t) = 0 \text{ on } \partial B_l \tag{5.2}$$

and

$$\Sigma_{rr}(\boldsymbol{x},t) = \dot{p}t,\ \Sigma_{\theta r}(\boldsymbol{x},t) = \Sigma_{3r}(\boldsymbol{x},t) = 0 \text{ on } \partial B_b \tag{5.3}$$

while the inner surface ∂B_a is traction free.

For the configuration of section 4.3, Fig. 4.1a, the loading rate is $\dot{p}$ =10MPa/ns, and material parameters are listed in Table 4.1. Fig. 5.2 shows that analytical results (solid line) coincide with Finite Element simulations (dots). In particular, the reduction of the axial stress Σ_{33} occurring at large deformation while the lateral stress is still increasing, is reproduced by both approaches, as observed in Fig 5.2b. Note that Σ_{33} is evaluated from the ratio of the axial force on ∂B_l divided by the current area πb^2.

It can be of interest to investigate whether a 2D FEM could provide consistent results in case of plane strain. Indeed, the length of the cylinder is not playing a role in the response, in terms of porosity and stress as observed in Eq (A.34) and (A.35). The cell, illustrated in Fig. 5.3a, is meshed with 4 node plane strain elements with reduced integration (CPE4R). The mesh is refined in the vicinity of void. More specifically, the mesh size at ∂B_a (resp. at ∂B_b) is 20μm x 92μm (resp. 589μm x 918μm). The following conditions of symmetry are considered:

$$v_x(\boldsymbol{x},t) = 0 \text{ on } \partial B_y,\ v_y(\boldsymbol{x},t) = 0 \text{ on } \partial B_x \tag{5.4}$$

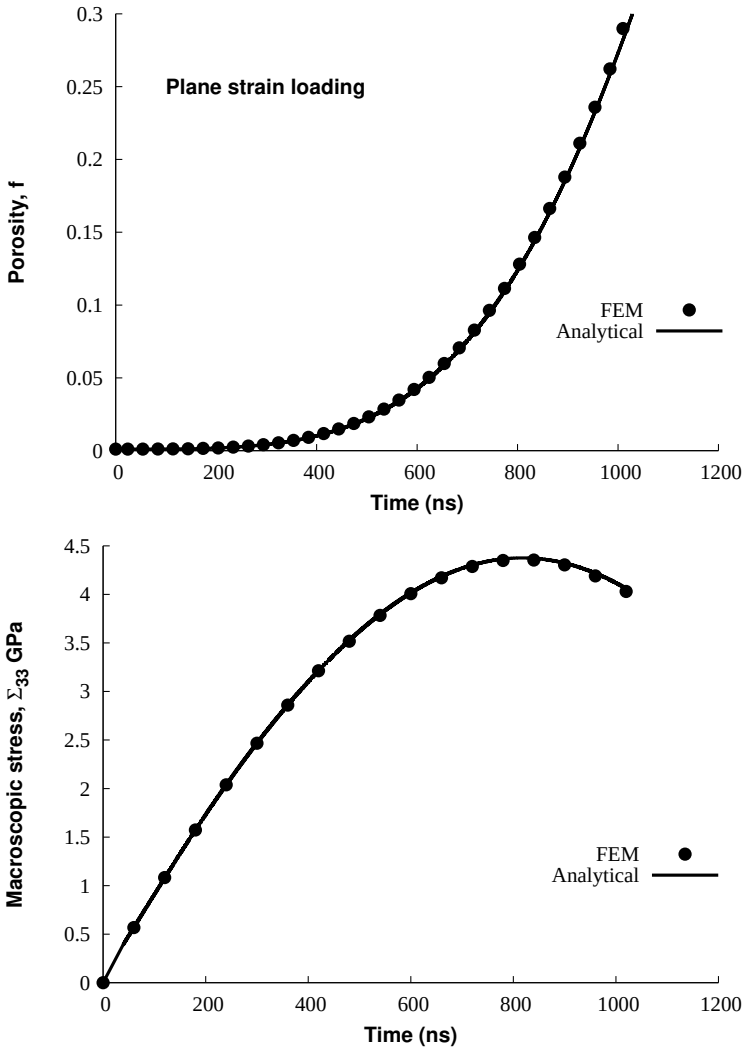

Figure 5.2: Comparison between FEM and analytical results for plane strain loading. Time evolution of a) the porosity and b) the axial stress. The stress rate is $\dot{p}$ =10MPa/ns. The reference material with parameters listed in Table 4.1 is considered.

while stress boundary conditions are prescribed as:

$$\Sigma_{\theta r}(\boldsymbol{x},t)=0,\ \Sigma_{rr}(\boldsymbol{x},t)=\dot{p}t,\ \Sigma_{3r}(\boldsymbol{x},t)=0 \text{ on } \partial B_b \tag{5.5}$$

The inner face ∂B_a remains traction free. As in section 5.2, the stress rate is $\dot{p}$=10MPa/ns and the material parameters of Table 4.1 are considered. Fig. 5.3b shows that the 2D plane strain model of Fig. 5.3a and axisymmetric model of Fig. 5.1 give identical results.

5.3 Hydrostatic loading

Let us consider the axisymmetric model of Fig. 5.1. Prescribing $\Sigma_{11}=\Sigma_{22}$ at the external boundary of the unit cell ($r=b$) presents no difficulties. Imposing uniform Σ_{33} on the top surface ($0\leq r\leq b$) where a void is present for $0\leq r\leq a$ is not straightforward. To overcome this difficulty, two strategies have been developed aiming at defining a model able to verify the proposed approach in case of hydrostatic loading. They give identical results and for completeness purpose, both will be presented in this section.

5.3.1 Boundary conditions inherited from the analytical model

The first approach relies on a two-step formalism. The solution of the considered configuration (prescribed hydrostatic loading condition) is searched by using the analytical approach presented in this manuscript. The resulting velocity field in the axial direction, denoted by $v_3^{\text{th.}}$, is collected and used as boundary condition in the finite element model of Fig. 5.1. Including the condition of symmetry, the set of kinematic boundary conditions is expressed as:

$$v_3(\boldsymbol{x},t)=0 \text{ on } \partial B_0,\quad v_3(\boldsymbol{x},t)=v_3^{\text{th.}} \text{ on } \partial B_l \tag{5.6}$$

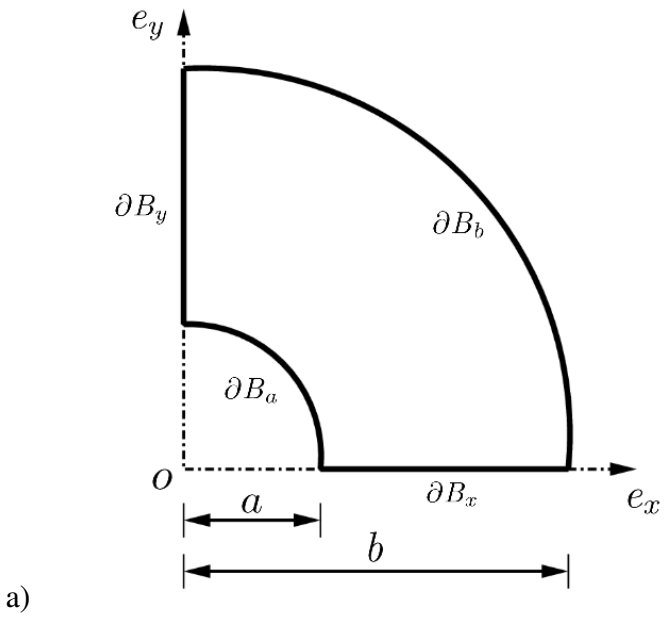

a)

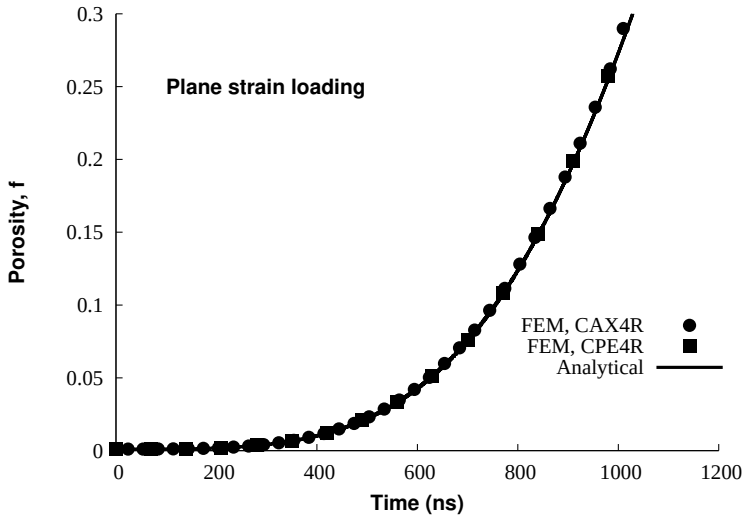

b)

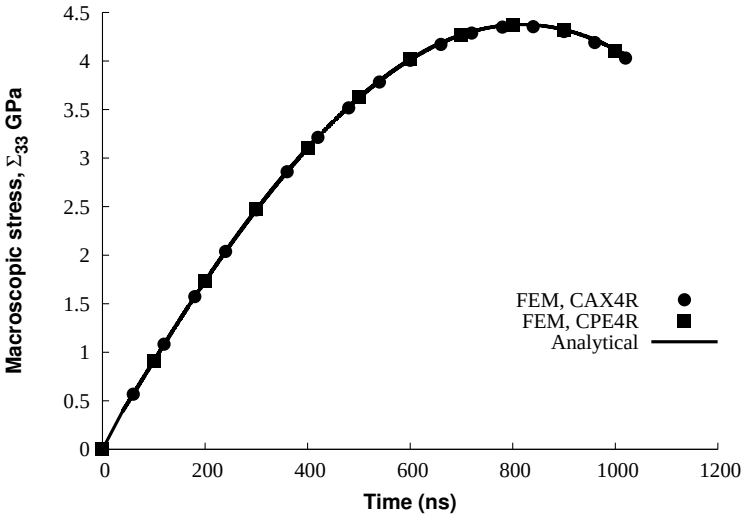

c)

Figure 5.3: a) Finite Element model of 2D unit cell of inner radius a and external radius b used for the plane strain problem. The mesh is made with 4 node plane strain elements with reduced integration (CPE4R). Comparison between FEM plane strain model (CPE4R), FEM axisymmetric model (CAX4R) and the analytical approach for the time evolution of b) porosity, f and c) axial stress, Σ_{33}. The reference material with parameters listed in Table 4.1 is considered. The stress rate is $\dot{p}$ =10MPa/ns.

complemented with the stress boundary conditions expressed by Eqs (5.2-5.3) and assuming that the void surface is traction free.

One has to mention that under intense imposed velocity $v_3^{\text{th.}}$, the shape of the unit cell can strongly deviate from its cylindrical shape. As a consequence, a supplementary constraint turned out to be necessary to prevent the unit cell from unexpected shape change. Specifically, the nodes located at the inner and outer vertical boundaries of the cylindrical void (∂B_a and ∂B_b in Fig. 5.1) are linked through a set of linear multi-point constraints so that, at each time of the deformation process, these surfaces remain vertical.

To illustrate the evolution of the cell when inner and outer surfaces are not forced to remain parallel, we consider the case where both constraints are removed. Fig 5.4a illustrates the shape change of the unit cell of Fig. 5.1 when linear multi-point constraint equation at the inner boundary ∂B_a and outer boundary ∂B_b are removed. Correspondingly, Fig. 5.4b illustrates the time evolution of the ratio a^2/b^2 evaluated at ∂B_0 and ∂B_l superimposed with the time evolution of the porosity obtained with the FEM calculation where kinematic constraints (ensuring that ∂B_a and ∂B_b remain planar) are implemented. It will be shown in Fig. 5.7, that this last result coincides with the analytical approach. Clearly, the ratio a^2/b^2, which stands as the porosity when the unit cell keeps its cylindrical shell is heterogeneous along the cylindrical axis when kinematic constraints are disregarded.

5.3.2 Closed unit-cell

The second approach consists of adopting a closed unit cell composed of a thin layer added at the top of the cylindrical void, see Fig. 5.5. If the top layer thickness, denoted by t_p in Fig. 5.5, is sufficiently small, the additional domain is of negligible mass. Therefore it should not affect the overall response of the unit cell under dynamic loading. Thus, imposing the macroscopic

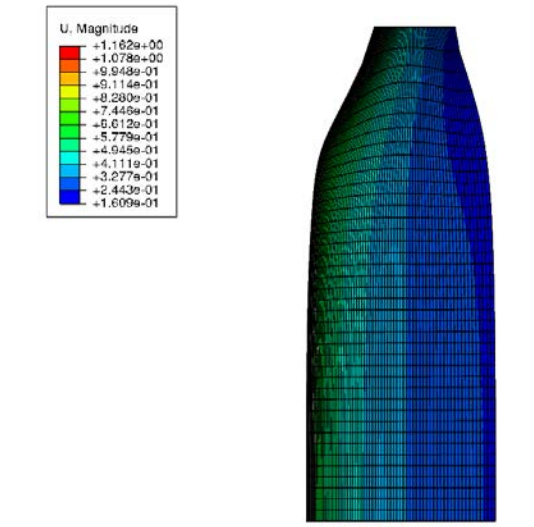

a)

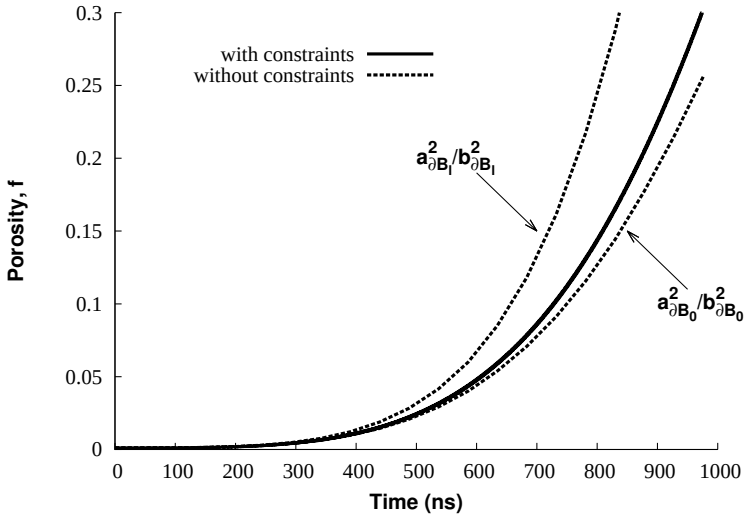

b)

Figure 5.4: a) Shape of the deformed unit cell at the end of the FE calculations for spherical loading achieved by using boundary condition inherited from the analytical model without multi-point constraints on inner ∂B_a and outer ∂B_b boundaries of the unit cell depicted in Fig. 5.1. b) Time evolution of the ratio a^2/b^2 measured at ∂B_0 and ∂B_l when multiple kinematic constraints are disregarded. The evolution of the porosity obtained from the analytical approach, which will be shown to coincide with the FEM results when multiple kinematic constraints are imposed, is superimposed.

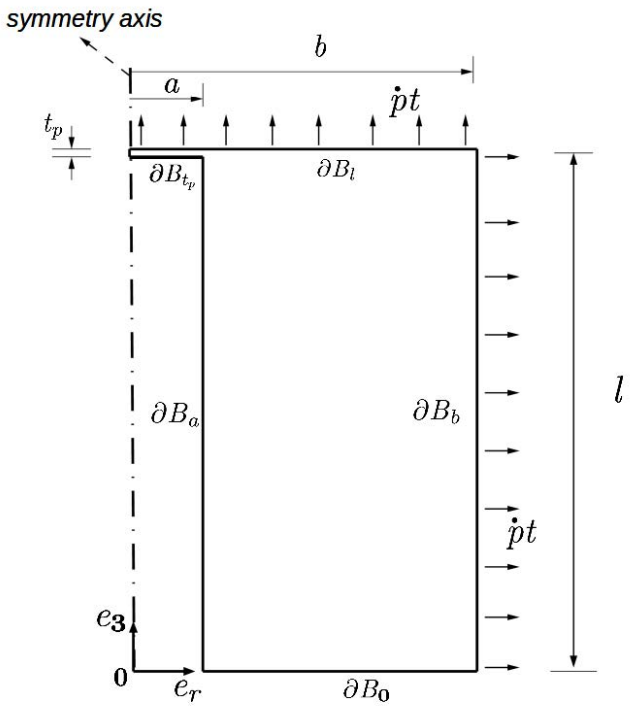

Figure 5.5: Closed cylindrical unit cell of length l, inner radius a and external radius b having a thin plate of thickness t_p on the top. CAX4R elements with initial size of 20μm x40μm are used.

stress tensor component at the top layer is immediate. This strategy however requires additional kinematic constraints in order to prevent the unit cell from excessive and unexpected distortion. Specifically, the inner surfaces identified by ∂B_a and ∂B_{t_p} on Fig. 5.5 as well as the outer surfaces ∂B_l and ∂B_b remain planar. In addition, the condition of symmetry on ∂B_0 still prevails. The lateral stress $\dot{p}t$ is prescribed according to Eq (5.3), and the axial stress $\Sigma_{33} = \dot{p}t$ is imposed at the top surface. The void boundary is stress free.

To show the necessity of above constraints on ∂B_a, ∂B_{t_p}, ∂B_l and ∂B_b to remain planar, FEM calculations have been conducted by removing the kinematic constraints. Fig. 5.6a illustrates the irregular distortion due to the lack of multi-point constraint on the outer boundary ∂B_b of the closed unit cell of Fig. 5.5. Fig. 5.6b shows the unexpected distortion of the top plate because of the removal of multi-point constraint on the top boundary ∂B_l of the closed unit cell. Similarly the unit cell is unable to remain cylindrical during the deformation stage when the

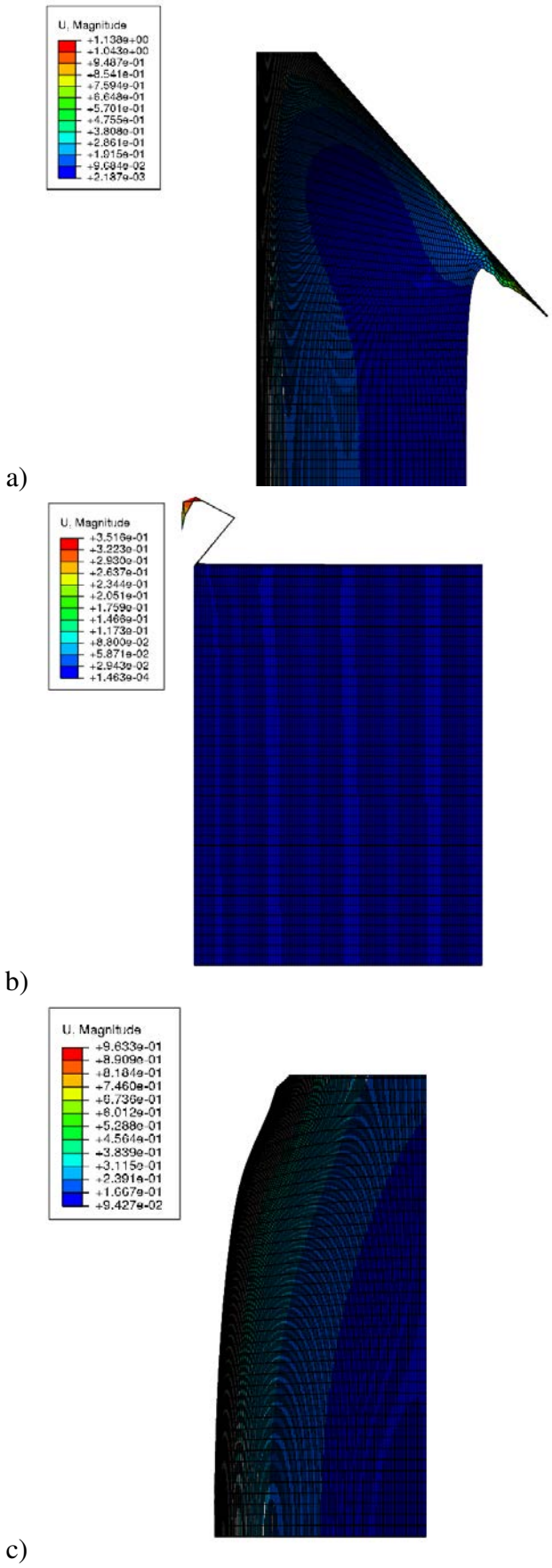

Figure 5.6: FEM calculations for hydrostatic loading achieved by applying stress on the top surface and lateral direction of the closed unit cell of Fig. 5.5. a) without multi-point constraint on the outer boundary ∂B_b, b) without multi-point constraint on the top boundary ∂B_l and c) without multi-point constraint on the inner boundaries ∂B_l and ∂B_{t_p}.

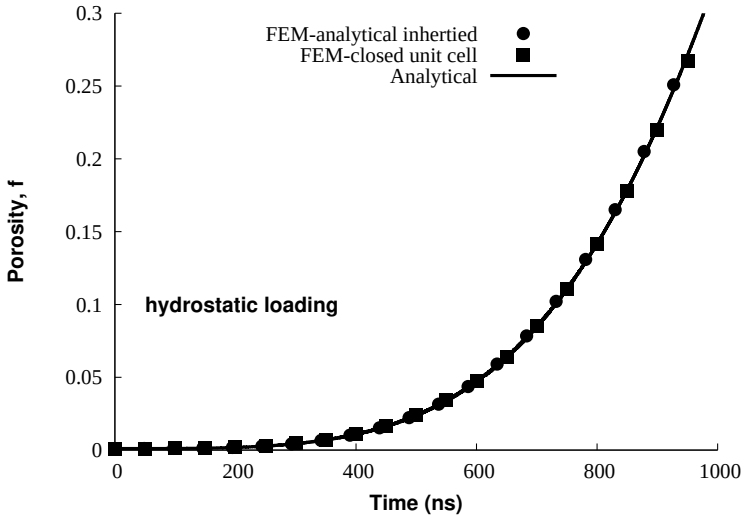

Figure 5.7: Time evolution of the porosity for a porous medium with cylindrical void under spherical loading with $\dot{p}$ =10MPa/ns and considering the reference material of Table 4.1 with l_0 =2000μm. Comparison between analytical results and FEM calculations. The approach based on the analytically inherited velocity field and the closed unit cell give comparable results.

multi-point constraints on the inner boundaries (∂B_a and ∂B_{t_p}) are removed, Fig. 5.6c. The above case studies prove the necessity of multi-point constraints on the boundaries (∂B_a, ∂B_{t_p}, ∂B_l and ∂B_b) of the closed unit cell, so that predictions of FEM calculation and of the model can be compared.

5.3.3 Validation on the reference case

The two strategies described in previous sections, are compared against analytical results of Fig. 4.5 obtained for $\dot{p}$ =10MPa/ns. The half length of the void is l_0 =2000μm, other material parameters are listed in Table 4.1. In our finite element calculation using the closed unit cell of Fig. 5.5, the thickness of the top layer is t_p=10 μm. It was checked that a smaller value do not affect the response of the unit cell. Fig. 5.7 shows the evolution of the porosity versus time and serves at verifying the analytical approach. It illustrates also the equivalence between the two finite element models of sections 5.3.1 and 5.3.2.

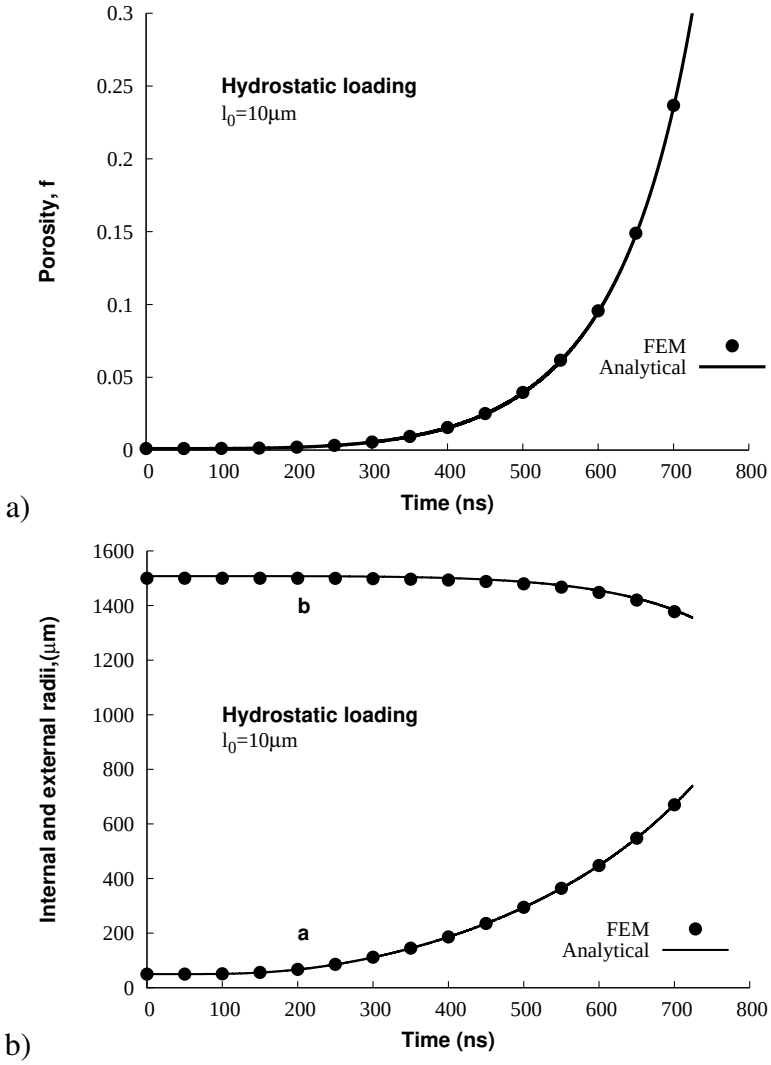

Figure 5.8: FEM calculations and analytical results for thin cylinder (l_0=10μm) subjected to spherical loading, a) Porosity versus time and b) Internal and external radii vs time. The stress rate is $\dot{p}$ =10MPa/ns. The reference material with parameters listed in Table 4.1 is considered. The FEM calculations and analytical results give good agreement.

5.3.4 Thin cylinder, l_0=10μm

Here we validate the analytical results obtained when considering a thin cylinder with initial half length l_0=10μm. This case has been discussed in section 4.4 (Fig. 4.5 and Fig. 4.6, $l_0 \rightarrow$0). The hydrostatic loading is achieved using the strategy developed in section 5.3.1 (boundary condition inherited from the analytical velocity). As revealed in section 4.4, for thin cylinder under spherical loading the porosity growth results from a decrease of external radius b and an

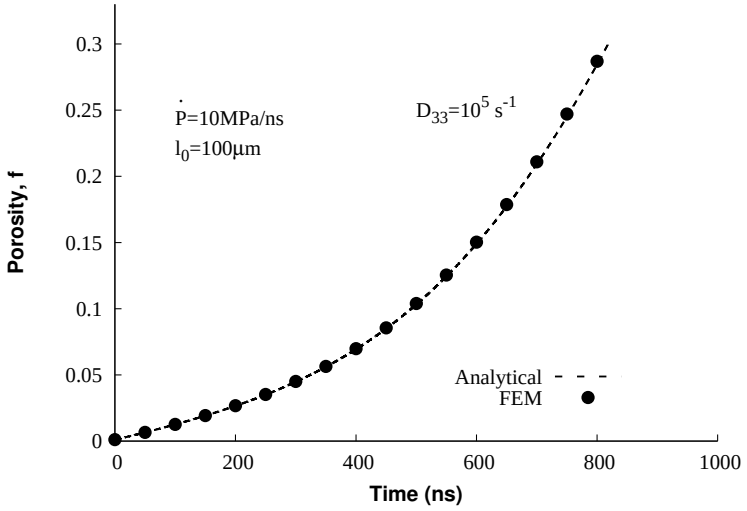

Figure 5.9: Time evolution of porosity validation of analytical results with FEM calculation. A constant strain rate is imposed on the top surface ∂B_l D_{33}=$10^5 s^{-1}$ and a prescribed stress Σ_{11}=Σ_{22}=$\dot{p}t$ is applied on ∂B_b. The initial length is l_0 =100μm, other material parameters listed in Table 4.1 are considered. The FEM calculation and analytical results are in good agreement.

increase of internal radius a. Here we compare the evolution of the porosity and damage growth mechanism predicted by the analytical approach and the results obtained from FEM. Fig. 5.8 illustrates the perfect match between the two approaches (FEM and analytical) regarding the porosity growth (Fig. 5.8a) and the evolution of the internal and external void radii (Fig. 5.8b).

5.4 Additional loading cases

Additional loading cases considered in the thesis are verified against numerical results obtained using the axisymmetric unit cell of Fig. 5.1.

5.4.1 Imposed axial strain rate (D_{33}=constant) with combined stress imposed on the lateral surface

In this section, we validate the analytical results obtained when the loading path consists of a homogeneous stress prescribed on the lateral surface, Σ_{11}=Σ_{22}=$\dot{p}t$, while a constant strain rate D_{33} is imposed in the longitudinal direction. In section 4.5 (Fig. 4.14a) the porosity evolution

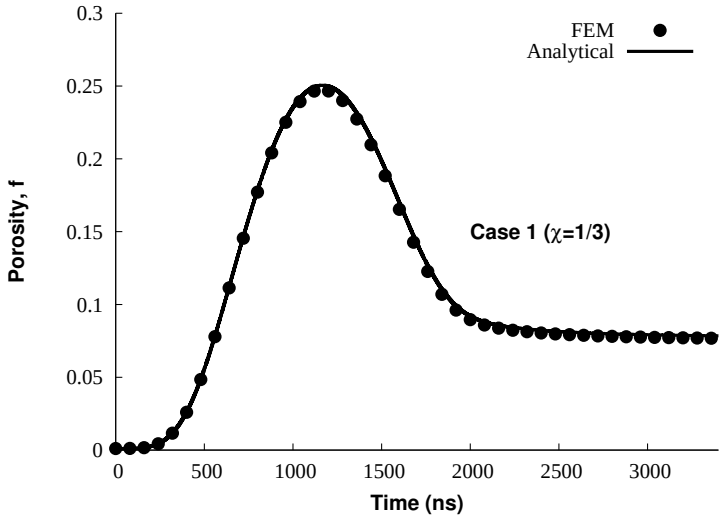

Figure 5.10: Time evolution of porosity comparison of FEM calculations and analytical result for uniaxial stress loading configuration: Σ_{11}=Σ_{22}=0 and Σ_{33}=$\dot{p}t$ (Case 1, χ=1/3). The stress rate is $\dot{p}$=10MPa/ns. Parameters for the reference material are listed in Table 4.1 with l_0=2000μm and ρ=270Kg/m^3.

has been illustrated for D_{33} ranging from 0 to $10^6 s^{-1}$ under stress rate $\dot{p}$=10MPa/ns. The case where D_{33}=$10^5 s^{-1}$ is selected here considering the material parameters of Table 4.1 with initial void half length, $l_0 = 100\mu m$. Fig 5.9 clearly provides a validation of the analytical modeling from the very good comparison with the finite element calculations.

5.4.2 Uniaxial loading: Case 1, χ=1/3

As explained in section 4.5, Case 1 corresponds to Σ_{11}=Σ_{22}=0, Σ_{33}=$\dot{p}t$ and reflects the uniaxial stress loading configuration for which the triaxiality $\chi = \frac{\Sigma_m}{\Sigma_{eq}}$ is equal to $1/3$. Numerical results are obtained using the axisymmetric unit cell of Fig. 5.1, therefore, the boundary condition $\Sigma_{33} = \dot{p}t$ is replaced by a kinematic velocity field derived from the analytical model.

We have chosen a matrix mass density of $\rho = 270 kg/m^3$ for validation with FEM calculations. The initial length is l_0=2000μm and the loading rate is $\dot{p}$=10MPa/ns, see also Fig. 4.12a. Other material parameters of Table 4.1 are considered. This case is particularly selected because as observed in Fig. 4.12a, after reaching a maximum porosity (less than the critical porosity

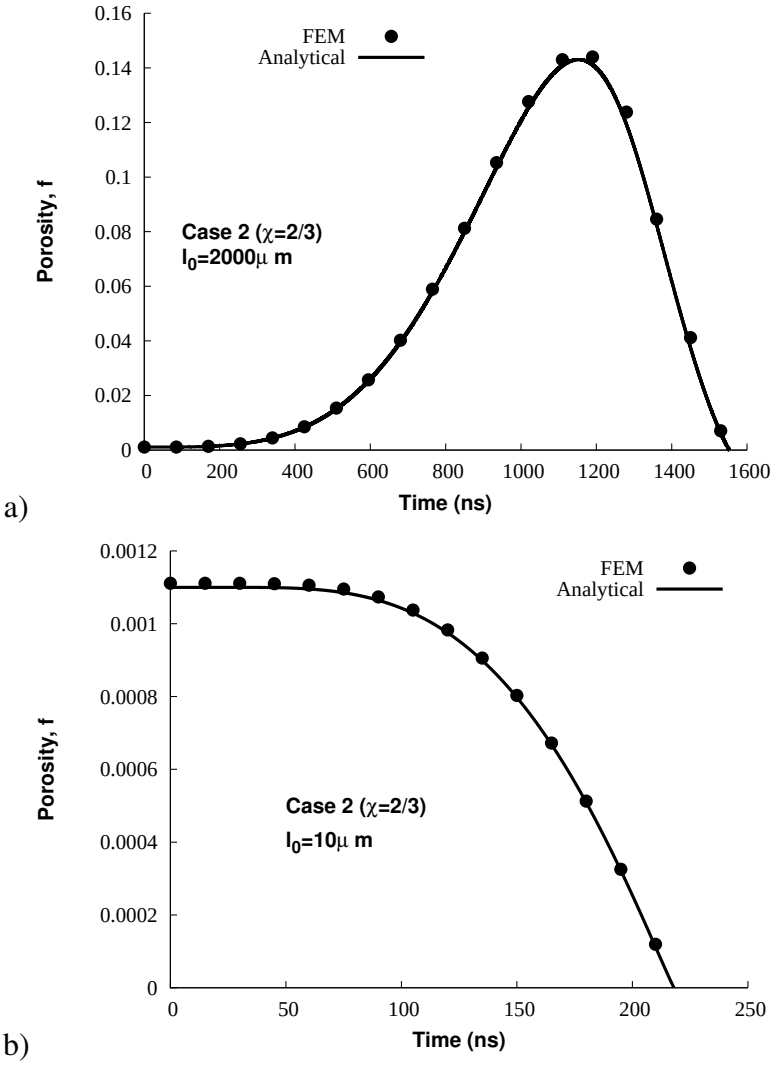

Figure 5.11: FEM calculations and analytical result comparison for loading case Σ_{11}=Σ_{22}=$\dot{p}t$ and Σ_{33}=0 (case 2, χ=2/3) a) l_0=2000μm b) l_0=10μm. The stress rate is $\dot{p}$=10MPa/ns. The reference material with parameters listed in Table 4.1 is considered.

f_c=0.3 for which fracture is assumed to occur), the porosity falls and reaches a stabilized value (a plateau is observed). Fig. 5.10 illustrates this peculiar response under uniaxial loading and very good agreement between FEM and analytical results.

5.4.3 Biaxial loading: Case 2, χ=2/3

In this section, we consider the loading Case 2 and two values of the initial length: l_0=10μm and 2000μm, see section 4.5. Recall that Case 2 corresponds to a biaxial loading where Σ_{11}=Σ_{22}=$\dot{p}t$, Σ_{33}=0. The corresponding triaxiality is 2/3. In that case, the unit cell is expand-

ing in the radial direction. Under such loading configuration, the void is shown to collapse for the two values of l_0, considered in Figs 4.9a and 4.9b. Figs 5.11a and 5.11b illustrate the validation of the two above analytical cases with FEM calculations. The model provides accurate prediction since FEM and analytical model results coincide. In particular, when l_0=2000μm (Fig. 5.11a), the porosity is first increasing up to 0.1415 obtained from FEM, while a very close value of 0.14 is revealed with the analytical approach.

5.5 Influence of the elastic properties

In all examples investigated above, a large value of the Young modulus E=6300GPa and of the Poisson ratio ν=0.499 has been adopted. In this section, we discuss the effect of elastic properties by varying E and v, considering still the axisymmetric model of Fig. 5.1. Again, plane strain and hydrostatic loading conditions are selected with material parameters listed in Table 4.1. To illustrate the effect of elastic compressibility of the matrix in FEM calculation, two values of the Poisson ratio have been tested (ν=0.33 and ν=0.499). So FEM calculations are carried out for (i) E=70GPa and ν=0.33 (representative of aluminium) and (ii) E=70GPa and ν=0.499 (to approach incompressibility condition). Fig. 5.12 illustrates the time evolution of the porosity obtained from numerical simulations considering both sets of elastic constants compared to the analytical result. It is clear that the FEM calculation with E=70GPa and ν=0.499 shows very close agreement with the analytical model for plane strain (Fig. 5.12a) and hydrostatic loadings (Fig. 5.12b). This figure has motivated our choice of adopting ν=0.499 for all loading cases.

The Young modulus is now varied, adopting the value of $\nu = 0.499$. Fig. 5.13 shows the FEM results for E=0.7, 6.3, 70 and 6300GPa. Plane strain loading (Fig. 5.13a-b) corresponding to results of Fig. 5.2 and hydrostatic loading (Fig. 5.13c) corresponding to results of Fig. 5.7 are tested. The FEM calculations show that the variation of the Young modulus has only a slight

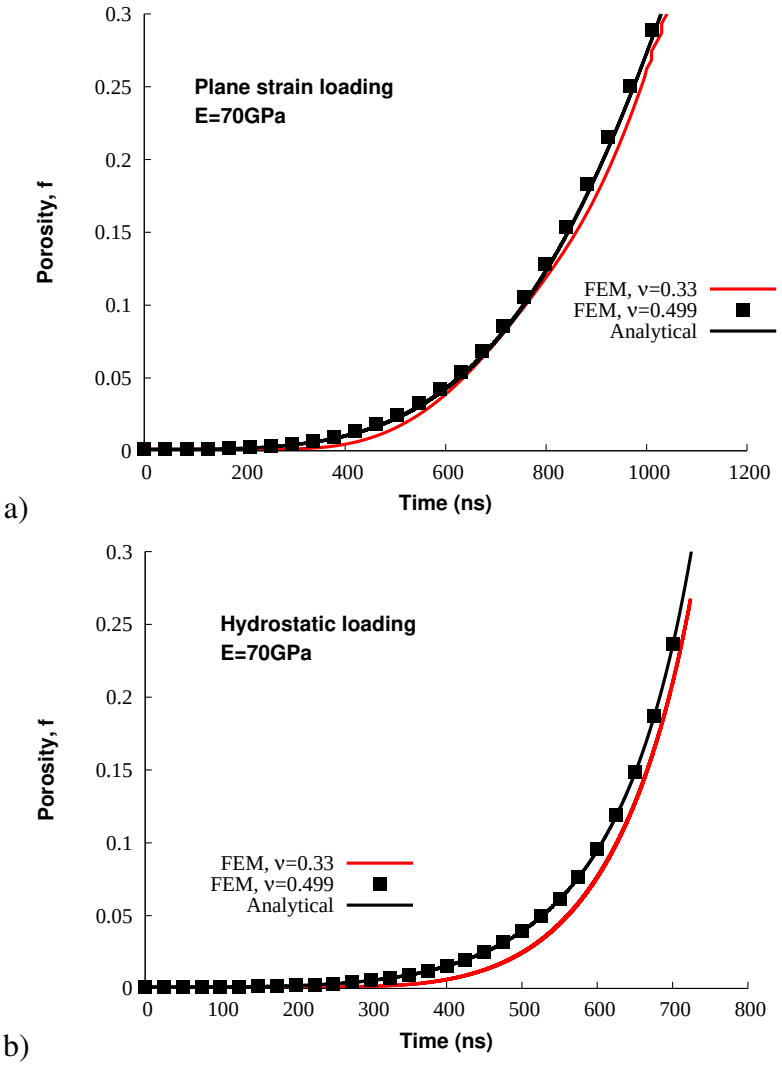

Figure 5.12: Time evolution of the porosity. FEM calculations for two Poisson's ratio=0.499 and 0.33 with Young's modulus E=70GPa under a) plane strain loading b) hydrostatic loading. Model predictions are also displayed. The loading rate is $\dot{p}$ =10MPa/ns. The material parameters listed in Table 4.1 are considered.

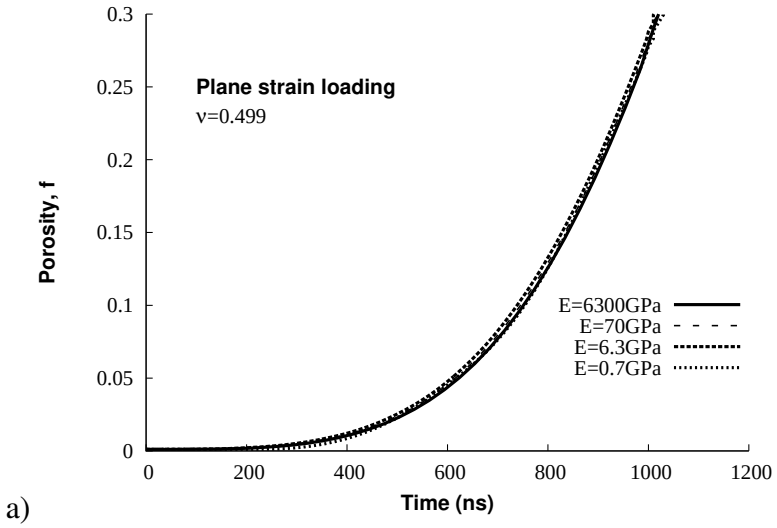

a)

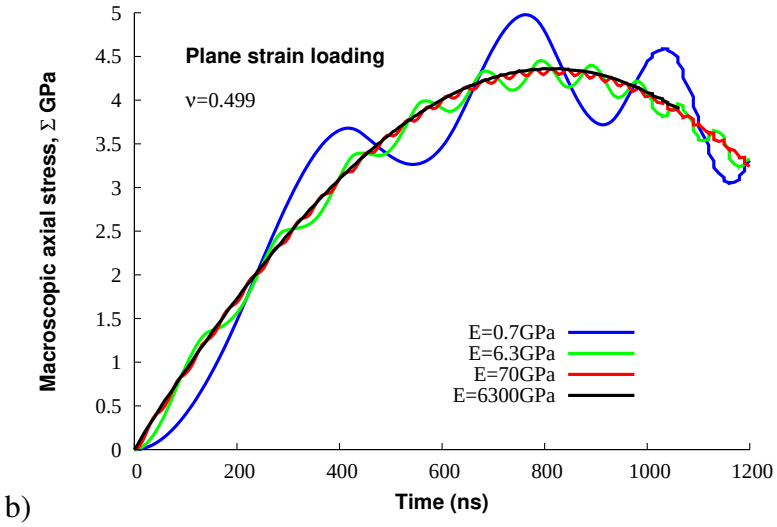

b)

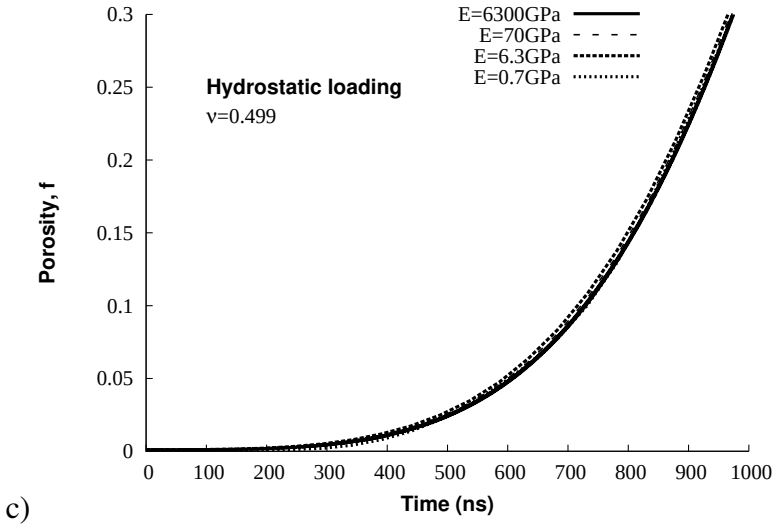

c)

Figure 5.13: Comparison of FEM calculations for various Young modulus, E=0.7, 6.3, 70 and 6300GPa under a) Plane strain loading b) Hydrostatic loading. The Poisson ratio is 0.499. Time evolution of the porosity for $\dot{p}$ =10MPa/ns. The material parameters listed in Table 4.1 is considered.

effect on the porosity evolution as depicted in Fig. 5.13a) and c). The perfect match between the analytical prediction and FEM calculations are observed for the highest value E=6300GPa. It has been checked that a further increase in Young modulus gives the same response as in the case E=6300GPa. More important is the corresponding evolution of the macroscopic axial stress Σ_{33}, see Fig. 5.13b. It is observed that the macroscopic axial stress shows some oscillations when E$\leq$70GPa. In fact, one can correlate the time period of oscillations to the time for an elastic wave to go back and forth from the outer to the inner boundaries of the cylindrical cell. In addition, since ν=0.499 is kept fixed for all calculations, the elastic wave speed is proportionnal to the Young modulus. As a consequence:

- when E is multiplied by approx. 10 (from 0.7 to 6.3), the number of oscillations is multiplied by approx. $\sqrt{10}$.

- When E is multiplied by 100 (from 0.7 to 70), the number is multiplied by 10.

In the case where E=6300GPa, the oscillation is vanished until the porosity reaches 0.3. At the end, to be consistent with the analytical results and to avoid oscillations, we have selected the largest Young modulus value, E=6300GPa for all loading cases in this thesis.

Chapter 6

Conclusion and perspectives

The objective of this thesis was to propose a model of damage by growth of cavities for dynamic loading. The porous materials considered in this work contain parallel cylindrical voids. These voids are representative of perforated structures or honeycomb architectural materials. The goal was to highlight the influence of two characteristic lengthscales of the unit cell (radius and length).

The results obtained from the model were checked by comparison with numerical simulations performed on finite element models developed in the PhD. Many loading cases were considered and new results were presented in the thesis. In particular, during a plane strain loading, we show that the axial stress decreases while the stresses in the plane direction continue to increase. This result reflecting that the stress required to maintain a porous structure at its initial length is reduced due to micro-inertial effects, can be used to design elements for machines for dynamic testing. The case where thin structures are subjected to dynamic spherical loading revealed unexpected behavior. The damage increases by increasing the void radius together with the reduction of the external radius. This trend can only be attributed due to micro-inertia.

In addition to plane strain and hydrostatic conditions, the model has been tested for additional loading configurations to reveal particular tendencies. For example, the void collapses during rapid biaxial expansion. In dynamic traction after an initial increase, the porosity seems to saturate when the voids are long enough and the inertial effects are significant.

The PhD work opens new perspectives. We will mention only some of them. First of all, the matrix was considered here as rigid perfectly plastic. The stabilizing effects related to dynamic loading in our approach results only from the inertia effects related to the size of the voids. The literature has shown that viscous effects can play an important role in the evolution of dynamic damage. Therefore it is expected that for real material, porosity evolution depends on the combined influence of viscous and micro-inertial effects. The first continuation of this work could be to include strain rate sensitivity in the rheological response of the matrix. It is important to note that this will lead to an adjustment in the quasi-static contribution (i.e. independent of micro-inertia effects) and will not affect the analytical expressions of the inertial contribution that are obtained in this work. After taking into account viscous effects in the extended approach, it seems appropriate to us to implement the model for comparison purposes to experimental tests conducted on ductile materials whose dynamic behavior of the matrix would have to be identified. The effect of hardening and thermal softening could be also of interest.

In our approach, the adopted RVE and associated velocity fields are defined for a hollow cylinder. This elementary configuration allows us to highlight the differential micro-inertia effects between the macroscopic contribution in the plane, and in the axial direction of the cylinder. An interesting way to extend our model is to consider cylindrical voids fully embedded in the matrix. Based on approaches from the literature, we aim to adopt an elementary unit cell domain containing a void surrounded by deformable matrix, similar to the RVE considered by Morin et al. [27].

Finally, the results obtained at LEM3 for spherical voids showed the significant importance of void size distribution parameters on the dynamic response of porous materials. It could also be interesting to consider distribution in size (a) and shape ratio (l/a) on the dynamic response of a porous structure containing a heterogeneous population of cylindrical voids.

Appendix A

Formulation of the macroscopic dynamic stress tensor, $\boldsymbol{\Sigma}^{\mathrm{dyn}}$.

A.1 General formulation

The macroscopic dynamic stress tensor $\boldsymbol{\Sigma}^{\mathrm{dyn}}$ is evaluated in this section with use of the following kinematic boundary condition:

$$\boldsymbol{v} = \mathbf{L} \cdot \boldsymbol{x} \quad \text{on } \partial V\,, \tag{A.1}$$

with $\boldsymbol{x}$ being the position vector. $\mathbf{L}$ is the macroscopic velocity gradient tensor, related to the macroscopic strain rate $\mathbf{D}$ and spin tensor $\boldsymbol{\Omega}$ by the following relationships:

$$\mathbf{D} = \frac{\mathbf{L} + {}^{\mathrm{t}}\mathbf{L}}{2}\,, \quad \boldsymbol{\Omega} = \frac{\mathbf{L} - {}^{\mathrm{t}}\mathbf{L}}{2}\,. \tag{A.2}$$

With the boundary condition (A.1), Eqs (2.27) and (2.32) become:

$$\boldsymbol{\Sigma} : {}^{\mathrm{t}}\mathbf{L} = \langle \boldsymbol{\sigma} : \mathbf{d} \rangle + \frac{1}{2} \langle \rho \frac{\mathrm{d}|\mathbf{v}|^{\mathbf{2}}}{\mathrm{d}t} \rangle \,, \tag{A.3}$$

$$\boldsymbol{\Sigma} : {}^{\mathrm{t}}\delta\mathbf{L} = \frac{\partial \langle \hat{\Phi} \rangle}{\partial \mathbf{D}} : \delta\mathbf{D} + \boldsymbol{\Sigma}^{\mathrm{dyn}} : {}^{\mathrm{t}}\delta\mathbf{L} \,, \tag{A.4}$$

with

$$\boldsymbol{\Sigma}^{\mathrm{dyn}} : {}^{\mathrm{t}}\delta\mathbf{L} = \langle \rho\boldsymbol{\gamma} \cdot \delta\mathbf{v} \rangle = \frac{1}{|V|} \int_V \rho\boldsymbol{\gamma}\delta\mathbf{v} dV \,. \tag{A.5}$$

More information can be found in Molinari and Mercier [26].

The dynamic stress tensor $\boldsymbol{\Sigma}^{\mathrm{dyn}}$ is evaluated considering that the porous material is represented by the hollow cylinder and that the approximate velocity field is of the form:

$$\boldsymbol{v} = \hat{\mathbf{L}} \cdot \boldsymbol{x} + B\tilde{\boldsymbol{x}} \tag{A.6}$$

where $B = \frac{3\mathbf{L}_m}{2} \left(\frac{b}{r}\right)^2 - \frac{L_{33}}{2}$ and $\hat{\mathbf{L}}$ is defined as in Eq (2.10). The adopted velocity field satisfies the kinematic condition (A.1) together with the matrix incompressibility condition. From Eq (A.6), the variation of the velocity $\delta\mathbf{v}$ due to the change $\delta\mathbf{L}$ of $\mathbf{L}$ at the boundary and the acceleration are:

$$\delta\boldsymbol{v} = \delta\hat{\mathbf{L}} \cdot \boldsymbol{x} + \delta B\tilde{\boldsymbol{x}} \,, \tag{A.7}$$

$$\boldsymbol{\gamma} = \dot{\hat{\mathbf{L}}} \cdot \boldsymbol{x} + \hat{\mathbf{L}} \cdot \boldsymbol{v} + \dot{B}\tilde{\boldsymbol{x}} + B\tilde{\boldsymbol{v}} \,, \tag{A.8}$$

where $\tilde{\boldsymbol{v}} = v_1\mathbf{e}_1 + v_2\mathbf{e}_2$. In Eq (A.8), the term $\dot{B}$ is given by:

$$\dot{B} = \frac{3}{2}\left(\frac{b}{r}\right)^2\left[\dot{L}_m + 3{L_m}^2 - 3\left(\frac{b}{r}\right)^2{L_m}^2\right] - \frac{\dot{L}_{33}}{2} \tag{A.9}$$

Combining Eqs (A.6-A.8), the integral term $I = \frac{1}{|V|}\int_V \rho\boldsymbol{\gamma}\delta\mathbf{v}$ of Eq (A.5) can be written as:

$$I = \frac{1}{|V|}\int_V \rho\boldsymbol{\gamma}\delta\boldsymbol{v}dV = \frac{1}{|V|}\int_V \rho(\boldsymbol{x}\cdot{}^t\dot{\hat{\mathbf{L}}}\cdot\delta\hat{\mathbf{L}}\cdot\boldsymbol{x} + \boldsymbol{v}\cdot{}^t\hat{\mathbf{L}}\cdot\delta\hat{\mathbf{L}}\cdot\boldsymbol{x} + \dot{B}\delta B\tilde{\boldsymbol{x}}\cdot\tilde{\boldsymbol{x}} + B\delta B\tilde{\boldsymbol{v}}\cdot\tilde{\boldsymbol{x}} + \dot{B}\tilde{\boldsymbol{x}}\cdot\delta\hat{\mathbf{L}}\cdot\boldsymbol{x} + B\tilde{\boldsymbol{v}}\cdot\delta\hat{\mathbf{L}}\cdot\boldsymbol{x} + \delta B\tilde{\boldsymbol{x}}\cdot\dot{\hat{\mathbf{L}}}\cdot\boldsymbol{x} + \delta B\tilde{\boldsymbol{x}}\cdot\hat{\mathbf{L}}\cdot\boldsymbol{v})dV \tag{A.10}$$

The volume $|V|$ of the RVE is $2l\pi b^2$. Note that particles are present only for $a \leq r \leq b$. After some calculations leading to an explicit relation for $I = \frac{1}{|V|}\int_V \rho\boldsymbol{\gamma}\delta\mathbf{v}dV$, using the following decomposition of $\delta\mathbf{L}$:

$$\delta\mathbf{L} = \delta\mathbf{L}_{(12)} + \delta\mathbf{L}_{(x3)} + \delta\mathbf{L}_{(3x)} + \delta L_{33}\mathbf{e}_3\otimes\mathbf{e}_3 \tag{A.11}$$

with

$$\delta\mathbf{L}_{(12)} = \begin{bmatrix}\delta L_{11} & \delta L_{12} & 0\\ \delta L_{21} & \delta L_{22} & 0\\ 0 & 0 & 0\end{bmatrix}\ \delta\mathbf{L}_{(x3)} = \begin{bmatrix}0 & 0 & \delta L_{13}\\ 0 & 0 & \delta L_{23}\\ 0 & 0 & 0\end{bmatrix}\ \delta\mathbf{L}_{(3x)} = \begin{bmatrix}0 & 0 & 0\\ 0 & 0 & 0\\ \delta L_{31} & \delta L_{32} & 0\end{bmatrix} \tag{A.12}$$

I is written as:

$$
\begin{aligned}
I = \frac{\rho a^2}{4}\Bigg\{ & \left(f^{-1}-f\right)\left(\dot{\hat{\mathbf{L}}}+\hat{\mathbf{C}}-D_{33}\,\hat{\mathbf{L}}\right)+6\left(f^{-1}-1\right)D_{\mathrm{m}}\,\hat{\mathbf{L}} \\
& +\Bigg[\left(f^{-1}-1\right)\left(C_{11}+C_{22}-\dot{D}_{33}+\frac{D_{33}^2}{2}\right)-\frac{9}{2}\left(f^{-2}-f^{-1}\right)D_{\mathrm{m}}^2 \\
& +3f^{-1}\ln\left(\frac{1}{f}\right)\left(\dot{D}_{\mathrm{m}}+3D_{\mathrm{m}}^2-D_{\mathrm{m}}D_{33}\right)\Bigg]\mathbf{I}\Bigg\} : {}^{t}\delta\mathbf{L}_{(12)} \\
& +\frac{\rho a^2}{4}\left[\left(f^{-1}-f\right)\left(\dot{\hat{\mathbf{L}}}+\hat{\mathbf{C}}-\frac{D_{33}}{2}\,\hat{\mathbf{L}}\right)+3\left(f^{-1}-1\right)D_{\mathrm{m}}\,\hat{\mathbf{L}}\right] : {}^{t}\delta\mathbf{L}_{(3\mathrm{x})} \\
& +\frac{\rho l^2}{3}\left[(1-f)\left(\dot{\hat{\mathbf{L}}}+\hat{\mathbf{C}}-\frac{D_{33}}{2}\,\hat{\mathbf{L}}\right)+\frac{3}{2}\ln\left(\frac{1}{f}\right)D_{\mathrm{m}}\,\hat{\mathbf{L}}\right] : {}^{t}\delta\mathbf{L}_{(\mathrm{x}3)} \\
& +\Bigg\{\frac{\rho a^2}{4}\Bigg[\left(f^{-1}-f\right)\left(\frac{\dot{D}_{33}}{2}-\frac{D_{33}^2}{4}-\frac{C_{11}+C_{22}}{2}\right)-\frac{9}{2}\left(f^{-2}-f^{-1}\right)D_{\mathrm{m}}^2 \\
& +\left(f^{-1}-1\right)\left(C_{11}+C_{22}+3D_{\mathrm{m}}D_{33}+\frac{D_{33}^2}{2}-9D_{\mathrm{m}}^2-\dot{D}_{33}-3\dot{D}_{\mathrm{m}}\right) \\
& +3f^{-1}\ln\left(\frac{1}{f}\right)\left(\dot{D}_{\mathrm{m}}+\frac{9}{2}D_{\mathrm{m}}^2-D_{\mathrm{m}}D_{33}\right)\Bigg]+\frac{\rho l^2}{3}\left(1-f\right)\left(\dot{D}_{33}+C_{33}\right)\Bigg\}\delta L_{33}
\end{aligned}
\tag{A.13}
$$

where

$$
\hat{\mathbf{L}}=\begin{bmatrix}\frac{L_{11}-L_{22}}{2} & L_{12} & L_{13}\\ L_{21} & \frac{L_{22}-L_{11}}{2} & L_{23}\\ L_{31} & L_{32} & L_{33}\end{bmatrix}, \tag{A.14}
$$

$\mathbf{C}=\hat{\mathbf{L}}\cdot\hat{\mathbf{L}}$.

$$
\hat{\mathbf{C}}=\begin{bmatrix}\frac{C_{11}-C_{22}}{2} & C_{12} & C_{13}\\ C_{21} & \frac{C_{22}-C_{11}}{2} & C_{23}\\ C_{31} & C_{32} & C_{33}\end{bmatrix}. \tag{A.15}
$$

By identification (the components of $\delta\mathbf{L}$, being independent terms), the dynamic macroscopic

stress tensor Σ^{dyn} is obtained from Eq (A.5):

$$\Sigma_{11}^{\text{dyn}} = \frac{\rho a^2}{4}\Bigg[\left(f^{-1}-f\right)\left(\dot{\hat{D}}_{11}+\hat{C}_{11}-D_{33}\hat{D}_{11}\right)-\frac{9}{2}\left(f^{-2}-f^{-1}\right){D_{\text{m}}}^2 + 3f^{-1}\ln\left(\frac{1}{f}\right)\left(\dot{D}_{\text{m}}+3{D_{\text{m}}}^2-D_{\text{m}}D_{33}\right) + \left(f^{-1}-1\right)\left(\frac{{D_{33}}^2}{2}-\dot{D}_{33}+C_{11}+C_{22}+6D_{\text{m}}\hat{D}_{11}\right)\Bigg] \quad \text{(A.16)}$$

$$\Sigma_{22}^{\text{dyn}} = \frac{\rho a^2}{4}\Bigg[\left(f^{-1}-f\right)\left(\dot{\hat{D}}_{22}+\hat{C}_{22}-D_{33}\hat{D}_{22}\right)-\frac{9}{2}\left(f^{-2}-f^{-1}\right){D_{\text{m}}}^2 + 3f^{-1}\ln\left(\frac{1}{f}\right)\left(\dot{D}_{\text{m}}+3{D_{\text{m}}}^2-D_{\text{m}}D_{33}\right) + \left(f^{-1}-1\right)\left(\frac{{D_{33}}^2}{2}-\dot{D}_{33}+C_{11}+C_{22}+6D_{\text{m}}\hat{D}_{22}\right)\Bigg] \quad \text{(A.17)}$$

$$\Sigma_{33}^{\text{dyn}} = \frac{\rho a^2}{4}\Bigg[\left(f^{-1}-f\right)\left(\frac{\dot{D}_{33}}{2}-\frac{D_{33}^2}{4}-\frac{C_{11}+C_{22}}{2}\right)-\frac{9}{2}\left(f^{-2}-f^{-1}\right)D_{\text{m}}^2 + \left(f^{-1}-1\right)\left(C_{11}+C_{22}+3D_{\text{m}}D_{33}+\frac{D_{33}^2}{2}-9D_{\text{m}}^2-\dot{D}_{33}-3\dot{D}_{\text{m}}\right) + 3f^{-1}\ln\left(\frac{1}{f}\right)\left(\dot{D}_{\text{m}}+\frac{9}{2}D_{\text{m}}^2-D_{\text{m}}D_{33}\right)\Bigg] + \frac{\rho l^2}{3}\left(1-f\right)\left(\dot{D}_{33}+C_{33}\right) \quad \text{(A.18)}$$

$$\Sigma_{12}^{\text{dyn}} = \frac{\rho a^2}{4}\left[\left(f^{-1}-f\right)\left(\dot{L}_{12}+C_{12}-D_{33}L_{12}\right)+6\left(f^{-1}-1\right)D_{\text{m}}L_{12}\right] \quad \text{(A.19)}$$

$$\Sigma_{21}^{\text{dyn}} = \frac{\rho a^2}{4}\left[\left(f^{-1}-f\right)\left(\dot{L}_{21}+C_{21}-D_{33}L_{21}\right)+6\left(f^{-1}-1\right)D_{\text{m}}L_{21}\right] \quad \text{(A.20)}$$

$$\Sigma_{13}^{\text{dyn}} = \frac{\rho l^2}{3}\left[(1-f)\left(\dot{L}_{13}+C_{13}-\frac{D_{33}}{2}L_{13}\right)+\frac{3}{2}\ln\left(\frac{1}{f}\right)D_{\text{m}}L_{13}\right] \quad \text{(A.21)}$$

$$\Sigma_{23}^{\text{dyn}} = \frac{\rho l^2}{3}\left[(1-f)\left(\dot{L}_{23}+C_{23}-\frac{D_{33}}{2}L_{23}\right)+\frac{3}{2}\ln\left(\frac{1}{f}\right)D_{\text{m}}L_{23}\right] \quad \text{(A.22)}$$

$$\Sigma_{31}^{\text{dyn}} = \frac{\rho a^2}{4}\left[\left(f^{-1}-f\right)\left(\dot{L}_{31}+C_{31}-\frac{D_{33}}{2}L_{31}\right)+3\left(f^{-1}-1\right)D_{\text{m}}L_{31}\right] \quad \text{(A.23)}$$

$$\Sigma_{32}^{\text{dyn}} = \frac{\rho a^2}{4}\left[\left(f^{-1}-f\right)\left(\dot{L}_{32}+C_{32}-\frac{D_{33}}{2}L_{32}\right)+3\left(f^{-1}-1\right)D_{\text{m}}L_{32}\right] \quad \text{(A.24)}$$

Note that $L_{11} = D_{11}$, $L_{22} = D_{22}$, $L_{33} = D_{33}$ and $L_m = D_m = (D_{11}+D_{22}+D_{33})/3$. The dynamic stress tensor reveals particular aspects that are commented in the main text, see section 3.2.

A.2 Case where $\boldsymbol{\Omega} = \mathbf{0}$

The case where $\mathbf{L}$ is symmetric, i.e. $\mathbf{L} = \mathbf{D}$, corresponds to the velocity field (3.15) of section 3.1. The dynamic stress tensor components Σ_{11}^{dyn}, Σ_{22}^{dyn} and Σ_{33}^{dyn} are still given by Eqs (A.16), (A.17) and (A.18) respectively. Since $\mathbf{C} = \hat{\mathbf{D}}\cdot\hat{\mathbf{D}}$ in this case, and thus is symmetric, the other components are obtained directly from Eqs (A.19-A.24), leading to:

$$\Sigma_{12}^{\text{dyn}} = \Sigma_{21}^{\text{dyn}} = \frac{\rho a^2}{4}\left[\left(f^{-1}-f\right)\left(\dot{D}_{12}+C_{12}-D_{33}D_{12}\right)+6\left(f^{-1}-1\right)D_{\text{m}}D_{12}\right] \quad \text{(A.25)}$$

$$\Sigma_{13}^{\text{dyn}} = \frac{\rho l^2}{3}\left[(1-f)\left(\dot{D}_{13}+C_{13}-\frac{D_{33}}{2}D_{13}\right)+\frac{3}{2}\ln\left(\frac{1}{f}\right)D_{\text{m}}D_{13}\right] \quad \text{(A.26)}$$

$$\Sigma_{23}^{\text{dyn}} = \frac{\rho l^2}{3}\left[(1-f)\left(\dot{D}_{23}+C_{23}-\frac{D_{33}}{2}D_{23}\right)+\frac{3}{2}\ln\left(\frac{1}{f}\right)D_{\text{m}}D_{23}\right] \quad \text{(A.27)}$$

$$\Sigma_{31}^{\text{dyn}} = \frac{\rho a^2}{4}\left[\left(f^{-1}-f\right)\left(\dot{D}_{13}+C_{13}-\frac{D_{33}}{2}D_{13}\right)+3\left(f^{-1}-1\right)D_{\text{m}}D_{13}\right] \quad \text{(A.28)}$$

$$\Sigma_{32}^{\text{dyn}} = \frac{\rho a^2}{4}\left[\left(f^{-1}-f\right)\left(\dot{D}_{23}+C_{23}-\frac{D_{33}}{2}D_{23}\right)+3\left(f^{-1}-1\right)D_{\text{m}}D_{23}\right] \quad \text{(A.29)}$$

Relationships (3.33-3.40) of chapter 2, section 3.2 are therefore retrieved. As also stated in section 3.2, the dynamic stress tensor is not symmetric even when spin effects are disregarded. This result is due to the geometrical configuration of the RVE which is not isotropic. Note that for spherical voids, Molinari and Mercier [26] showed that without spin contribution the dynamic stress tensor is symmetric.

A.3 Axisymmetric case

For an axisymmetric configuration without shear contributions, the velocity field used by Tracey [42] is of the form of Eq (3.15) with $\mathbf{D}$ expressed as:

$$\mathbf{D} = \begin{bmatrix} D_{11} & 0 & 0 \\ 0 & D_{11} & 0 \\ 0 & 0 & D_{33} \end{bmatrix}, \quad \text{(A.30)}$$

From Eqs (A.16-A.18, A.25-A.29), the only non zero components of $\boldsymbol{\Sigma}^{\text{dyn}}$ are:

$$\Sigma_{11}^{\text{dyn}} = \Sigma_{22}^{\text{dyn}} = \frac{\rho a^2}{4}\Bigg\{2f^{-1}\ln\left(\frac{1}{f}\right)\dot{D}_{11} + \left[1 - f^{-1} + f^{-1}\ln\left(\frac{1}{f}\right)\right]\dot{D}_{33} - 2\left[f^{-2} - f^{-1} - 2f^{-1}\ln\left(\frac{1}{f}\right)\right]D_{11}^2 - \frac{1}{2}(1-f)^2 f^{-2} D_{33}^2 - 2\left[f^{-2} - f^{-1} - f^{-1}\ln\left(\frac{1}{f}\right)\right]D_{11}D_{33}\Bigg\} \quad \text{(A.31)}$$

$$\Sigma_{33}^{\text{dyn}} = \frac{\rho a^2}{4}\Bigg\{2\left[1 + f^{-1}\ln\left(\frac{1}{f}\right) - f^{-1}\right]\dot{D}_{11} + \left[f^{-1}\ln\left(\frac{1}{f}\right) - \frac{1}{2}\left(f^{-1}-1\right)(3-f)\right]\dot{D}_{33} - 2\left[(1+f)f^{-2} - 3f^{-1}\ln\left(\frac{1}{f}\right) - 2\right]D_{11}^2 - \frac{1}{4}\left[f^{-2}(1-f)^3 + f^{-2} - 1 - 2f^{-1}\ln\left(\frac{1}{f}\right)\right]D_{33}^2 - 2\left[f^{-2} - 1 - 2f^{-1}\ln\left(\frac{1}{f}\right)\right]D_{11}D_{33}\Bigg\} + \frac{\rho l^2}{3}(1-f)\left(\dot{D}_{33} + D_{33}^2\right) \quad \text{(A.32)}$$

For the purpose of concise notation, we can also write:

$$\Sigma_{11}^{\text{dyn}} = \Sigma_{22}^{\text{dyn}} = \rho a^2 F\,, \Sigma_{33}^{\text{dyn}} = \rho a^2 G + \frac{\rho l^2}{3}(1-f)\left(\dot{D}_{33} + D_{33}^2\right) \quad \text{(A.33)}$$

where functions F and G, identified from Eqs (A.31-A.32), are related to the porosity f, the strain rate components D_{11} and D_{33} and their time derivative $\dot{D}_{11}$ and $\dot{D}_{33}$.

In addition to the previous axisymmetric configuration, under plane strain conditions, $D_{33} = 0$, the following relationships are obtained:

$$\Sigma_{11}^{\text{dyn}} = \Sigma_{22}^{\text{dyn}} = \frac{\rho a^2}{2}\Bigg\{f^{-1}\ln\left(\frac{1}{f}\right)\dot{D}_{11} - f^{-1}\left[f^{-1} - 2\ln\left(\frac{1}{f}\right) - 1\right]D_{11}^2\Bigg\} \quad \text{(A.34)}$$

$$\Sigma_{33}^{\text{dyn}} = \frac{\rho a^2}{2}\left\{\left[f^{-1}\ln\left(\frac{1}{f}\right) - f^{-1} + 1\right]\dot{D}_{11} - \left[(1+f)\,f^{-2} - 3f^{-1}\ln\left(\frac{1}{f}\right) - 2\right]D_{11}^2\right\} \tag{A.35}$$

Note that when $D_{33} = 0$ (i.e. the length of the cylinder remains constant, $l = l_0$), the porosity evolution is solely governed by D_{11} through $\dot{f} = 2(1-f)D_{11}$. Using in addition Eq (A.34) and $\dot{a}/a = D_{11}/f$ (matrix volume preserving) and since the static stress is expressed in terms of D_{11} and f, it appears that under imposed in plane stress (i.e. Σ_{11} is known), the radial strain rate component D_{11} can be obtained. As a consequence, when $D_{33} = 0$, one can determine the porosity evolution from knowing the stress components in the $(\mathbf{e}_1, \mathbf{e}_2)$ plane. But, interestingly, inertia effects are transferred also to the axial component of the stress tensor Σ_{33}^{dyn}. This implies that limiting the analysis to the 2D plane configuration may leave aside substantial information on the role played by micro-inertia. As a matter of fact, the axial stress needed to constrain the length of the cylinder in a dynamic problem cannot be captured by such 2D in plane approach, see Appendix C.

Appendix B

Analytical relationships for the quasi-static macroscopic stress, Σ^{static}.

The analytical expression for the static stress tensor Σ^{static} proposed by Sartori et al. [35] is specified in this appendix. Consider the unit cell of Fig. 3.1 and the Gurson yield function for cylindrical void embedded into a perfectly plastic matrix (see Eq (3.46)). Under axisymmetric loading (C_{eq}=1 in Eq 3.46), following Sartori et al. [35], the closed form expressions for quasi-static macroscopic stress tensor components are given as:

$$\Sigma_{11}^{static} = \Sigma_{22}^{static} = \sigma_0 \beta_1 \tag{B.1}$$

$$\Sigma_{33}^{static} = \sigma_0 (\beta_1 + \beta_2) \tag{B.2}$$

with,

$$\beta_1 = \frac{1}{\sqrt{3}} \ln(\mathbf{W} + \sqrt{\mathbf{W}^2 - 1}) sgn(tr\mathbf{D}) \tag{B.3}$$

$$\beta_2 = \frac{D_{33}\sqrt{3}}{tr\mathbf{D}} f \sinh(\sqrt{3}\beta_1) \tag{B.4}$$

$$\mathbf{W} = \frac{-1 + \sqrt{1 + 3\left(\frac{D_{33}}{tr\mathbf{D}}\right)^2 \left\{1 + f^2 + 3f^2\left(\frac{D_{33}}{tr\mathbf{D}}\right)^2\right\}}}{3f\left(\frac{D_{33}}{tr\mathbf{D}}\right)^2} \tag{B.5}$$

where $sgn(\cdot)$ stands for the sign of $(\cdot)$. In addition to the previous axisymmetric condition, under plane strain condition, D_{33}=0 in Eqs (B.3-B.4), the following relationships are obtained:

$$\beta_1 = \frac{1}{\sqrt{3}} \ln\left(\frac{1}{f}\right), \beta_2 = 0 \tag{B.6}$$

$$\Sigma_{11}^{static} = \Sigma_{22}^{static} = \Sigma_{33}^{static} = \frac{\sigma_0}{\sqrt{3}} \ln\left(\frac{1}{f}\right) sgn(D_{11}) \tag{B.7}$$

It thus appears that under plane strain loading, the quasi-static stress tensor $\mathbf{\Sigma}^{static}$ is spherical. As explained in detail in chapter 3, this is not the case for the total macroscopic stress tensor $\mathbf{\Sigma} = \mathbf{\Sigma}^{static} + \mathbf{\Sigma}^{dyn}$.

Appendix C

Formulation of the macroscopic dynamic stress tensor (Σ^{dyn}) for 2D approach.

In this appendix, the 2D case problem under axisymmetric loading is investigated. Therefore the main differences between 3D and 2D approaches can be presented in a clear way. Of course this analysis makes sense only for plane strain configuration.

Under plane strain axisymmetric loading without shear contributions, the macroscopic strain rate is:

$$\mathbf{D} = \begin{bmatrix} D_{11} & 0 & 0 \\ 0 & D_{11} & 0 \\ 0 & 0 & 0 \end{bmatrix}, \tag{C.1}$$

As a consequence, from incompressibility condition the radial component of $\boldsymbol{v}$ is:

$$\boldsymbol{v}_r = \frac{D_{11} b^2}{r} \tag{C.2}$$

From the conservation of momentum, one has

$$\frac{\partial \sigma_{rr}}{\partial r} + \frac{\sigma_{rr} - \sigma_{\theta\theta}}{r} = \rho\gamma_r, \qquad \frac{\partial \sigma_{zz}}{\partial z} = 0 \tag{C.3}$$

By integration from a to b with $|\sigma_{rr} - \sigma_{\theta\theta}| = \frac{2}{\sqrt{3}}\sigma_0$ and $\sigma_{\theta\theta} > \sigma_{rr}$.

$$\sigma_{rr}(r = b) = \int_a^b \frac{2}{\sqrt{3}}\sigma_0 \frac{dr}{r} + \int_a^b \rho\gamma_r dr \tag{C.4}$$

From Eq (C.2), the radial acceleration γ_r is:

$$\gamma_r = (\dot{D}_{11} + 2D_{11}^2)\frac{b^2}{r} - D_{11}^2\frac{b^4}{r^3} \tag{C.5}$$

Therefore one gets

$$\sigma_{rr}(r = b) = \frac{2}{\sqrt{3}}\sigma_0 \ln\left(\frac{b}{a}\right) + \frac{\rho a^2}{2}(\dot{D}_{11} + 2D_{11}^2)\frac{1}{f}\ln\left(\frac{1}{f}\right) + \rho\frac{D_{11}^2}{2}\frac{a^2}{f}\left(1 - \frac{1}{f}\right) \tag{C.6}$$

Finally one obtains the following macroscopic dynamic stress components:

$$\Sigma_{11}^{dyn} = \Sigma_{22}^{dyn} = \frac{\rho a^2}{2}\left[f^{-1}\ln\left(\frac{1}{f}\right)\dot{D}_{11} - D_{11}^2\left\{\frac{1}{f^2} - \frac{1}{f} - 2f^{-1}\ln\left(\frac{1}{f}\right)\right\}\right] \tag{C.7}$$

which is equivalent to Eq (A.34).

Alternatively, $\boldsymbol{\Sigma}^{dyn}$ is also defined from:

$$\boldsymbol{\Sigma}^{dyn} : \delta\mathbf{D} = \frac{1}{|V|}\int \rho\boldsymbol{\gamma} \cdot \delta\boldsymbol{v} dV \tag{C.8}$$

With Eq (C.2), one obtains:

$$\delta v_r = \frac{b^2}{r}\delta D_{11}, \quad \text{and} \quad \boldsymbol{\Sigma}^{dyn} : \delta\mathbf{D} = 2\Sigma_{11}^{dyn}\delta D_{11} \tag{C.9}$$

With recourse to the definition of $\boldsymbol{\gamma}$ given by Eq (C.5), the right hand side of Eq (C.8) is evaluated, leading to Eq (C.7).

Note that from Eq (C.8) combined to Eq (C.1) which restricts the analysis to a 2D approach, Σ_{33}^{dyn} cannot be evaluated. In fact, one has to use the complete theory developed in the PhD which allows an explicit relationhip for Σ_{33}^{dyn} valid under plane strain loading.

Bibliography

[1] Barthélémy, R., Jacques, N., Kerampran, S., and Vermeersch, F. (2016). Modelling of micro-inertia effects in closed-cell foams with application to acoustic and shock wave propagation. *International Journal of Solids and Structures*, 97-98:445 – 457.

[2] Benzerga, A. A., Besson, J., and Pineau, A. (1999). Coalescence-Controlled Anisotropic Ductile Fracture. *Journal of Engineering Materials and Technology*, 121:221.

[3] Benzerga, A. A. and Leblond, J. B. (2010). Ductile Fracture by Void Growth to Coalescence. *Advances in Applied Mechanics*, 44:169–305.

[4] Budiansky, B., Hutchinson, J. W., and Slutsky, S. (1982). Void growth and collapse in viscous solids. *in H. G. Hopkins, M. J. Sewell (Eds.), Mechanics of Solids. Oxford: Pergamon Press.*

[5] Carroll, M. M. and Holt, A. C. (1972). Static and Dynamic Pore Collapse Relations for Ductile Porous Materials. *Journal of Applied Physics*, 43:1626–1636.

[6] Cortes, R. (1992). The growth of microvoids under intense dynamic loading. *International Journal of Solids and Structures*, 29:1339–1350.

[7] Curran, D. R., Seaman, L., and Shockey, D. A. (1987). Dynamic failure of solids. *North-Holland, Amsterdam*, 147, Nos. 5-6:253–388.

[8] Czarnota, C., Jacques, N., Mercier, S., and Molinari, A. (2008). Modelling of dynamic ductile fracture and application to the simulation of plate impact tests on tantalum. *Journal of the Mechanics and Physics of Solids*, 56:1624–1650.

[9] Czarnota, C., Mercier, S., and Molinari, A. (2006). Modelling of nucleation and void growth in dynamic pressure loading, application to spall test on tantalum. *International Journal of Fracture*, 141:177–194.

[10] Czarnota, C., Molinari, A., and Mercier, S. (2017). The structure of steady shock waves in porous metals. *Journal of the Mechanics and Physics of Solids*, 107:204–228.

[11] Dorothy, H. L. and Longère, P. (2019). Unified modelling of adiabatic shear banding and subsequent micro-voiding driven dynamic failure of viscoplastic solids. *International Journal of Impact Engineering*, 132:103322.

[12] Glennie, E. B. (1972). The dynamic growth of a void in a plastic material and applica-tion to fracture. *Journal of the Mechanics and Physics of Solids*, 3:415–429.

[13] Gologanu, M., Leblond, J. B., and Devaux, J. (1993a). Approximate models for ductile metals containing non-spherical voids-Case of axisymmetric prolate ellipsoidal cavities. *Journal of the Mechanics and Physics of Solids*, 41:1723–1754.

[14] Gologanu, M., Leblond, J. B., Devaux, J., and Molinari, A. (1993b). Approximate models for ductile metals containing nonspherical voids - case of axisymmetric prolate ellipsoidal cavities. *Journal of the Mechanics and Physics of Solids*, 41:1723–1754.

[15] Gurson, A. L. (1977). Continuum theory of ductile rupture by void nucleation and growth. *Journal of Engineering Materials and Technology*, 99:2–15.

[16] Jacques, N., Czarnota, C., Mercier, S., and Molinari, A. (2010). A micromechanical constitutive model for dynamic damage and fracture of ductile materials. *International Journal of Fracture*, 162:159–175.

[17] Jacques, N., Mercier, S., and Molinari, A. (2012). Effects of microscale inertia on dynamic ductile crack growth. *Journal of the Mechanics and Physics of Solids*, 60:665–690.

[18] Klöcker, H. and Montheillet, F. (1988). Modeling the Ductile Growth of Voids At High Strain Rates. *Le Journal de Physique Colloques*, 49:C3–313–318.

[19] Leblond, J. B., Perrin, G., and Suquet, P. (1994). Exact results and approximate models for porous viscoplastic solids. *International Journal of Plasticity*, 10:213–235.

[20] Leblond, J. B. and Roy, G. (2000). A model for dynamic ductile behavior applicable for arbitrary triaxialities. *Comptes Rendus de l'Académie des Sciences - Series IIB - Mechanics*, 328:381–386.

[21] Longère, P. (2018). Adiabatic shear banding assisted dynamic failure: Some modeling issues. *Mechanics of Materials*, 116:49 – 66.

[22] Mayya, A., Banerjee, A., and Rajesh, R. (2018). Role of porosity and matrix behavior on compressive fracture of haversian bone using random spring network model. *Journal of the Mechanical Behavior of Biomedical Materials*, 83:108–119.

[23] McClintock, F. M. (1968). On Void Coalescence Under Combined Tension and Shear. *Journal of Applied Mechanics*, 82:71005–71015.

[24] Meyers, M. A. and Aimone, C. T. (1983). Dynamic fracture (spalling) of metals. *Materials Science*, 28:1–96.

[25] Molinari, A., Jacques, N., Mercier, S., Leblond, J. B., and Benzerga, A. A. (2015). A micromechanical model for the dynamic behavior of porous media in the void coalescence stage. *International Journal of Solids and Structures*, 71:1–18.

[26] Molinari, A. and Mercier, S. (2001). Micromechanical modelling of porous materials under dynamic loading. *Journal of the Mechanics and Physics of Solids*, 49:1497–1516.

[27] Morin, L., Leblond, J.-B., and Benzerga, A. A. (2015). Coalescence of voids by internal necking: Theoretical estimates and numerical results. *Journal of the Mechanics and Physics of Solids*, 75:140 – 158.

[28] Needleman, A. and Tvergaard, V. (1984). An analysis of ductile rupture in notched bars. *Journal of the Mechanics and Physics of Solids*, 32:461–490.

[29] Olevsky, E. and Skorohod, V. (1988). Some questions of sintering kinetics under external forces influence. In: Technological and Design Plasticity of Porous Materials. *IPMS NAS, Ukraine,*, pages 97–103.

[30] Ortiz, M. and Molinari, A. (1992). Effect of strain hardening and rate sensitivity on the dynamic growth of a void in a plastic material. *Journal of Applied Mechanics*, 114:48–53.

[31] Reboul, J. and Vadillo, G. (2018). Homogenized gurson-type behavior equations for strain rate sensitive materials. *Acta Mechanica*, 229:3517–3536.

[32] Rice, J. R. and Tracey, D. M. (1969). On the ductile enlargement of voids in triaxial stress fields*. *Journal of the Mechanics and Physics of Solids*, 17:201–217.

[33] Roy, G. (2003). Vers une modélisation approfondie de l'endommagement ductile dynamique, Investigation expérimentale d'une nuance de tantale et développements théoriques.

Ph.D. thesis, Ecole Nationale Supérieure de Mécanique et d'Aéronautique, Université de Poitiers, France,.

[34] Sartori, C., Mercier, S., Jacques, N., and Molinari, A. (2016). On the dynamic behavior of porous ductile solids containing spheroidal voids. *International Journal of Solids and Structures*, 97-98:150–167.

[35] Sartori, C., Mercier, S., and Molinari, A. (2019). Analytical expression of mechanical fields for Gurson type porous models. *International Journal of Solids and Structures*, 163:25–39.

[36] Sartori, C., Mercier, S., Molinari, A., and Jacques, N. (2015). Constitutive behavior of porous ductile materials accounting for micro-inertia and void shape. *Mechanics of Materials*, 80:324–339.

[37] Simo, J. C. and Hughes, T. J. R. (1988). *Computational inelasticity. Interdisciplinary applied mathematics*, volume 91. Springer.

[38] Tong, W. and Ravichandran, G. (1993). Dynamic pore collapse in viscoplastic materials. *Journal of Applied Physics*, 74:2425–2435.

[39] Tong, W. and Ravichandran, G. (1995). Inertial Effects on Void Growth in Porous Viscoplastic Materials. *Journal of Applied Mechanics*, 62:633.

[40] Torki, M. E., Benzerga, A. A., and Leblond, J. B. (2015). On Void Coalescence Under Combined Tension and Shear. *Journal of Applied Mechanics*, 82:71005–71015.

[41] Torki, M. E., Tekoğlu, C., Leblond, J.-B., and Benzerga, A. A. (2017). Theoretical and numerical analysis of void coalescence in porous ductile solids under arbitrary loadings. *International Journal of Plasticity*, 91:160–181.

[42] Tracey, D. M. (1971). Strain-hardening and interaction effects on the growth of voids in ductile fracture. *Engineering Fracture Mechanics*, 3:301–315.

[43] Tvergaard, V. (1982). On localization in ductile materials containing spherical voids. *International Journal of Fracture*, 32:157–169.

[44] Vadillo, G. and Fernández-Sáez, J. (2009). An analysis of gurson model with parameters dependent on triaxiality based on unitary cells. *European Journal of Mechanics - A/Solids*, 28:417–427.

[45] Versino, D. and Bronkhorst, C. A. (2018). A computationally efficient ductile damage model accounting for nucleation and micro-inertia at high triaxialities. *Computer Methods in Applied Mechanics and Engineering*, 333:395–420.

[46] Wang, Z. P. (1994). Growth of voids in porous ductile materials at high strain rate. *Journal of Applied Physics*, 76:1535–1542.

[47] Wang, Z. P. (1997). Void-containing nonlinear materials subject to high-rate loading. *Journal of Applied Physics*, 81:7213–7227.

[48] Wang, Z. P. and Jiang, Q. (1997). A Yield Criterion for Porous Ductile Media at High Strain Rate. *Journal of Applied Mechanics*, 64:503–509.

[49] Weck, A. and Wilkinson, D. S. (2008). Experimental investigation of void coalescence in metallic sheets containing laser drilled holes. *Acta Materialia*, 56:1774–1784.

[50] Wu, X. Y., Ramesh, K. T., and Wright, T. W. (2003). The dynamic growth of a single void in a viscoplastic material under transient hydrostatic loading. *Journal of the Mechanics and Physics of Solids*, 51:1–26.

List of Figures

1.1 Représentation schématique d'un matériau poreux contenant des cavités cylindriques parallèles. Le VER adopté est décrit par un cylindre creux à section circulaire (longueur $2l$, rayon interne a, rayon externe b). 8

1.2 Evolutions de a) la porosité f et b) des contraintes $\Sigma_{11} = \Sigma_{22},\ \Sigma_{33}$ en fonction du temps. Le chargement est axisymmétrique en déformation plane (D_{33}=0 est imposé) et $\Sigma_{11} = \Sigma_{22} = \dot{p}t$ avec $\dot{p}$ =10 et 250MPa/ns en a) et $\dot{p}$ =10MPa/ns en b). La matrice entourant les vides est rigide parfaitement plastique, de limite d'élasticité σ_0=100MPa, de masse volumique ρ=2700kg/m^3. La géométrie de la cellule élémentaire est telle que a_0=50μm, b_0=1500μm, conduisant à une porosité initiale f_0=1.1 10^{-3}. 12

1.3 Effet de la longueur initiale de vide sur l'évolution a) de la porosité lorsque l_0 varie dans l'intervalle [1:20 000]μm et b) des rayons intérieur et extérieur du VER pour $l_0 \to 0$ et l_0 =1000μm. Le chargement est sphérique: $\Sigma_{11} = \Sigma_{22} = \Sigma_{33} = \dot{p}t$, avec $\dot{p}$=10MPa/ns. La matrice entourant les vides est rigide parfaitement plastique, de limite d'élasticité σ_0=100MPa, de masse volumique ρ=2700kg/m^3. La géométrie de la cellule élémentaire est telle que a_0=50μm, b_0=1500μm, conduisant à une porosité initiale f_0=1.1 10^{-3}. 14

1.4 Compact bone made up of groups of concentric cylinders of bones, called Haversian units. a) Cubic sample from posterior cortex at mid-diaphysis with faces perpendicular to the longitudinal, radial and transverse directions. b) Optical micrograph of the sample surface showing Haversian bone. CT scan images of the Haversian bone specimen c) before fracture and d) after fracture (Mayya et al. [22]). 20

2.1 Failure mechanisms of Aluminium alloy (AA5052) with initial cylindrical voids generated using laser drilling process. The aluminium model fails by ductile fracture between the voids through internal necking. Weck and Wilkinson [49], Quasi-static condition. 24

2.2 Ductile fracture in an initially dense steel due to void growth and coalescence of voids, Benzerga and Leblond [3], Quasi-static condition. 25

2.3 Dynamic fracture in nickel by spalling. (a) Spherical voids are induced during impact. They grow and coalesce by direct impingement mechanism. (b) Formation of a string of voids in nickel. Meyers and Aimone [24], ... 26

2.4 Dynamic damage in ductile material under impact test. (a) Ductile fracture by void coalescence. (b) Impingement of voids in impact-loaded specimens of 1145 aluminium. Curran et al. [7] 26

2.5 Voids coalescence by void sheet formation in AISI 4340 steel strained plastically. Curran et al. [7] 27

2.6 Dynamic damage observed in tantalum under planar impact test at various impact velocites. Development of micro-voiding along the spall plane parallel to the impacted surface. The level of porosity is growing with increase in impacted velocity V. Complete fracture is observed at V=306m/s. Roy [33] . . . 28

2.7 Cylindrical unit cell with inner radius R subjected to axial strain rate $\dot{\bar{\varepsilon}}_z$ and radial strain rate $\dot{\bar{\varepsilon}}_r$. The resulting strain rates are due to imposed stress at infinity, McClintock [23]. 31

2.8 Long circular cylindrical unit cell (inner radius 'a' and outer radius 'b') with cylindrical void embedded inside. The porosity of the unit cell is $f = (a/b)^2$. The matrix is rigid perfectly plastic, Gurson [15]. 34

2.9 Hollow sphere model with a spherical void embedded inside a spherical shell having inner radius 'a' and outer radius 'b'. The porosity of the unit cell is $f = (a/b)^3$, Gurson [15]. 35

2.10 Gurson yield function for cylindrical voids in plane strain loading conditions. The yield loci are presented for three different loading cases. Axi-symmetric, plane strain and generalized plane strain conditions are represented by solid lines, dashed lines and dotted lines respectively for various porosities (f in the range 0.005 to 0.3). In the present figure $T = \Sigma/\sigma_0$ is the normalized macroscopic stress tensor, Gurson [15] 36

2.11 Evolution of distension with time during the pore collapse of an aluminium material of initial distention, α=1.8, with applied loading rates $\dot{P}$=2.5, 5, 10 and 20 MPa/ns. Solid line shows the predictions of the analytical model. Dashed lines show the results of the finite difference calculations, Carroll and Holt [5]. 45

2.12 A hollow sphere as a representative volume element with internal radius a and external radius b. The matrix behavior is viscoplastic and the porosity $f = a^3/b^3$. Molinari and Mercier [26]. 48

2.13 Porosity versus time evolution for both quasi-static and dynamic models. The initial porosity is f_0=0.01. Two loading rates ($\dot{\mathbf{p}}$=10MPa/ns, 250MPa/ns) and two strain rate sensitivities (m=0.05, 0.15) are tested for spherical loading. Molinari and Mercier [26] 49

2.14 Prolate (a) and oblate (b) spheroidal void embedded inside a confocal spheroid. Homogenous kinematic boundary conditions are applied on the external boundary of the unit cell, Sartori et al. [36, 34]. The RVE is similar to the Gologanu et al. [13] work. 50

2.15 Representative volume element adopted for the coalescence analysis. The RVE has a cylindrical shape (height, $2H$ and diameter, $2L$) with a cylindrical void (height, $2h$ and diameter, $2R$) inside, Molinari et al. [25] 53

3.1 Schematic representation of the porous material. A cylindrical unit cell (length $2l$, void radius a, external radius b) is taken as the representative volume element. A cartesian coordinate system is adopted for the derivation of the model with $-l < x_3 < l$. 58

4.1 Evolution of the porosity f versus a) time and b) macroscopic stress $\Sigma_{11} = \Sigma_{22} = \dot{p}t$ under plane strain loading. A comparison between dynamic (micro-inertia dependent) and static (micro-inertia independent) analyses is carried out for two stress rates: $\dot{p}$ =10 MPa/ns and $\dot{p}$ =250 MPa/ns. Material parameters are provided in Table 4.1. For D_{33} =0, results are independent from the void length. 75

4.2 Time evolution of the macroscopic stress Σ_{33} under plane strain loading. The macroscopic stress $\Sigma_{11} = \Sigma_{22} = \dot{p}t$ is imposed with $\dot{p}$=10MPa/ns. Material parameters are listed in Table 4.1. The time to fracture (i.e. when f =0.3 is reached) is strongly influenced by micro-inertia (around 1020ns in the micro-inertia dependent calculation). Under quasistatic approach (micro-inertia being neglected), the porous material sustains very limited stress up to fracture which occurs at a time around 39ns. 76

4.3 Collapse of the pore under plane strain loading, porosity f versus time. $\Sigma_{11} = \Sigma_{22} = \dot{p}t$. Comparison of dynamic (micro-inertia dependent) and quasi-static (micro-inertia independent) analyses is carried out for two stress rates: $\dot{p}$ =-10 MPa/ns and $\dot{p}$ =-250 MPa/ns. Material parameters are provided in Table 4.1. For D_{33} =0, results are independent of the void length (similar to Fig. 4.1). . 77

4.4 Effects of the mass density, of the initial radius, of the initial porosity and of the flow stress level, on the porosity evolution for dynamic expansion under plane strain configuration. The parameters of the reference material are listed in Table 4.1. The stress rate is $\dot{p}$ =10MPa/ns. 78

4.5 Effect of the initial length on the time evolution of the porosity under spherical loading. The material parameters are listed in Table 4.1 except for l_0 which is varying in the range [1:20 000]μm. The stress rate is $\dot{p}$ =10MPa/ns. The case where $l_0 \to \infty$ (resp. $l_0 \to$0) depicts the response of long (resp. short) cylinders under dynamic loading. 79

4.6 Time evolution, under spherical loading, of the external and internal radii for $l_0 \to$0, l_0 =810 and 1 000μm. Material parameters, displayed in Table 4.1, are those of Fig. 4.5 with stress rate, $\dot{p}$ =10MPa/ns. 80

4.7 Time evolution, under spherical loading, of D_{11} for $l_0 \to$0, l_0 =810 and 1 000μm. Material parameters are displayed in Table 4.1, and the stress rate, $\dot{p}$ =10MPa/ns. A magnified scale, where the y-axis is reduced, is proposed in b). 81

4.8 a) Time evolution of D_{33} under spherical loading, the initial length ranging from 1 to 20000μm - Specific powers in b) the plane, see Eq. (4.17), and c) the axial direction, see Eq. (4.18), for l_0=500, 1000, 2000μm. Other material parameters are displayed in Table 4.1 with stress rate, $\dot{p}$ =10MPa/ns. 85

4.9 Time evolution of the porosity for spherical loading and for Case 1 and Case 2 under dynamic conditions, see Table 4.3. The stress amplitude is $\dot{p}t$ with $\dot{p}$ =10MPa/ns. The initial length is a) l_0 =2 000μm, b) l_0 =10μm. Other material parameters are listed in Table 4.1. 89

4.10 Time evolution of a) the void radius a and external radius b and b) the macroscopic strain rate components D_{11} and D_{33} c) $D_{33} + 2\frac{D_{11}}{(1-f)}$, for Case 2: $\Sigma_{11} = \Sigma_{22} = \dot{p}t$ with $\dot{p}$ =10MPa/ns, $\Sigma_{33} = 0$. The initial length is l_0 =2 000μm, other material parameters being listed in Table 4.1. 90

4.11 Influence of a) the mass matrix density with l_0=2000μm and b) the initial void length with ρ=2700kg/m^3 for Case 2: $\Sigma_{11} = \Sigma_{22} = \dot{p}t$ with $\dot{p}$ =10MPa/ns, $\Sigma_{33} = 0$. The other material parameters are displayed in Table 4.1. The response with l_0 =10 000μm provides the plane strain case of Fig. 4.1, in terms of porosity evolution only. 92

4.12 Influence of a) the mass matrix density with l_0=2 000μm and b) the initial void length with ρ=2700kg/m^3 on porosity evolution for loading Case 1 (uniaxial stress). The other material parameters are displayed in Table 4.1. The evolution of the axial stress is given by $\Sigma_{33} = \dot{p}t$ with $\dot{p}$ =10MPa/ns. 94

4.13 Time evolution of a) the void radius a and external radius b and b) the macroscopic strain rate components D_{11} and D_{33} for loading Case 1 (uniaxial stress with $\Sigma_{33} = \dot{p}t$, $\dot{p}$ =10MPa/ns). The initial length is l_0 =2 000μm, the mass matrix density is ρ =270kg/m^3, other material parameters being listed in Table 4.1. 95

4.14 Time evolution, under imposed constant strain rate D_{33} and prescribed $\Sigma_{11} = \Sigma_{22} = \dot{p}t$ with a) $\dot{p}$ =10MPa/ns b) $\dot{p}$ =100MPa/ns. The initial length is l_0 =100μm, other material parameters being listed in Table 4.1. 96

4.15 Time evolution of the porosity under imposed in-plane stress $\Sigma_{11} = \Sigma_{22} = \dot{p}t$ and constant velocity v_3^0. Calculations are performed for D_{33}^0 =10^{5}s^{-1} and 10^{6}s^{-1} considering l_0 =1000 and 2000μm which infers various applied constant velocities. Other material parameters are given in Table 4.1. 98

5.1 Finite element cylindrical unit cell of length l, inner radius a and external radius b used for various loading cases. The mesh is made with 4 node axisymmetric elements (CAX4R). The element size is 20μm$\times$40μm. 102

5.2 Comparison between FEM and analytical results for plane strain loading. Time evolution of a) the porosity and b) the axial stress. The stress rate is $\dot{p}$ =10MPa/ns. The reference material with parameters listed in Table 4.1 is considered. . . . 104

5.3 a) Finite Element model of 2D unit cell of inner radius a and external radius b used for the plane strain problem. The mesh is made with 4 node plane strain elements with reduced integration (CPE4R). Comparison between FEM plane strain model (CPE4R), FEM axisymmetric model (CAX4R) and the analytical approach for the time evolution of b) porosity, f and c) axial stress, Σ_{33}. The reference material with parameters listed in Table 4.1 is considered. The stress rate is $\dot{p}$ =10MPa/ns. 106

5.4 a) Shape of the deformed unit cell at the end of the FE calculations for spherical loading achieved by using boundary condition inherited from the analytical model without multi-point constraints on inner ∂B_a and outer ∂B_b boundaries of the unit cell depicted in Fig. 5.1. b) Time evolution of the ratio a^2/b^2 measured at ∂B_0 and ∂B_l when multiple kinematic constraints are disregarded. The evolution of the porosity obtained from the analytical approach, which will be shown to coincide with the FEM results when multiple kinematic constraints are imposed, is superimposed. 108

5.5 Closed cylindrical unit cell of length l, inner radius a and external radius b having a thin plate of thickness t_p on the top. CAX4R elements with initial size of 20μm x40μm are used. 109

5.6 FEM calculations for hydrostatic loading achieved by applying stress on the top surface and lateral direction of the closed unit cell of Fig. 5.5. a) without multi-point constraint on the outer boundary ∂B_b, b) without multi-point constraint on the top boundary ∂B_l and c) without multi-point constraint on the inner boundaries ∂B_l and ∂B_{t_p}. 110

5.7 Time evolution of the porosity for a porous medium with cylindrical void under spherical loading with $\dot{p}$ =10MPa/ns and considering the reference material of Table 4.1 with l_0 =2000μm. Comparison between analytical results and FEM calculations. The approach based on the analytically inherited velocity field and the closed unit cell give comparable results. 111

5.8 FEM calculations and analytical results for thin cylinder (l_0=10μm) subjected to spherical loading, a) Porosity versus time and b) Internal and external radii vs time. The stress rate is $\dot{p}$ =10MPa/ns. The reference material with parameters listed in Table 4.1 is considered. The FEM calculations and analytical results give good agreement. 112

5.9 Time evolution of porosity validation of analytical results with FEM calculation. A constant strain rate is imposed on the top surface ∂B_l D_{33}=$10^5 s^{-1}$ and a prescribed stress Σ_{11}=Σ_{22}=$\dot{p}t$ is applied on ∂B_b. The initial length is l_0 =100μm, other material parameters listed in Table 4.1 are considered. The FEM calculation and analytical results are in good agreement. 113

5.10 Time evolution of porosity comparison of FEM calculations and analytical result for uniaxial stress loading configuration: Σ_{11}=Σ_{22}=0 and Σ_{33}=$\dot{p}t$ (Case 1, χ=1/3). The stress rate is $\dot{p}$=10MPa/ns. Parameters for the reference material are listed in Table 4.1 with l_0=2000μm and ρ=$270 Kg/m^3$. 114

5.11 FEM calculations and analytical result comparison for loading case Σ_{11}=Σ_{22}=$\dot{p}t$ and Σ_{33}=0 (case 2, χ=2/3) a) l_0=2000μm b) l_0=10μm. The stress rate is $\dot{p}$=10MPa/ns. The reference material with parameters listed in Table 4.1 is considered. . . . 115

5.12 Time evolution of the porosity. FEM calculations for two Poisson's ratio=0.499 and 0.33 with Young's modulus E=70GPa under a) plane strain loading b) hydrostatic loading. Model predictions are also displayed. The loading rate is $\dot{p}$ =10MPa/ns. The material parameters listed in Table 4.1 are considered. . . 117

5.13 Comparison of FEM calculations for various Young modulus, E=0.7, 6.3, 70 and 6300GPa under a) Plane strain loading b) Hydrostatic loading. The Poisson ratio is 0.499. Time evolution of the porosity for $\dot{p}$ =10MPa/ns. The material parameters listed in Table 4.1 is considered. 118

List of Tables

2.1 Expression of the static pressure $P_{eq}(\alpha)$ for the elastic, elastic-plastic and plastic phases during dynamic compaction, from Carroll and Holt [5] 44

4.1 Reference material parameters, representative for porous aluminium. 74

4.2 Various configurations used to compute the critical length for $l_0 < l_0^{\text{cr}}$, $\dot{D}_{11} < 0$. The critical value l_0^{cr}, obtained from the complete modeling, is well compared to the analytical approximation $l_0^{\text{cr, approx.}}$ given by Eq (4.12) 84

4.3 Loading configurations and corresponding triaxialities. 88

Résumé

La rupture des matériaux ductiles résulte de l'interaction de trois mécanismes, à savoir la nucléation, la croissance et la coalescence des vides. Dans ce doctorat, nous nous intéressons à l'endommagement des matériaux poreux par croissance de vides cylindriques, sous chargement dynamique. Cette étude a un intérêt particulier notamment pour l'atténuation des ondes de choc dans le cadre de la protection des structures. Par ailleurs, du fait du développement de la fabrication additive, la conception de matériaux contenant des vides cylindriques est une voie possible pour créer des matériaux légers à haut pouvoir dissipatif. Ce travail s'attèle à décrire le comportement dynamique de matériaux architecturés tels que des nids d'abeille faiblement poreux.

En conditions dynamiques, les vides sont soumis à une expansion rapide, induisant localement (au voisinage de la cavité) de très fortes accélérations. Cet effet d'inertie locale, ou micro-inertie, est connu pour influencer fortement la réponse macroscopique mais aussi le développement de la porosité. En fait, il a été montré précédemment que le tenseur des contraintes macroscopiques est la somme d'un tenseur des contraintes statiques (dans le sens indépendant de la micro inertie) et d'un tenseur des contraintes dynamiques. Ce dernier terme va contenir toutes les informations liées aux accélérations et sera intrinsèquement relié à la microstructure (taille et forme des vides).

Dans ce travail, un volume élémentaire représentatif cylindrique est adopté (rayons interne a et externe b, hauteur $2l$). Les contraintes statiques dérivent d'un modèle de la littérature. Les contraintes dynamiques sont évaluées à partir d'un champ cinématiquement admissible. On observe in fine que les contraintes dynamiques sont proportionnelles à la masse volumique de la matrice, sont liées à la porosité, au tenseur vitesse de déformation de manière quadratique, à sa dérivée temporelle de manière linéaire mais surtout fait intervenir deux longueurs internes (rayon interne du vide et longueur de celui-ci). Pour des chargements axisymétriques, on montre que les contraintes dynamiques dans le plan ne dépendent que du rayon du vide alors que les contraintes dynamiques hors plan font apparaître les deux longueurs internes.

Les prédictions du modèle ont été testées en considérant de nombreux exemples parmi lesquels le chargement sphérique, en contraintes planes, déformations planes, traction uniaxiale, chargement biaxial. En déformation plane sous chargement axisymétrique, le modèle quasi-statique prédit que le tenseur des contraintes associé est sphérique. En chargement dynamique, en revanche la contrainte axiale est différente de la composante radiale. Nous avons aussi observé pour un chargement sphérique que l'accroissement de la porosité résulte d'une augmentation du rayon du vide et d'une diminution du rayon externe du VER. Cette observation est propre aux effets de micro-inertie. De nombreuses tendances originales sont illustrées dans ce document. A noter que l'ensemble des prédictions du modèle a été validé par confrontation avec des calculs éléments finis sur des cellules élémentaires cylindriques.

Mots clés: Homogénéisation dynamique, micro-inertie, longueurs internes, endommagement, matériaux poreux

Abstract

The fracture of ductile materials is often the result of the nucleation, growth and coalescence of microscopic voids. In this thesis, we mainly focus on the dynamic void evolution in porous media containing cylindrical voids. This study covers a problem that is of particular interest in many areas of research (e.g. development of shock mitigation devices for civil or military applications). Owing to the development of additive manufacturing, the processing of porous material with cylindrical voids is an option to create lightweight materials having interesting properties in terms of energy dissipation. Therefore, our work aims at describing the dynamic response of architectured materials such as honeycomb structures. In dynamic loading, micro-voids sustain an extremely rapid expansion which generates strong acceleration of particles in the vicinity of cavities. These micro-inertia effects are known to play a significant role in the macroscopic response and the development of damage in porous media. In fact, the overall macroscopic stress is found to be the sum of two contributions: a static term (micro-inertia independent term) and a dynamic term (micro-inertia dependent term), the latter being related to the microstructure (e.g. size and aspect ratio of voids).

In our work, a cylindrical shell is adopted as a Representative Volume Element (internal and external radii a and b, length $2l$) for the porous material. The static term is derived from a yield function available in the literature. The dynamic stress is evaluated analytically using a trial velocity field for cylindrical voids combined with the multi-scale approach developed in the literature in LEM3. It is shown that the dynamic stress is scaled by the mass density, two characteristic lengths of the voids, the porosity, the macroscopic strain rate tensor and the time derivative of the strain rate tensor. An important outcome of the model is the differential lengthscale effect which exists between in- plane and out of plane components of the macroscopic stress. Namely, it is observed for axisymmetric loading that in-plane dynamic stress components are only related to the void radius a while the out of plane stress component is linked to a and the length of the RVE, l.

In the thesis, we present the dynamic response of the porous medium when subjected to various loading conditions: spherical loading, axisymmetric plane strain loading, uniaxial loading and biaxial loading. While for plane strain loading under quasi static condition, the overall axial stress is spherical, in dynamic conditions, the inertia contribution hinders the overall stress tensor from being spherical. Another important result of the proposed theory is the effect of the void length, which does not exist in quasi static conditions where the overall response is solely modulated by the porosity. The case of thin cylinders under dynamic loading reveals a peculiar damage kinetics. In fact, the damage developed in such porous materials results from an increase of the void radius and a reduction of the external radius. The void collapse for uniaxial as well as for biaxial loadings are new observations. The analytical model predictions are validated based on comparisons with finite element calculations (Abaqus/Explicit).

keywords: Dynamic homogenization, micro-inertia, length-scale effect, damage, porous material